MASTER OF SCIENCE THESIS

# Induction heating of uni-directional carbon-fibre PEKK composites

## Multiphysics modelling

R.S. de Wit


Faculty of Aerospace Engineering · Delft University of Technology

TU Delft Delft University of Technology

# INDUCTION HEATING OF UNI-DIRECTIONAL CARBON-FIBRE PEKK COMPOSITES

## MULTIPHYSICS MODELING

by


| | |
|---|---|
| Student name: | Robin Sebastian de Wit |
| Student number: | 4091639 |
| Student mail address: | R.S.deWit@student.tudelft.nl |
| Student telephone number: | +31655183637 |


| | | |
|---|---|---|
| Graduation assignment: | August $1^{st}$, 2016 – November $10^{th}$, 2017 | |
| Supervisor KVE: | Maarten Labordus, | Kok & Van Engelen Composite Structures BV |
| Supervisor TU: | Irene Fernandez Villegas, | Technical University, Delft |

An electronic version of this report is available.

The work in this thesis was supported by Kok & Van Engelen composite structures. Their cooperation is gratefully acknowledged.


DELFT UNIVERSITY OF TECHNOLOGY
FACULTY OF AEROSPACE ENGINEERING
DEPARTMENT OF AEROSPACE STRUCTURES AND MATERIALS

**GRADUATION COMMITTEE**

Dated: November $10^{th}$, 2017

Chair holder:

Dr.ir. R.C. (René) Alderliesten

Committee members:

Dr. I. (Irene) Fernandez-Villegas

Dr.ir. J.M.J.F. (Julien) van Campen

Ir. M. (Maarten) Labordus

# ABSTRACT

The usage of carbon-fibre reinforced composite materials in the aerospace industry has been steadily increasing due to their light weight solution with respect to their metal counterparts. Using thermoplastic resins gives rise to induction heating as a joining technique. Induction heating can be applied by utilising the inherent material properties of the adherends themselves. This avoids having to input a foreign material in between adherends that has to heat up the joint. It is a form of non-contact heating, it is relatively cost-effective and it is a rapid form of heating. One of the major challenges in using induction heating is controlling the temperature distribution within adherends. The temperature distribution directly influences the quality of the bond and is controlled by numerous process parameters. Having computational models able to predict the influence of these process parameters is of key importance into optimising the bond quality in a cost-effective and time-efficient manner. This research focuses on the electromagnetic response of UD CF-PEKK laminates on an alternating electromagnetic flux. It shows the relation between the micro-structure and electric material properties with the thermal response to an electromagnetic wave. This research fills the gap in literature by modelling this response for unidirectional laminates heated without the use of susceptor materials. These models can ultimately be used as optimisation tools within the process of continuous induction welding.

# PREFACE

After successfully completing an internship at GKN Fokker, I was determined to do my graduation assignment also in collaboration with a company. With Fokker being a relatively large company, the goal was to find a smaller company to also be able to experience working in such an environment. KVE Composites in Den Haag stood out due to their small size, but large impact on welding of thermoplastic composites. I was very pleased to hear that I could do my graduation assignment under their guidance. Induction heating without using additional materials spoke to my imagination. With the prospect of contributing to this subject, I accepted the graduation assignment without hesitation. With that, dr. Irene Fernandez-Villegas became my mentor on the university and ir. Maarten Labordus my mentor at the company.

I would like to thank dr. Irene Fernandez-Villegas for all of her support and critical thinking during my graduation project. She helped me narrow down the true goal of the project and always critically reviewed my actions. It helped me in truly understanding the results obtained. I would also like to thank ir. Maarten Labordus and Matthijs Bosboom for all of their help on the practical side of the graduation project. By actually experiencing what induction welding is instead of just modelling it. I would like to thank Kim Villa Bramon for being a sparring partner whenever I was in doubt about certain subjects. With both of us investigating induction heating, I think heaving someone to spar with makes for a more fun and challenging graduation project. Having done several different experiments, I have often been inside of the 'Vliegtuighal'. Misja Huizing, Frans Oostrum, and all of the other employees have helped me greatly in working with the sometimes heavy equipment needed to perform the different experiments. Last but not least, I would like to thank my family, girlfriend and fellow students for supporting me through this great ordeal. It was a long but memorable trip.

*R.S. de Wit*
*Delft, October 2017*

# CONTENTS

# LIST OF FIGURES

# LIST OF TABLES

# LIST OF ABBREVIATIONS

**3D:** Three-Dimensional
**AC:** Alternating-Current
**CF:** Carbon Fibre
**CFRP:** Carbon-fibre Reinforced Plastic
**CFRTPC:** Continuous Fibre-Reinforced Thermoplastic Composite
**DC:** Direct-Current
**DSC:** Differential Scanning Calorimetry
**EM:** Electromagnetic
**emf:** electro motive force
**FEM:** Finite Element Method
**FGMRES:** Flexible Generalized Minimum RESidual iterative method
**IR:** Infrared
**KVE:** Kok en Van Engelen
**PAEK:** Poly(Aryl-Ether-Ketone)
**PAN:** Polyacrylonitrile
**PEEK:** Poly(Ether-Ether-Ketone)
**PEI:** Poly(Ether-Imide)
**PEKK:** Poly(Ether-Ketone-Ketone)
**PPS:** Poly(Phenylene-Sulfide)
**RT:** Room Temperature
**TH:** Thermal
**UD:** Uni-Directional

# LIST OF SYMBOLS

| | |
|---|---|
| $\delta$ | Penetration depth $[m]$ |
| $\epsilon''_{eff}$ | Relative effective permittivity loss factor $[-]$ |
| $\epsilon'$ | Relative permittivity constant $[-]$ |
| $\epsilon_0$ | Permittivity of free space $[F/m]$ |
| $\epsilon''_a$ | Relative atomic loss factor $[-]$ |
| $\epsilon''_d$ | Relative dipolar loss factor $[-]$ |
| $\epsilon''_e$ | Relative electronic loss factor $[-]$ |
| $\epsilon''_{MW}$ | Relative Maxwell-Wagner loss factor $[-]$ |
| $\kappa$ | Dielectric constant [-] |
| $\mu_0$ | Magnetic permeability of free space $[H/m]$ |
| $\mu_r$ | Relative magnetic permeability medium $[H/m]$ |
| $\omega$ | Angular frequency $[rad/s]$ |
| $\Phi_E$ | Electric field flux $[V \cdot m]$ |
| $\Phi_B$ | Magnetic flux $[Wb]$ |
| $\rho$ | Electric resistivity $[\Omega \cdot m]$ |
| $\rho$ | Mass density $[kg/m^3]$ |
| $\rho_f$ | Electric resistivity fibre $[\Omega \cdot m]$ |
| $\sigma$ | Electric conductivity $[1/(\Omega \cdot m)]$ |
| $\sigma_B$ | Stefan-Boltzmann constant $[W/(m^2 \cdot K^4)]$ |
| $\vec{B}$ | Magnetic field $[T]$ |
| $\vec{E}$ | Electric field $[N/C]$ |
| $A$ | Area $[m^2]$ |
| $A_f$ | Cross section fibre $[m^2]$ |
| $c$ | Heat capacity per unit mass $[J/(kg \cdot K)]$ |
| $e$ | Emissivity constant [-] |
| $f$ | Frequency of input current $[Hz]$ |
| $h$ | Heat transfer coefficient $[W/(m^2 K)]$ |
| $I$ | Current [A] |
| $k$ | Thermal conductivity $[W/(m \cdot K)]$ |
| $k_\alpha$ | Thermal conductivity in longitudinal direction $[W/(m \cdot K)]$ |
| $k_\beta$ | Thermal conductivity in transverse direction $[W/(m \cdot K)]$ |
| $l_f$ | Length fibre $[m]$ |
| $m$ | Mass $[kg]$ |
| $P$ | Power $[W]$ |
| $Q$ | Heat $[J]$ |
| $q$ | Charge $[C]$ |
| $q''_s$ | Surface heat flux $[W/m^2]$ |
| $r$ | Distance [m] |
| $R_f$ | Resistance fibre $[\Omega]$ |
| $R_{jc}$ | Resistance fibre $[\Omega]$ |
| $T$ | Temperature $[K]$ |
| $t$ | Time $[s]$ |
| $T_s$ | Surface temperature $[K]$ |
| $T_{\text{inf}}$ | Ambient temperature $[K]$ |
| $tan(\delta_{eff})$ | Permittivity loss tangent [-] |
| J | Complex current density $[A/m^2]$ |
| n | Integration node [-] |
| V | Volume $[m^3]$ |

# SUMMARY

With the increase in the usage of thermoplastic composites in the aerospace industry, the search for suitable joining techniques continues. Mechanically fastening the composites would mean penetrating the fibres that give strength to the composite material. Next to that, holes attract stresses, act as areas susceptible to crack nucleation and the bolts and rivets add weight to the overall structure. An alternative is offered with adhesive bonding. However, for primary load bearing aircraft structures, adhesively bonded joints cannot be certified. The lack of non-destructive testing methods for assessing the quality of the adhesively bonded joints makes one unable to use adhesive bonding as a joining technique. The advantage of thermoplastic composites is that one can heat up the material, and cool it back down without degrading it. This makes fusion bonding one of possible joining methods worth investigating. The three popular methods of fusion bonding consist of resistance welding, ultrasonic welding and induction welding.

The current research focusses on induction welding of carbon fibre reinforced Poly(Ether-Ketone-Ketone) (PEKK) laminates with an unidirectional lay-up. One of the main challenges within induction welding is accurate control of the temperature increase of the adherends. There are multiple process parameters that can influence the temperature increase of the adherends during induction heating. One is able to change the coil shape, the distance between the coil and laminate, add cooling of the outer surfaces of the adherends, change the power settings and many more. In order to optimise the quality of the induction welded joint, one should optimise these process parameters. In order to do this in a time-efficient and cost-effective manner, this research proposes a computational model that can be used as a optimisation tool. The research sets itself apart by focussing on the intrinsic material properties of the unidirectional Carbon Fibre (CF)-PEKK material. It will investigate what causes the laminate to heat up during induction heating and will model the multi-physics problem based on a finite-element model.

Experimental results showed how junction heating is dominant in the heating of unidirectional CF-PEKK laminates. The lay-up and the fibre orientation determines the locations at which most of the heat is generated. Electric conductivity measurements indicated electric current paths to exist in every direction of the material. Microscopy confirmed this and visualised the fibre-fibre contacts existent perpendicular to the fibre direction. A distinction is made between the electric material properties of the individual plies and the additional electric resistances present at the interfaces between plies. Without accumulation of charge present within the Uni-Directional (UD) CF-PEKK laminates, a method is proposed that finds these separate electric properties, needed to model the electric behaviour of the UD CF-PEKK material. Findings regarding the generation of heat are used in modelling the multi-physics induction heating phenomenon.

A computational model was made with the help of Comsol Multiphysics. The induction heating of the UD CF-PEKK material was modelled based on the distinctive electric material properties and electric interface constraints found when determining the main heating principle. Results showed the model capable of predicting the heating patterns witnessed during induction heating experiments. The prediction of the temperature increase for the different laminate lay-ups, orientations and coils were however not accurate. Several recommendations should be incorporated in order to improve the model and result in an efficient tool of optimising induction welded joints of the UD CF-PEKK laminates. One should find the thermal material properties of the UD CF-PEKK material with respect to temperature. Next to this, the experimental data used for validating the computational model should be re-evaluated. Only then can one with certainty determine whether the model can be validated or not.

“The only true wisdom is in knowing you know nothing.”

— *Socrates*

# 1

# INTRODUCTION

With the increase in the use of composite materials in the aerospace industry [1], the need for suitable joining methods increases as well. This research focuses on the use of Carbon-fibre Reinforced Plastics (CFRPs). Opposed to thermoset matrices, thermoplastics have an infinite shelf life, high impact damage resistance, do not have to be kept refrigerated and are easy processable [2, 3]. Due to the formability of thermoplastics, fusion bonding is one the key interests in the joining of carbon-fibre reinforced thermoplastic composites, next to adhesive bonding and mechanical fastening.

Mechanical fastening is a suitable method for joining of metallic parts in the aerospace industry. When using composites, there are some drawbacks related to mechanical fastening. Mechanical fastening requires holes to be drilled in the material, causing stress concentrations, possible delaminations, strength reduction and area's at which crack nucleation can take place. Using nuts, bolts or rivets, increases the weight of the connection, increases tooling and production costs and could cause galvanic corrosion [4].

Critically reviewing adhesive bonding, one can see that it requires extensive surface preparation of the adherends, it lacks certification methods for primary aircraft structures [5] and requires a controlled industrial environment [6–8]. Contaminations will have a direct effect on the strength and durability of adhesively bonded joints [6]. Fusion bonding does not entail the same requirements and drawbacks as proposed with mechanical fastening and adhesive bonding. This makes fusion bonding to be a promising method of joining composite materials.

There are multiple different fusion bonding techniques, of which a small overview is given in Figure 1.1.

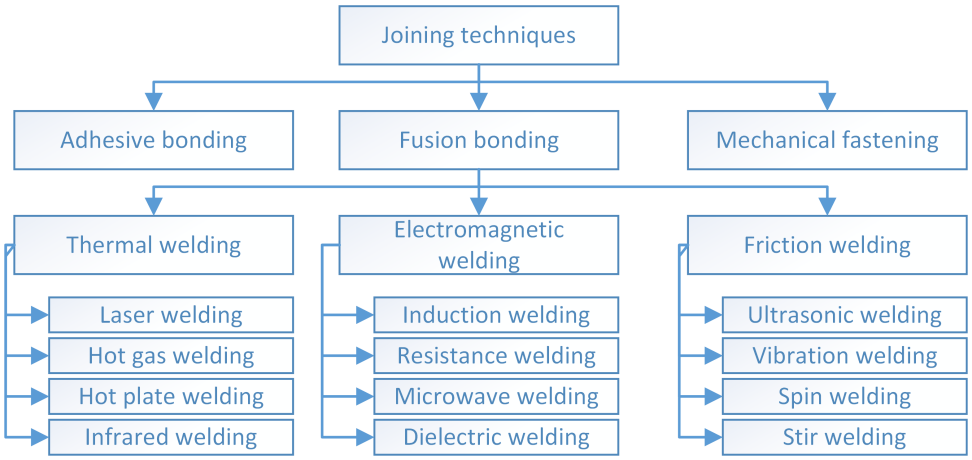


Figure 1.1: Bonding techniques applicable to composites [4]

It shows that fusion bonding can roughly be divided into three separate groups: thermal-, electromagnetic- and friction welding. Of all of the possible fusion bonding techniques, resistance-, induction- and ultrasonic welding are most widely used for joining Continuous Fibre-Reinforced Thermoplastic Composites (CFRTPCs) [9].

The principle behind ultrasonic welding is the conversion of work into frictional heat. Intermolecular friction induced by high frequency vibrations, causes viscous matrix flow due to the temperature increase of the material [4]. Welding frequency, pressure, amplitude and duration are major influences on the final quality of the

weld. It is a fast and energy-efficient process, enabling high production rates [4, 10]. High frequency oscillatory motions can however cause fibre disruption at the interface. Next to that, an energy director is needed in between adherends.

Another frequently used fusion bonding technique is resistance welding. Resistance welding uses a conductive susceptor placed in between the adherends, through which a current is fed. Joule losses causes the susceptor and surrounding material to heat up [11]. It is a simple and cost-effective set-up. The downside to using resistance welding is the need for a susceptor in between the adherends. This can cause a reduction in joint strength, air entrapment and potential problems regarding corrosion [4, 10].

Induction welding does not have to rely on a susceptor placed in between the adherends. When looking at carbon-fibre reinforced plastics, no susceptor is needed because the carbon fibres are conductive. This makes the carbon fibre susceptible to electromagnetic waves, which cause eddy currents to be generated when closed circuits are formed inside of the laminate. Due to the resistance encountered by the eddy currents, heat is generated [4]. It is a local method of heating, it is a form of non-contact heating, relatively cost-effective and is a rapid form of heating with melting temperatures occurring in a matter of seconds [3]. Susceptorless induction heating makes use of the intrinsic properties of the CFRTPCs; one no longer has to place additional materials in between the adherends. One of the major challenges for using induction welding is the accurate control of the thermal distribution throughout the adherends. The control of temperatures occurring is one the main challenges in induction welding and will be part of this research project.

## 1.1. MOTIVATION

Kok en Van Engelen (KVE) composites in Den Haag is one of the pioneers in the area of induction welding and is part of this research. Their induction welding set-up is currently being used for the manufacturing of the tailwing of the Gulfstream G650 by GKN Fokker [12]. It is desired to be able to accurately predict the temperature distributions in the materials that are welded together. The temperature distribution has a direct effect on the final quality of the weld. Predicting such temperatures, can be done with the help of a Finite Element Method (FEM) program that is based on applying the multi-physics laws involved. Having a computational model enables one to perform time- and labour efficient analyses into process parameters that govern the final quality of the joint. KVE is able to predict the thermal behaviour during induction heating for a woven Carbon Fibre (CF)-Poly(Phenylene-Sulfide) (PPS) laminate [13–16]. When using the same model for a Uni-Directional (UD) lay-up CF-Poly(Ether-Ketone-Ketone) (PEKK) laminate, the computational model is unable to predict the heating behaviour of the laminate for both the heating pattern as well as the temperature prediction. The graduation assignment is included in Appendix A. The main goals of the assignment are to find the correct electric material properties of the UD CF-PEKK material and use that to model the induction heating phenomenon. The goal of the current research is to create an understanding on what actually happens during induction heating of UD lay-up CF-PEKK and how this is influenced by properties like fibre orientation and lay-up, and how it is related to the inherent electrical properties of the laminate's constituents.

## 1.2. BASICS BEHIND INDUCTION WELDING

Induction heating is based on the creation of alternating magnetic fields in the vicinity of a conductive material. Figure 1.2 gives a general drawing of a susceptorless induction heating set-up, making use of the conductive nature of the laminate.

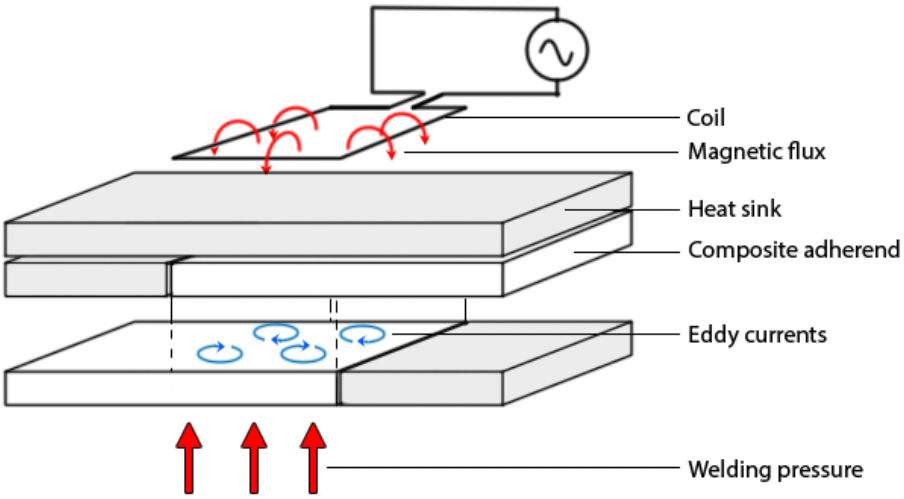


Figure 1.2: Experimental set-up induction welding without susceptor

A heat sink is placed on top of the laminate, in order to take away heat from the outer surface. This is done in order to prevent thermal degradation of the outer surface of the laminate. Pressure is applied to ensure surface contact between adherends. Surface contact is one of the two requirements for bonds to occur. Surface contact and polymer chain mobility causes interdiffusion of polymer chains, erasing the interface between adherends [17]. Polymer chain mobility is caused due to an increase in molecular kinetic energy (increase of temperature). In order to increase the kinetic energy of the molecules, energy should be added. With induction heating, this is done in the form of electromagnetic waves. These electromagnetic waves are generated by the copper coil, connected to an Alternating-Current (AC)-generator. The entire process is a combination of electromagnetism and thermodynamics.

### 1.2.1. ELECTROMAGNETISM

The entire electromagnetic process can be described with the help of the four fundamental equations of Maxwell, given in Table 1.1.

Table 1.1: Maxwell's equations [18]

| **Law** | **Equation** | |
|---|---|---|
| Gauss's law for electricity | $\oint E \cdot dA = \frac{q_{enclosed}}{\epsilon_0}$ | (1.1) |
| Gauss's law for magnetism | $\oint \vec{B} \cdot d\vec{A} = 0$ | (1.2) |
| Faraday's law | $\oint \vec{E} \cdot d\vec{r} = -\frac{d\Phi_B}{dt}$ | (1.3) |
| Ampère's law | $\oint \vec{B} \cdot d\vec{r} = \mu_0 I_{encircled} + \mu_0 \epsilon_0 \frac{d\Phi_E}{dt}$ | (1.4) |

Equation 1.1 is called Gauss's law for electricity and shows the relation between the closed integral of an electric field $E$ over a surface area $A$, which equals the charge $q$ that this surface area encloses, divided by the permittivity constant $\epsilon_0$. It basically states that there is an electric field present around charged particles. Equation 1.2 is called Gauss's law for magnetism and gives the closed integral of a magnetic field $B$ over a surface area $A$, which equals zero. It states that the magnetic flux through a closed surface will always be equal to zero, because magnetic field lines do not have a beginning or ending, but form closed loops. Equation 1.3 is called Faraday's law and shows that for any change in magnetic flux $\frac{\Phi_B}{dt}$, an electric field $E$ occurs. The opposite is also true and stated by Equation 1.4, Ampère's law. It states that magnetic field $B$ occurs, when either a current $I_{encircled}$ or change in electric field flux $\frac{\Phi_E}{dt}$ is present. The parameter $\mu_0$ in this case, represents the permeability constant of free space.

In order to get a better understanding of the physics behind induction welding, one can first take a closer look at what happens at the source of the electromagnetic waves.

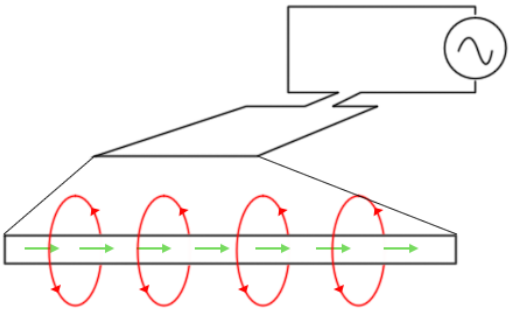

Figure 1.3: Close-up copper coil

Figure 1.3 shows part of the copper coil and the drift velocity vector the electrons attain due to a potential difference generated by the AC power supply. This drift velocity of electrons is known as an electric current, and by the definition of Ampère's law (Equation 1.4), a magnetic field will be present around this current. Gauss's law for magnetism (Equation 1.2) dictates that the magnetic field lines form closed loops around the current carrying wire. Figure 1.3 only shows the field lines at a fixed distance, but in reality, the magnetic field is present all around the current carrying wire. The magnetic field strength can be described with the help of the Biot-Savart law, given in Equation 1.5.

$$\begin{aligned} d\vec{B} &= \frac{\mu_0}{4\pi}\frac{Id\vec{l}\times\hat{r}}{r^2} \\ \vec{B} &= \int d\vec{B} = \frac{\mu_0}{4\pi}\int \frac{Id\vec{l}\times\hat{r}}{r^2} \end{aligned} \tag{1.5}$$

In which $\mu_0$ stands for the permeability constant of free space, $r$ the distance, $I$ the current and $\hat{r}$ the unit vector pointing from source to point of measurement. The equation shows that the strength of the magnetic field decreases with the distance squared. The further one places the coil from the laminate, the smaller the strength of the magnetic field that reaches the laminate. Knowing how the magnetic field is produced, one can start looking at what is happening inside of the laminate. Figure 1.4 shows a close-up of the laminate and depicts the physics occurring inside the laminate.

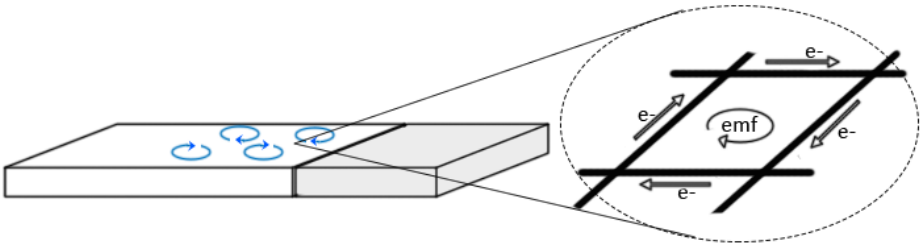


Figure 1.4: Close-up laminate

The conductive carbon fibres, which are present inside the laminate, can form circuits through which currents can run. Figure 1.4 shows an example where the fibres of separate layers are oriented perpendicular to each other. With the principle of mutual inductance, one can explain what is happening in the laminate. The conducting fibres form either closed or open circuits in the laminate. The current going through the coil alternates due to the AC-generator, resulting in an alternating magnetic field. This change in magnetic flux causes an electro motive force (emf) to be induced within the laminate, which causes electrons to start moving. The movement of electrons creates a separate magnetic field, opposing the orignial magnetic field of the copper coil. The direction of the eddy currents is thus based on the current source, as described by Lenz's law. With a UD-layup, the possibility exists that the individual fibre plies are electrically separated due to the presence of

matrix. Eddy currents can still be generated but will accumalate at the fibre-matrix interface, until the potential difference at the gap opposes the induced emf [18]. The movement of electrons and the possible creation of potential differences between plies causes heat to be generated.

### 1.2.2. HEATING PRINCIPLES

Based on the movement of electrons through the laminate, power will be dissipated in the form of heat. Power dissipation can occur through Joule losses through the fibres, Joule losses through the resistance at the fibre junctions, dielectric hysteresis at fibre junctions and magnetic hysteresis when the material is ferro-magnetic [4, 10, 19–23]. The latter is not applicable and will thus not be evaluated in this report. The three remaining heating mechanisms are schematically drawn in Figure 1.5.

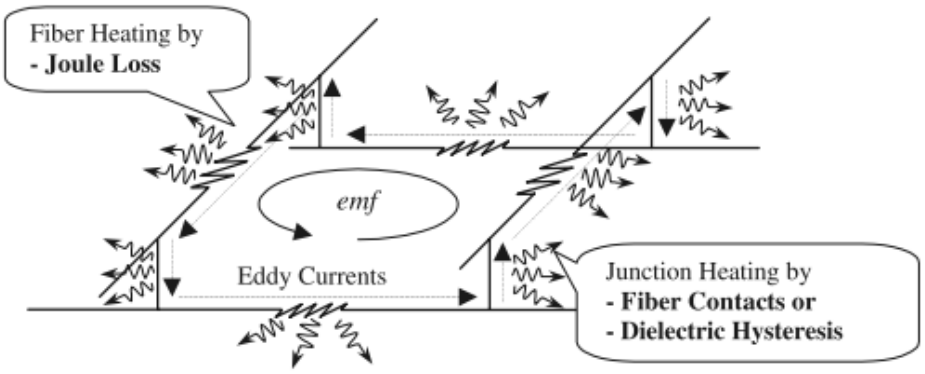


Figure 1.5: Different heating mechanisms [24]

This research focuses on a CF-PEKK material, in which the carbon fibres are conductive and the matrix is a dielectric thermoplastic polymer. Induced currents will run through the fibres, which have a certain resistance. Using Ohm's law, one can compute the amount of power that will be dissipated due to this resistance. Equation 1.6 [18] shows that Joule losses are a function of the induced current $I$, the fibre resistivity $R_f$ and the length $l_f$ and cross-sectional area $A_f$ of the fibre.

$$P = I^2 R_f = I^2 \frac{\rho_f l_f}{A_f} \tag{1.6}$$

At a certain point, the induced current will change direction and will have to 'jump' from fibre layer to fibre layer. When the fibre layers are in contact with each other, a certain junction resistance will exist at the location where the eddy current goes from one ply to the other. Again using Ohm's law, one can derive the power dissipated at such junctions. Equation 1.7 [25] shows this power dissipation, based on the induced current $I$ and the junction contact resistance $R_{jc}$.

$$P_{jc} = I^2 R_{jc} \tag{1.7}$$

The value for the junction contact resistance will have to be measured experimentally. Heat could also be generated due to dielectric heating. The matrix PEKK is a dielectric material, meaning induced (in the presence of an electric field) or permanent dipoles are present inside the material. Heating of the matrix could happen due to polarisation effects [26]. Different forms of polarisation exists, which are itemised below [26].

- **Distortion polarisation:** This is an induced form of polarisation that occurs either due to the displacement of electrons around their nuclei or the displacement of the atomic nuclei relative to the molecular chain.
- **Orientation polarisation:** Permanent dipoles inside the matrix will align with the applied electric field.
- **Interfacial polarisation:** This is also called Maxwell-Wagner polarisation and arises from a charge build-up between interfaces in a homogeneous material.

Heating due to distortion polarisation occurs at frequencies in the Tera-Hz regime [27], due to the small masses of electrons and nuclei. Heating due to orientation polarisation, also known as dipolar heating, occurs due to

the interaction a permanent dipole has with its environment. Interfacial polarisation heating, also known as Maxwell-Wagner heating, happens at the interfaces between materials [26]. Charge carriers move through the carbon fibres induced by the changing magnetic field. At the interface between carbon fibre and matrix they can become trapped due to the limited conductivity of the matrix. When the fibres from individual plies are not in direct contact, potential differences can occur causing dipolar heating [28]. The power loss due to the dielectric heating mechanism for a non-magnetic material is given in Equation 1.8.

$$P_{av} = \omega \varepsilon_0 \varepsilon_{eff}^{''} E_{rms}^2 V \tag{1.8}$$

The power loss depends on the angular frequence $\omega$, the permittivity of free space ($\varepsilon_0$), the effective permittivity loss factor ($\varepsilon_{eff}^{''}$), the root-mean square value of the electric field $E$ and the volume $V$ over which the alternating electric field acts. The permittivity or dielectric constant indicates the amount of energy that a material can store and the permittivity loss factor is an indication of how much energy is lost due to the generation of heat. A complete expression for the effective permittivity loss factor is given in Equation 1.9 [26], which includes the heating mechanisms of, dipolar- ($\varepsilon_d{''}(\omega)$), electronic- ($\varepsilon_e{''}(\omega)$), atomic- ($\varepsilon_a{''}(\omega)$), Maxwell-Wagner ($\varepsilon_{MW}{''}(\omega)$) -polarisation next to heating due to conduction ($\frac{\sigma}{\omega\varepsilon_0}$).

$$\varepsilon_{eff}{''}(\omega) = \varepsilon_d{''}(\omega) + \varepsilon_e{''}(\omega) + \varepsilon_a{''}(\omega) + \varepsilon_{MW}{''}(\omega) + \frac{\sigma}{\omega\varepsilon_0} \tag{1.9}$$

The complete expression for the complex permittivity of a material is given in Equation 1.10 [26]. The ratio of the effective loss factor over the dielectric constant is called the effective loss tangent.

$$\begin{aligned} \varepsilon^* &= \varepsilon' - j\varepsilon_{eff}{''} \\ \tan(\delta_{eff}) &= \frac{\varepsilon_{eff}{''}}{\varepsilon'} \end{aligned} \tag{1.10}$$

The generation of heat depends on several different material properties discussed in the current section. These material properties will either be measured experimentally or be taken from literature. Next to the generation of heat, the distribution of heat also plays an important role with induction heating.

### 1.2.3. THERMODYNAMICS

Due to the dissipation of power, the material will start increasing in temperature. The relation between heat and temperature is given in Equation 1.11 [29].

$$Q = C\Delta T = mc\Delta T \tag{1.11}$$

The equation shows the specific heat $c$ of the material, the mass $m$ and the temperature $T$. Within the laminate, heat conduction will take place, conducting the heat throughout the material. The conduction of heat can be modelled with Fourier's equation of conduction, Equation 1.12 [29]. Where $k$ is the thermal conductivity, $A$ the area and $\frac{dT}{dx}$ the temperature change through the material distance.

$$\frac{dQ}{dt} = H = -kA\frac{dT}{dx} \tag{1.12}$$

When the outer surfaces of the laminate are in contact with the surrounding air, heat convection will take place. Heat convection can be approximated with the help of Newton's law of cooling, given in Equation 1.13 [30, 31]. The relation between surface flux $q_s''$, surface temperature $T_s$, ambient temperature $T_{\text{inf}}$ and heat transfer coefficient $h$ is made.

$$q_s{''} = h(T_s - T_\infty) \tag{1.13}$$

The heat transfer coefficient depends on the geometry of the object, the fluid properties, fluid motion and the difference in temperature. It is not a material property. Typical values for free convection of gasses are, $h \approx 5-30\ [W/(m^2K)]$[30]. The last form of heat transfer is through radiation. Stefan-Boltzmann's law describes the net radiated power that an object emits in ambient temperature and is given in Equation 1.14 [31].

$$P = e\sigma_B A\left(T^4 - T_a^4\right) \tag{1.14}$$

In which $e$ is the emissivity constant of the material, $\sigma_B$ is the Stefan-Boltzmann constant and equals $\sigma \approx 5.67 \cdot 10^{-8}$ $[W/m^2 \cdot K^4]$, $A$ is the area that is emitting radiation and $T_a$ the ambient temperature in Kelvin. The emissivity of carbon fibre plastics is taken to be equal to 0.95 and independent of temperature [20, 32–35]. This is an approximation; in reality the emissivity is temperature-dependent.

### 1.2.4. PROCESS PARAMETERS

There are several process parameters that influence the heat generation during induction heating. Controlling the temperature of the laminate is crucial for the final quality of the weld [17, 36]. Material degradation will occur when temperatures are too high, whilst too low temperatures cause weak bonds due to limited polymer chain interdiffusion over the bond interface [36]. There are several process parameters that can be adjusted by the user, which influence the temperatures generated in the workpiece.

By adjusting any of the parameters related to the generation of the changing magnetic flux, one indirectly controls the temperature occurring in the workpiece. The design of the coil [19, 20, 37–42], the generator power settings [19, 20, 39, 43] or by making use of flux concentrators [40, 44–48], will cause a change in magnetic flux strength. The shape and length of the copper coil not only dictates the magnetic flux strength but also influences the resonance frequency at which the current will go through the coil. The longer the coil, the lower the generator output frequency. This frequency has an effect on the skin depth, given in Equation 1.15. The skin depth is defined as the distance at which the magnetic field power equals 1/e of the power output at the surface of the laminate.

$$\delta_s \approx \left( \frac{2}{\omega \mu_r \mu_0 \sigma} \right)^{1/2} \tag{1.15}$$

Equation 1.15 shows the skin depth, angular frequency, relative permeability, permeability of free space and the electric conductivity of the material, $\delta_s$, $\omega$, $mu_r$, $\mu_0$ and $\sigma$ respectively. The lower the skin depth, the harder it is for the magnetic field to penetrate the material. Very conductive materials will thus act as reflectors. Different coil shapes will result in different magnetic fields and different skin depths.

Next to the coil shape, one can also alter the generator power settings. Changing the power settings, changes the current going through the copper coil and the angular frequency at which the current oscillates [19, 20, 39, 43]. Increasing the power settings, increases the magnetic field strength.

A different way to influence the magnetic flux is by making use of flux controllers [40, 44–49]. Figure 1.6 shows the proximity effect and flux concentrator and their influence on the magnetic field lines and current distribution in conductors.

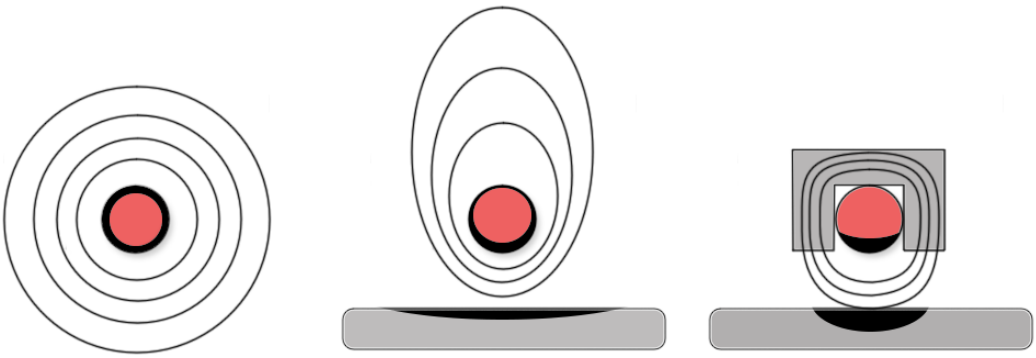

(a) No effects (b) Proximity effect (c) Flux concentrated

Figure 1.6: Depiction of the proximity effect and usage of flux concentrators [22]

Figure 1.6a shows the cross-section of a solid circular coil through which an alternating current is fed. With alternating currents, the current (black area over the coil geometry) will always reside on the outer edges of the conductor, describing the skin effect [49]. When a conductive load is placed in the vicinity of the coil, the current will primarily flow near the surface facing that conductive load [49], shown in Figure 1.6b. The magnetic field is distributed accordingly. Figure 1.6c shows the usage of a flux concentrator. The flux concentrator provides a path for the magnetic field to follow [22, 49]. The current through the coil will now primarily

flow near the open surface and the magnetic field is directed towards the workpiece more locally, generally increasing heating efficiency [49]. Flux concentrators are usually produced from steel laminates, ferrites or magneto-dielectric materials [44]. They differ in permeability and saturation flux density [44]. Applying optimal coil design, generator power settings and using flux controllers, one can accurately use induction heating in a power-efficient manner [45, 46].

Next to altering the magnetic flux strength, one can also look at the distance between coil and laminate as well as the properties of the laminate itself. The distance between the coil and laminate is known as the coupling distance. The closer one places the coil to the laminate, the faster the laminate heats up [19, 20, 39, 40, 43]. This has everything to do with the increase of the magnetic field strength, as given by the Biot-Savart's law in Equation 1.5. The constituents of the laminate also influence the production of heat during induction. Rudolf et al. [19] showed the influence of weave-type and Duhovic et al. [43] showed the influence of the thickness of the laminate on the heat generation. The micro-structure and the electric material properties influence the generation of eddy currents. The geometry of the laminate could also cause an edge effect to occur, which is depicted in Figure 1.7.

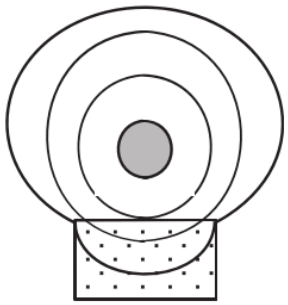

Figure 1.7: Edge effect [40]

The edge effect is caused by a change in electromagnetic field which is caused due to the edges of the workpiece. A difference in permeability and permittivity will cause the electromagnetic waves to propagate in a different manner and this can cause a concentration of heat generation near the edges of the laminate [40].

Last, one could choose to actively cool the laminate during induction heating. The objective of induction welding is to have the maximum temperature occurring at the bond line. Based on Biot-Savart's law however, the magnetic field is strongest at the outer surface of the laminate facing the coil. In order to have the maximum temperature at the bond line, one could apply cooling in the form of blowing air (increasing convection) or by applying heat sinks, which conduct the heat away [23, 43, 50]. Next to cooling of the laminate, cooling of the coil is also an important factor [51]. The coil will be water-cooled, to prevent an excessive temperature increase. This elongates the expected lifetime of the coil [51].

### 1.2.5. MODELLING

The previous section showed the different process parameters that influence the generation of heat and their effect on the final quality of an induction welded joint. Simulating the problem enables one to research these process parameters cost- and time-efficiently. Several analytical and computational models already exist in literature.

Miller et al. [52–54] were one of the first to analytically model the heat generation in graphite composites during induction heating. Miller focused on Joule losses and used Faraday's and Ohm's law to find the power dissipation in the fibres. Agreement between simulation and experimental results for woven materials was found. However, for UD lay-up materials results differed. Fink et al. [55–58] focused on UD lay-up cross-ply carbon fibre composites and assumed dielectric heating to be the primary form of heating, not included by Miller et al. The matrix was modelled as a resistor and capacitor in parallel. Experimental and model results agreed, confirming the assumption of dielectric heating. Both CF-Poly(Ether-Ether-Ketone) (PEEK) and CF-Poly(Ether-Imide) (PEI) [59] were researched. Yarlagadda et al. [25] focused on a UD lay-up CF-PEEK material and proposed a method for determining the dominant heating principle, instead of assuming the dominant

heating principle beforehand. It confirmed that junction heating for UD lay-up composites is dominant, but also showed a distinction between woven and UD lay-up materials. With woven materials, the fibres are in relatively close contact, reducing junction resistance or any matrix effects which could be present for UD lay-up materials. Finally, Kim et al. [24] combined the model proposed by Fink et al. and Yarlagadda et al. and included all three heating mechanisms instead of focusing on one. Kim et al. looked at UD lay-up CF-PEI material both cross- and angle-plied. The results emphasised the important dependency of heating on the material properties and process parameters.

Analytical models found in literature have modelled UD lay-up carbon fibre materials but all were focusing on a simplified Helmholtz coil. Changing coil geometry will make the analytical model very complex very fast.

Instead of analytically modelling the problem, one could also look at computational models. Several different researches have been performed, investigating the induction heating phenomenon of CFRPs. Almost all of the research was focused on the woven CF-PPS [34, 35, 38, 39, 42, 43, 50] or woven CF-PEEK [20, 50, 60, 61] material.

Mitschang et al. [35] investigated the thermal behaviour of woven CF-PPS during continuous induction heating with the help of a 2D model, written in ANSYS. Ideal process parameters were determined with the help of the model, focusing on coil velocity, the distance between coil and consolidation roller and the pressure applied by the roller. Later research [50] investigated the effect of cooling the outer surface on the temperature distribution through the thickness for both woven CF-PPS and woven CF-PEEK materials. Without altering the mechanical performance of the bonds, surface cooling resulted in increased processing speeds. Most recent work of Mitschang et al. [62] looked at a woven CF-PA66 material and simulates the thermal behaviour with the help of COMSOL. Next to air cooling, a flux concentrator is used and again the coil feed speed and the distance between coil and consolidation roller were investigated, resulting in a process diagram. The model was able to predict void development, material degradation and lap shear strength of lap shear bonds.

Duhovic et al. [34, 43] also focused on actively cooling the outer surface in order to shift the maximum temperature location from the outer surface to the bond line. A computational model was written with which the process parameters for both static and continuous induction heating of a woven CF-PPS material could be evaluated. Process parameters that were investigated were laminate thickness, coupling distance and generator power. Both works of Mitschang and Duhovic show similar trends. Active cooling shifts the maximum temperature towards the bond line and optimised settings can be found based on material requirements. Optimised processing settings for induction heating of a woven CF-PPS material were used to manufacture a stiffened panel by Pappada et al. [38, 39, 42]. C-scans of the panel showed the success of applying continuous induction welding, having only small debonded areas near the edges of the laminate.

Lionetto et al. [61] produced a similar processing window for induction welding woven CF-PEEK laminates. This research set itself apart by looking into the phenomena of heat transfer, melting and crystallization, which was not considered in earlier research.

All in all, most of the research regarding computationally modelling the induction heating phenomenon focuses on woven materials. O'Shaughnessey et al. [10] looked into UD CF-PPS but incorporated a stainless steel metal mesh in order to maximise the temperature at the bond line. A three-dimensional model was written in COMSOL and the influence of mesh size and current input were investigated.

No literature was found that describes a computational model with which the susceptorless induction heating phenomenon is investigated for a UD-layup material. This gap in knowledge is exactly where this research will focus on. It will focus on susceptorless induction heating of UD CF-PEKK material and will try to model the thermal behaviour with the help of a computational model.

### 1.2.6. CONCLUSION LITERATURE STUDY

There are multiple process parameters which influence the behaviour of laminates during induction heating. Controlling the temperature increase directly influences the quality of the bond. For this, a computational model can be used which can predict the ideal processing window based on these process parameters in a cost- and time-efficient manner. Based on the theory behind induction heating, several different process and material properties are needed to be able to run the electromagnetic and thermal analyses. The different parameters are given in Table 1.2.

Table 1.2: Input parameters computational model

| Parameter | Unit | Description |
|---|---|---|
| **Miscellaneous** | | |
| w, l, t | [m] | Width, length and thickness geometry[1] |
| I | [A] | Current excitation |
| f | [Hz] | Current frequency |
| $T_0$ | $[^oC]$ | Initial temperature |
| $t_{end}$ | [s] | Total duration transient analysis |
| $t_{inc}$ | [s] | Step size transient analysis |
| **Material properties electric** | | |
| $\rho(x,y,z,T)$ | $[\Omega \cdot m]$ | Electric resistivity tensor as a function of temperature [1] |
| $\epsilon'$ | [-] | Relative permittivity constant laminate |
| $\epsilon''_{eff}$ | [-] | Relative permittivity loss factor laminate |
| $\mu_r$ | [-] | Relative permeability scalar [1] |
| **Material properties thermal** | | |
| $k(x,y,z,T)$ | $[W/(m \cdot K)]$ | Thermal conductivity tensor as a function of temperature[1] |
| $c$ | $[J/(kg \cdot K)]$ | Specific heat capacity material[1] |
| $D$ | $[kg/m^3]$ | Density material[1] |
| $h$ | $[W/(m^2 \cdot K)]$ | Heat convection laminate boundaries |
| $e$ | $[-]$ | Emissivity material [1] |

[1] For Laminate, coil, air and optional: heat sink

Because the material under investigation is a non-ferromagnetic material, the relative permeability is assumed to be equal to one and independent of temperature.

Analytical models exist in literature that deal with induction heating of UD lay-up CFRPs. These are however often based on simplified coils and lay-ups. When one wants to include complex coil shapes, active cooling or even using flux concentrators, analytical models become very complex very fast. The more complex induction heating set-ups can be modelled with the help of computational models based on FEM. Several authors have modelled the induction heating process with help of FEM, but only for either woven materials or for using suscpetor materials at the bond line. This research will try to fill the gap and will try to computationally model the thermal response of the UD lay-up CF-PEKK material to an alternating magnetic field. Next to that, it will go into what is actually happening in a UD lay-up composite material when it is subjected to a changing magnetic flux. An understanding of what is happening inside the laminate is of crucial importance, because it is needed for computationally modelling the entire heating process.

## 1.3. PROJECT PLAN

From the literature study and motivation, a research objective and research questions have been developed. These are based on the wishes of the company and on the lack of knowledge found from literature for modelling induction heating of UD lay-up materials.

### 1.3.1. OBJECTIVE AND RESEARCH QUESTIONS

The objective of the research project is to contribute to the knowledge on induction heating of UD lay-up CF-PEKK composites. This is done by investigating the heating behaviour of UD CF-PEKK laminates and by simulating this behaviour with the help of a computational model. From the objective, the following main research question has been formulated.

*"What is the influence of the laminate lay-up, fibre orientation and the inherent electrical properties of fibre and matrix of an UD CF-PEKK laminate on the heat generation during induction heating and how can one model this behaviour?"*

The main research question can be divided into two sub-topics, with each their own sub-research questions.

1. Which heating principle is dominant in the heating of UD lay-up CF-PEKK laminates?

- What is the thermal response of the material when subjected to a changing magnetic flux?
- What are the influences of the UD fibre ply orientations on the electrical properties of the laminate and how could one quantify these properties?
- How do the thermal response and electric properties relate to the micro molecular structure of the laminate?
- How do the results from these experiments relate to the heating principles?

2. Is it possible to model the electromagnetic induction heating of UD CF-PEKK laminates and accurately predict temperatures within an error limit of 10%?

    - What are the different methods of modelling this problem?
    - What are the input properties needed for modelling induction heating of UD CF-PEKK laminates?
    - Is it possible to accurately model the heating patterns occurring for the different UD CF-PEKK laminates heated by the coils investigated?
    - What are the differences between the computational model and the results obtained by heating experiments when comparing heating patterns?
    - Is it possible to accurately model the temperatures occurring for the different UD CF-PEKK laminates heated by the coils investigated?
    - Can the model be validated?
    - How should the computational model be adjusted in order to get a validated model?

### 1.3.2. METHODOLOGY

In order to answer the main research question, heating experiments will be performed on different UD CF-PEKK laminates with different coils. The heating response of different laminate lay-ups will be recorded with the help of a thermal camera. The results should clarify how the material behaves in the vicinity of an altering magnetic field source. Images are expected to show the locations of maximum heating, based on laminate lay-up and fibre orientation. The electrical properties of the material will be measured in the three principal directions. This gives an understanding of the current paths available in the material and the resistances the currents will encounter when going in these directions. Together with the thermal images, the electric material properties are to be used to explain the heating behaviour of the UD CF-PEKK material. With the help of a light microscope, the micro-structure of the material is investigated in order to help explain the electric properties found in the principal directions. These should shed light on whether currents are capable of going perpendicular to the fibre direction. A computational model will be written that can model the behaviour seen during induction heating experiments. The research will be concluded by analysing heating results obtained through experiments and will compare these with the results found with the computational model. The goal is to have the computational model be able to predict the electromagnetic response of the material. This is the first and most important step towards having a computational tool to optimise induction welding.

## 1.4. REPORT OUTLINE

This report will give clear descriptions of all of the experimental set-up used, in Chapter 2. Material properties and laminate production procedures are also included. Chapters 3 and 4 will try to answer the first sub-research question. Chapter 3 visualises the electromagnetic response of the UD CF-PEKK material and includes the influence of laminate lay-up and fibre orientation. Chapter 4 goes into the electric characteristics of the material and tries to link this to the thermal response of Chapter 3. Chapter 5 will answer the second sub-research question and includes a detailed description of the computational model build in Comsol. Validation of the model takes place by using the experimental data found in Chapter 4. This report is concluded in Chapter 6.

# 2
# EXPERIMENTAL SET-UP

Numerous different experimental set-ups have been used during this research. These are experiments into finding the primary cause for the generation of heat within the Carbon Fibre (CF)-Poly(Ether-Ketone-Ketone) (PEKK) material. And experiments used to find the material properties needed for modelling induction heating. These experimental set-ups will be described in the current chapter.

## 2.1. MATERIAL

The material used for this research is a CF-PEKK laminate with a Uni-Directional (UD) lay-up. The laminates were manufactured by Fokker, using the prepreg from TenCate. The properties of the prepreg are given and temperature dependent thermal material properties needed to model the induction heating physics are discussed separately.

### 2.1.1. PREPREG MATERIAL PROPERTIES AND LAMINATE MANUFACTURING

The laminates that will be used for this research have been made of CF-PEKK prepreg. The carbon fibre is an AS4 Polyacrylonitrile (PAN) based fibre and the PEKK matrix is a dielectric semi-crystalline thermoplastic polymer. Figure 2.1 shows the molecular structure of the matrix PEKK. It is part of the Poly(Aryl-Ether-Ketone) (PAEK) family, just like Poly(Ether-Ether-Ketone) (PEEK) [63]. In order to decrease the melting temperature and crystallisation rate, various PEKK copolymers can be mixed together. These are known as Terephthaloyl (T) and Isophthaloyl (I) and the T/I ratio of PEKK. Different T/I ratios give different PEKK properties. As the molecular structure shows, the terephthaloyl is a straight and rigid moiety [63] opposed to the isophtaloyl moiety, which possesses a kink. These kinks influence the chain's flexibility, mobility and crystallization [63]. The PEKK prepreg used for the production of the composite plates had a T/I ratio of 70/30. Table 2.1 shows the relevant characteristics of the prepreg composite and shows the relatively high glass transition temperature [64].

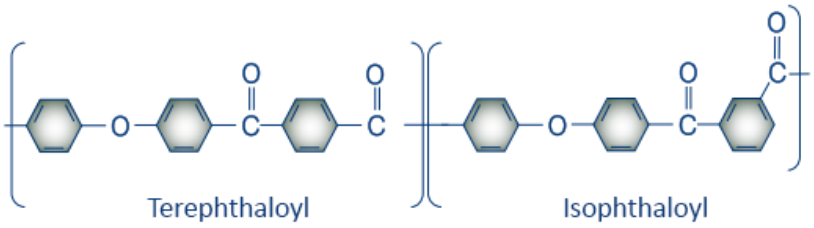


Figure 2.1: Molecular structure PEKK [65]

Table 2.1: CF-PEKK material properties

| Property | Value | Source |
|---|---|---|
| Density[1] | 1.310 $[g/cm^3]$ | [66] |
| Glass transition temperature | 159 $[^oC]$ | [67] |
| Crystallization temperature[2] | 265 $[^oC]$ | [67] |
| Melting temperature | 337 $[^oC]$ | [67] |
| Processing temperature | 360-380 $[^oC]$ | [63] |
| Dielectric constant matrix[3] | 3.6 | [68] |
| Dielectric loss matrix[3] | 0.0033 | [68] |
| Fibre volume content | 60 [%] | [66] |
| Cured ply thickness | 0.137 [mm] | [66] |
| Moisture uptake[4] | <0.2 [wt%] | [69] |

[1] Test method: ASTM D792 at Room Temperature (RT)

[2] Cooling rate = 10 $[^oC/\text{min}]$

[3] Measured at RT and 1 [kHz]

[4] 24 [h] immersion at 23 $[^o]$

PEKK has a low intake of moisture, high toughness and tensile modulus, great flammability resistance and is thermally stable [70]. Having a high glass transition temperature (PEEK = 143 $[^oC]$ [71], Poly(Phenylene-Sulfide) (PPS) = 90 $[^oC]$ [72]), enables larger temperature domains in which the material can be used. Important parameters from Table 2.1 are the dielectric constant and the dielectric loss factor. Chapter 1 showed dielectric heating to be one of the possible heating mechanisms of the material during induction heating. The amount of heat that will be generated depends on the dielectric material properties. Pan et al. [68] investigated these properties and showed that there is dependency of the dielectric properties of PEKK on the frequency of the electromagnetic field applied and on the temperature of the material. The dielectric loss factor starts increasing rapidly around a temperature of 150 $[^oC]$[68]. This might be related to the glass transition temperature of PEKK, which is also around that temperature. Softening of the amorphous regions of the semi-crystalline polymer could influence the dielectric properties of said polymer [73].

Numerous consolidated UD lay-up CF-PEKK plates were available within Kok en Van Engelen (KVE) for the use of testing. These were manufactured by Fokker, with the prepreg material coming from TenCate. The consolidated plates were manufactured with the help of the autoclave cycle of Figure 2.2a and the bagging instructions of Figure 2.2b.

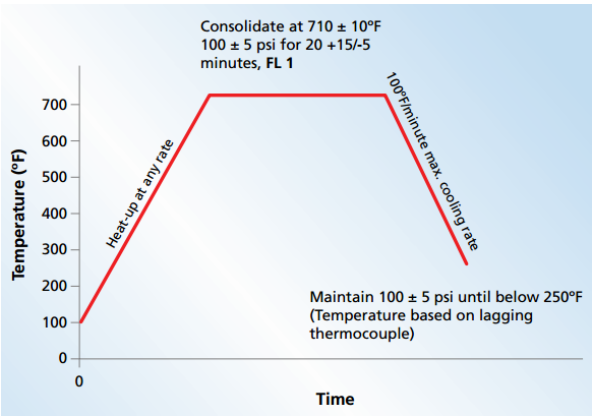


(a) Autoclave cycle used to manufacture Fokker laminates [66]

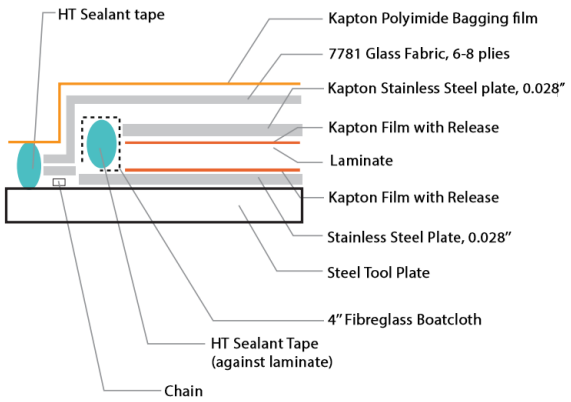


(b) Bagging instructions Fokker laminates [66]

Figure 2.2: Manufacturing characteristics consolidated Fokker laminates

Table 2.2 shows the consolidated plates that were used during this research. Each of the laminates are 300x300 [mm] in width and length and approximately 1.1 [mm] in thickness (except for UD-9).

Table 2.2: Available consolidated plates

| Material blank number | Lay-up | Lot number | Roll number |
|---|---|---|---|
| UD-3 | $[0]_{4S}$ | 012014-1TP1-4 | 4 |
| UD-4 | $[0,90]_{2S}$ | 012014-1TP1-4 | 4 |
| UD-5 | $[45,-45]_{2S}$ | 012014-1TP1-4 | 4 |
| UD-6 | $[45,-45,0,90]_{S}$ | 012014-1TP1-4 | 4 |
| UD-9 | $[45,-45,0,90]_{2S}$ | 012014-1TP1-4 | 4 |

The table shows that the laminates are manufactured from the same batch. With the prepreg coming from the same batch, the prepreg can be considered a constant factor between the different laminates manufactured. All laminates have the same thickness, except for the UD-9 laminate, which has a thickness of approximately 2.2 [mm].

### 2.1.2. THERMAL CONDUCTIVITY

In order to be able to model the induction heating physics, several thermal properties of the material are needed. With the current research focused on the electric properties, the thermal properties are either taken from literature, or have been measured using the material from Table 2.2. The thermal material properties needed to model the induction heating of the CF-PEKK laminates are the thermal conductivity, the specific heat and the density of the material with respect to temperature. The thermal conductivity in fibre direction, $k_{cL}$, has been measured by the company Experta. The transverse thermal conductivity, $k_{cT}$, was computed based on the rule of mixtures and the results from Experta, shown in Equation 2.1.

$$\begin{aligned} k_{cL} &= v_f k_f + v_m k_m \rightarrow k_f = \frac{k_{cL} - v_m k_m}{v_f} \\ k_{cT} &= \left(\frac{v_f}{k_f} + \frac{v_m}{k_m}\right)^{-1} = \left(\frac{v_f}{\frac{k_{cL} - v_m k_m}{v_f}} + \frac{v_m}{k_m}\right)^{-1} \end{aligned} \tag{2.1}$$

In this equation, $k_{cL}$, and $k_{cT}$ are the composite thermal conductivity in longitudinal and transverse direction respectively. The thermal conductivity of the fibre and matrix and the volume contents of both fibre and matrix are included as $k_f$, $k_m$, $v_f$ and $v_m$ respectively. With $k_{cL}$ measured and by knowing $k_m$, $v_m$ and $v_f$, one is able to compute $k_f$. The fibre thermal conductivity can then be used in order to compute $k_{cT}$. The thermal conductivity of the matrix is taken from the thermal conductivity of a similar material: PEEK [74]. Figure 2.3 shows both the longitudinal and transverse thermal conductivity used in the computational model.

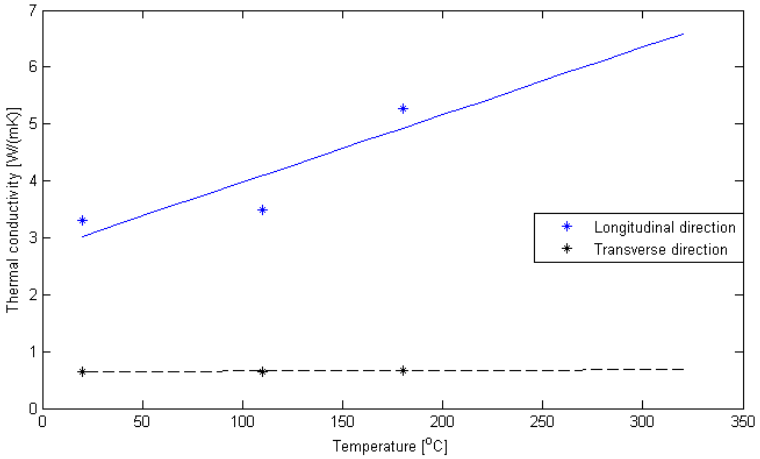


Figure 2.3: Thermal conductivity vs temperature UD CF-PEKK

A linear fit was used to find the thermal conductivity properties with respect to temperature. The assumption that the thermal conductivity will increase linear with respect to temperature is based on data for a comparable

material. Choy et al. [74] showed that the thermal conductivity of CF-PEEK increased linear in the temperature range of 300-600 [K].

### 2.1.3. SPECIFIC HEAT

Next to the thermal conductivity, the specific heat is needed, dependent on temperature. The specific heat of the material was found by using Differential Scanning Calorimetry (DSC) [75]. The test is based on heating the CF-PEKK material with a controlled rate and comparing this with a reference material. The reference material is a Sapphire standard with known specific heat. The difference in heat flow is then used to compute the specific heat of the CF-PEKK sample. Both the sample and the Sapphire standard will be placed in an aluminium holder with an aluminium lid placed on top. Because the aluminium will influence the heat flow, an empty measurement on the aluminium holder and lid is included. The $[45,\text{-}45,0,90]_S$ laminate was used to produce samples with a diameter of approximately 5 [mm] and a weight of 8 [mg]. A diamond blade saw was used to cut a total of three square samples of 5x5 [mm]. Sanding paper (300P) was used to create a round sample of 8 [mg] in weight. Equation 2.2[75] is used to compute the specific heat of the sample material.

$$E = \left[b\left(Wst \cdot Cp(st)\right)\right] / (60 \cdot Dst) \tag{2.2a}$$

$$Cp(s) = \frac{60 \cdot E \cdot Ds}{Ws \cdot b} \tag{2.2b}$$

Equation 2.2a shows one how to compute the calorimetric sensitivity needed in order to find the capacity of the samples. In Equation 2.2a, $b$, $Wst$, $Cp(st)$ and $Dst$ stand for the heating rate $[^oC/min]$, the mass of the Sapphire standard [mg], the specific heat capacity of the Sapphire standard [J/(g·K)] and the vertical displacement between the sapphire DSC thermal curve and the specimen holder [mW] respectively. A heating rate of 10 $[^oC/min]$ was used to heat the samples. The mass of the Sapphire standard is 9.8 [mg] and the specific heat capacity of the Sapphire standard is included in Figure 2.4b. The distance, $Dst$, is visualised in Figure 2.4a. It is the difference between the curves of the empty holder+lid and the Sapphire standard. The calorimetric sensitivity is used in Equation 2.2b to compute the specific heat $Cp(s)$ of the sample. This equation also includes $Ds$ and $Ws$, which stand for the vertical displacement between the curves of the empty holder and sample [mW] and the mass of the sample [mg] respectively. A total of three samples were tested. The masses of samples 1, 2 and 3 equalled 8.7-, 8.2- and 8.7 [mg] respectively. The measured heating rates with respect to temperature are given in Figure 2.4a. The average calculated specific heat of the CF-PEKK material is given in 2.4b.

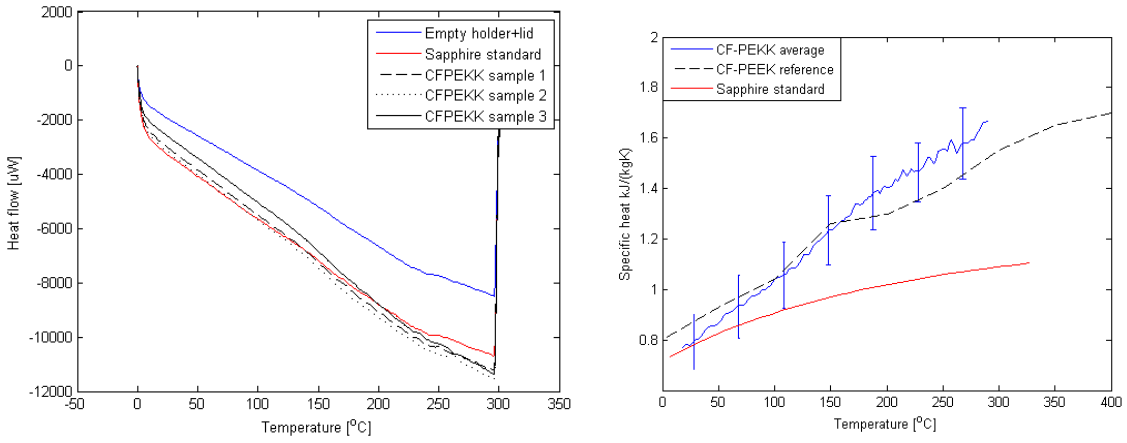


(a) Thermal curves empty holder, sapphire standard and samples

(b) Specific heat CF-PEKK, CF-PEEK and Sapphire standard

Figure 2.4: Computed specific heat UD CF-PEKK

In order to compare the computed specific heat, a reference material was added. This is a quasi-isotropic CF-PEEK material, made with APC-2 prepreg [32]. It shows how the results found for the CF-PEKK specific heat are similar to the specific heat of the CF-PEEK material.

### 2.1.4. DENSITY

The final thermal material property needed is the density with respect to temperature. In order to include the temperature dependent behaviour of the density, the density of a similar material was used as input to the computational model. This is the density of a UD CF-PEEK material [32] with equivalent fibre volume content. The temperature dependent density is given in Figure 2.5.

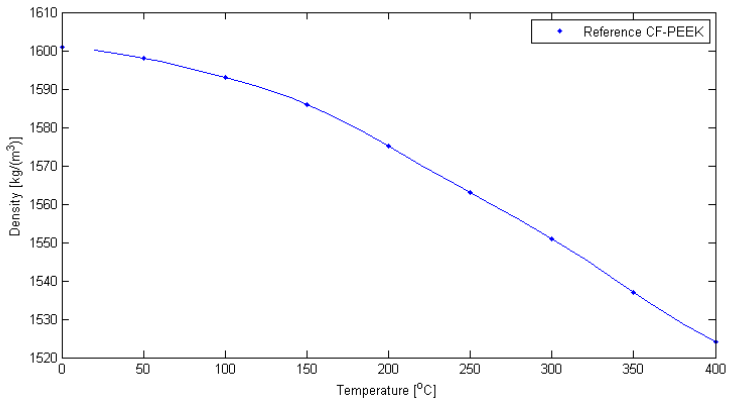


Figure 2.5: Density vs temperature CF-PEEK

## 2.2. SAMPLE MANUFACTURING

For the induction heating experiments as well as for the measurement of material properties, samples will be manufactured. The samples shall be obtained from the consolidated laminates from Table 2.2. These laminates are approximately 300x300 [mm] in width and length. It was decided that samples with a size of 200x200 [mm] in width and length will be used for the induction heating experiments. This makes the samples large enough to be able to neglect any edge effects from the sample's ends, as well as have enough material left to manufacture samples for obtaining the electric material properties. The samples for the induction heating experiments will be cut to size with the help of a Darley Guillotine Shear cutter. One aspect to keep in mind is the fact that cutting the laminate by shearing could cause local delaminations. Because the samples for induction heating were taken large enough to also avoid these kinds of edge effects, this will not pose a problem.

The samples used for obtaining the electric material properties will be cut to size with the help of a Proth cutting and grinding machine. A diamond blade saw will separate the material and will ensure the edges of the samples to be parallel to one another. The individual steps taken and the settings used on the Proth machine are included in Appendix B. After the samples have been cut, the samples are dried using compressed air. In order to ensure electrical contact between carbon fibres and copper terminals, the ends of the samples are disposed with a small layer of gold. First, ends of the samples are sanded with a very fine grain in order to expose the carbon fibres. Sanding paper grade P320 and P1000 were used to expose the carbon fibres and remove loose fibres. After sanding, the samples are cleaned with the help of a Bandelin Sonorex ethanol bath and are immersed for about 10 [s]. The samples are then dried using compressed air, paying special attention to the edges of the samples. Before gold sputtering the samples, tape is applied to the areas where no gold should be deposed. Last, the samples are placed in a gold sputtering machine and a small gold layer is sputtered onto the ends of the sample. Gold is a good conductor and will not be affected by oxidation effects. Gold is sputtered at a rate of 15 [nm/min] with the help of a SCD 040 Balzers union gold sputtering machine. Trial and error showed a duration of 15 [min] per side is sufficient to get a smooth gold layer.

## 2.3. INDUCTION HEATING SET-UP

Heating experiments will be performed on the consolidated plates from Table 2.2. A picture of the induction heating set-up is shown in Figure 2.6.

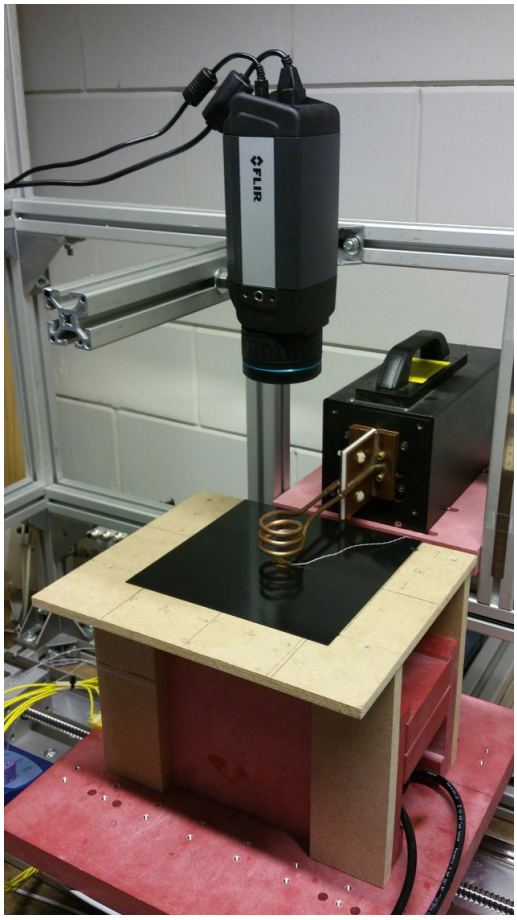


Figure 2.6: Induction heating set-up TU Delft

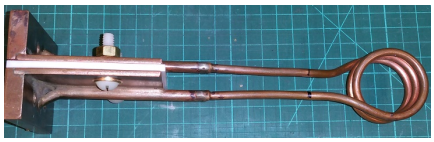

(a) Horizontal 3-turn Helmholtz coil

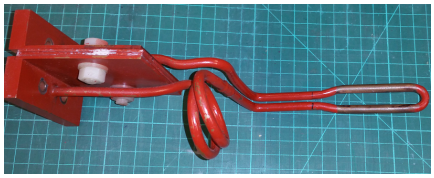

(b) Hairpin coil

Figure 2.7: Different coils used for heating experiments

A wooden platform has been manufactured to support the laminate samples and to ensure the samples are in the same position every experiment. Wood will not be affected by the alternating magnetic field. The wooden platform only supports the laminate at its edges, preventing the conduction of heat from the laminate through the wood. The dimensions of the wooden platform are included in Appendix D. Type E thermocouples have been used to measure the temperatures. Type E is made from a non-ferromagnetic material (chromel-constantan) and will less be affected by the alternating magnetic field in comparison with a type K thermocouple [76]. These thermocouples have been positioned both on top and on the bottom of the sample. A FLIR A655sc Infrared (IR)-camera is used to record the heating patterns during heating. A picologger is used to store all of the data from the thermocouples. The picologger, IR-camera and power generator are all connected to a computer with which the entire process is controlled.

The copper coils are connected to an Alternating-Current (AC)-generator which is water cooled. The generator is an Ambrell EasyHeat, provided by KVE. One can adjust the amperage or power at which heating will take place, and the duration of heating. The generator is an Easyheat LI edition, capable of delivering up to 8.3 [kW] of power. The maximum current that can be applied is 750 [A]. In this research, the amperage and duration are altered with discrete steps. Ambrell automatically computes the resonance frequency. The frequency is not a parameter that can be set and will always be in between 150-400 [kHz] [77]. Different coils have been used in order to investigate the heating behaviour of the laminates. The focus is on the two coils shown in Figure 2.7. These coils are used to investigate the effect of fibre orientation on the heat generation. The dimensions of the Helmholtz and Hairpin coils have been included in Appendix E.

## 2.4. Resistance measurement set-up

The electric resistivity of the material is one of the properties needed in order to model induction heating. For this, a resistance measurement set-up available at the TU-Delft is used. Figure 2.8 shows a schematic of this

measurement set-up. It is based on a four-wire resistance measurement method using a Keithley 2701. The Keithley is capable of measuring resistances in a domain from 100 [$\mu\Omega$] to 120 [$M\Omega$] [78]. With the four-wire method, two wires are connected to the Keithley 2701 multimeter and are used as input wires, carrying the current that goes through the sample. The other two copper wires are known as the sensing wires, measuring the voltage difference over the sample locally. When the measured resistance of the samples is below 1 [$k\Omega$], it is advised to use the 4-wire method over the 2-wire method [78]. The method of measuring the resistance is by utilising a constant-current method. The Keithley sources a constant current to the resistance and measures the voltage [78]. The constant current equals 1 [$mA$] and the impedance of the voltmeter is very high (>10 [$G\Omega$] [78]. This results in almost all of the current flowing through the sample.

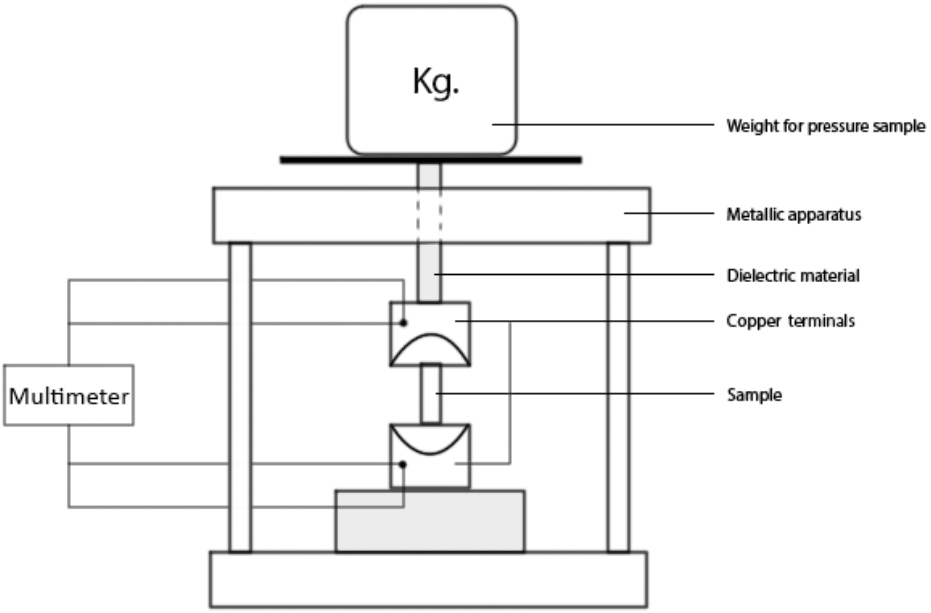


Figure 2.8: Test jig for conductivity measurement

A varying amount of weight will be placed on top of the apparatus which ensures a constant pressure to reside over the sample. A total of five masses were available, each having a mass of approximately 1 [kg]. This pressure improves the contact area between copper terminals and the ends of the sample. Increasing the pressure, decreases the resistance measured. The relation between clamping pressure and electrical resistance will be investigated in Chapter 4.

The entire test jig is small enough to be placed completely inside an oven. This enables measurements to be performed at increased temperatures. A Keithley 2701 multimeter is used to store all of the data from the resistance test jig and thermocouples type K for the temperature measurements. The oven used, a Thermo Hereaus, is capable of reaching temperatures of 250 [$^oC$]. This temperature encompasses the glass transition temperature and should thus include the possible non-linear effects on the electric conductivity of the material. No ovens were available that could reach the melting process of the CF-PEKK samples.

## 2.5. DIRECT-CURRENT HEATING EQUIPMENT

Knowing the current path through the material is of key importance, because it gives insight into how the material could behave during induction heating. Next to that, knowing how the current goes through the samples during resistance measurements, gives insight into which material properties are actually being measured. In order to visualise this current path, the samples will be heated using a Direct-Current (DC) generator. The generation of heat will be recorded with the help of the FLIR IR-camera. The measurement jig from Figure 2.8 is directly attached to a Basetech BT-305 DC power supply, which is capable of providing a 0-30 [V] and 0-5 [A]

output range. The current output was set to 5 [A] and the voltage was automatically set by the power supply, depending on the resistance of the sample. Due to the current, the samples will heat up rapidly and this heat can be recorded by the FlIR IR-camera. Figure 2.9 shows the DC heating set-up.

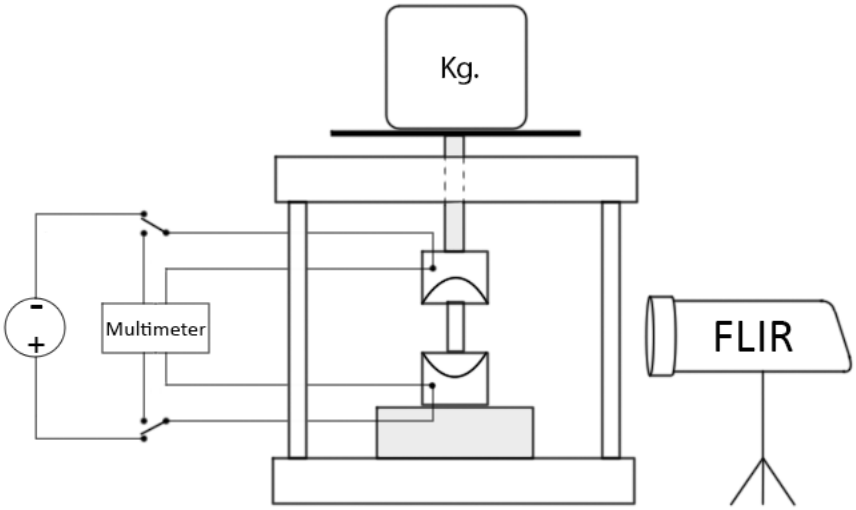


Figure 2.9: Direct current heating set-up

The IR-camera is attached to a computer that contains the FLIR utility program. Due to the fact that heat is conducted through the material during heating, only the instantaneous heating response will be used. This means that the power supply will only be connected to the measurement set-up only for approximately one second. The IR-camera used is a FLIR a655sc, capable of digital data streaming of up to 25 [Hz] with the USB-connection, which was used during this research [79].

## 2.6. MICROSCOPY SET-UP

In order to get an understanding of what is happening inside the laminate during induction heating, it is desirable to know the micro-structure of the laminates. The micro-structure will be examined with the help of a light microscope. This is a Leica DM LM light microscope connected to a computer via a Zeiss Axiocam ICc 5. This enables one to digitally analyse the microscopic images. Figure 2.10 shows the light microscope.

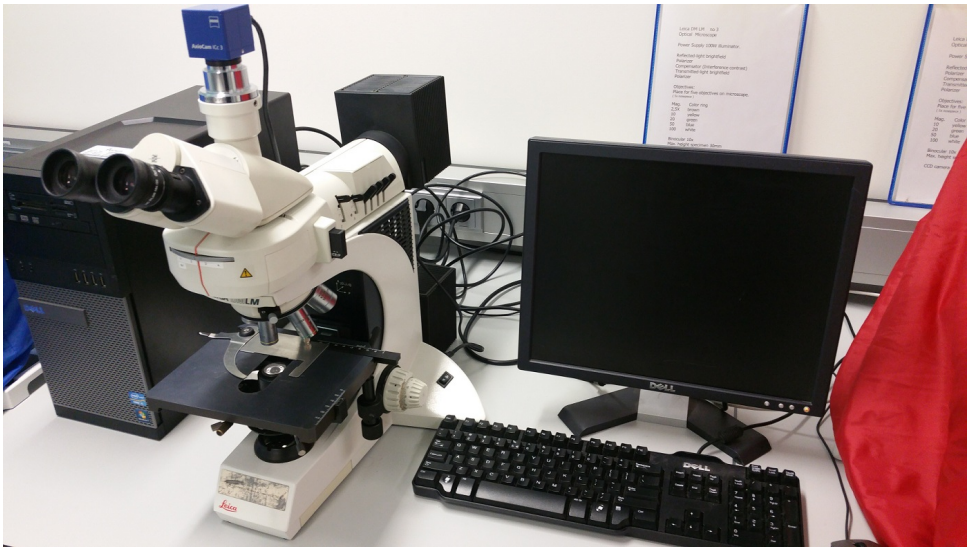


Figure 2.10: Microscopy set-up

The objectives attached to the microscope range from 2.5-100x magnification. This research will only use up to 10x magnification in order to view the micro-structure of the laminates.

The samples used for analysis will be cut with the help of a diamond blade saw positioned in the Struers Secotom-10 [80]. The ends of the samples will be sanded and polished with the of the Struers Pedemin DAP-7 polishing machine. In order to keep the samples in place and have straight edges, the samples will be immersed in a polymer matrix. This is a two-component cold curing thermoset that cures when the Technovit 4071 powder is mixed with the Technovit 4071 liquid. The complete description of manufacturing the samples and using the light-microscope is added in Appendix C.

# 3

# THERMAL IMAGING

The first step into finding out what the primary heating source is during induction heating of Uni-Directional (UD) Carbon Fibre (CF)-Poly(Ether-Ketone-Ketone) (PEKK) laminates, is to place them in the vicinity of an alternating magnetic field and record their thermal response. By using different coils, different lay-ups and by altering the fibre orientation with respect to the coil, one can get a clear view of what the thermal response of the material is and how this relates to the laminate lay-up and orientation. The coupling distance and surrounding conditions were kept as constant as possible between the different heating experiments. Because the laminate samples had to be re-used, the maximum temperature was kept below the glass transition temperature of CF-PEKK. A coupling distance of approximately 10 [mm] was chosen in order to prevent thermal degradation of the material. The laminates were heated for 15 [s] in order to see the instant and transient heating behaviour of the material. The transient thermal behaviour after turning off the power was also recorded. The measurement set-up of Section 2.3 will be used to do the thermal imaging experiments.

A total of three different lay-ups were tested, heated by two different coils. The layups $[0]_{4S}$, $[0,90]_{2S}$ and $[45,-45,0,90]_S$ were heated by both the horizontal Helmholtz and Hairpin coils. The influence of fibre orientation and coil geometry was taken into account by rotating the laminate with respect to the coil over the angles $45-$ and $90[deg]$. The horizontal Helmholtz coil will force the current to follow a loop-like circuit inside the laminate. The Hairpin coil forces the current to follow a more linear circuit path, enabling one to investigate the influence of fibre orientation on the thermal response.

## 3.1. LAMINATE LAY-UP $[0]_{4S}$

With all of the fibres going in the same direction, it was expected that the amount of heat that would be generated was going to be limited. This due to the increased resistance the current has to overcome going perpendicular to the fibre. Figure 3.1 shows the heating results when the laminate is subjected to the alternating magnetic field of the horizontal Helmholtz coil for the three different orientations. It shows the heating pattern after 15 [s] of heating at an amperage of 399 $[A]$ and resonance frequency of 346 $[kHz]$.

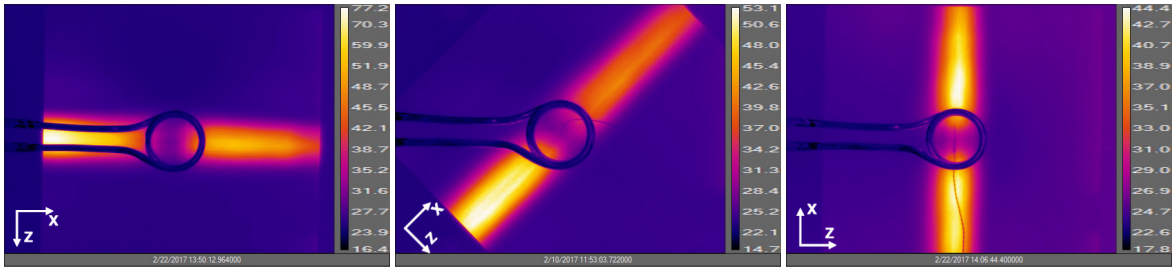

(a) $\alpha = 0[deg]$ (b) $\alpha = 45[deg]$ (c) $\alpha = 90[deg]$

Figure 3.1: Results heating experiments $[0]_{4S}$ laminate with Horizontal Helmholtz coil at 400 [A]

The figure shows that heating of the $[0]_{4S}$ laminate does take place, creating a narrow band over which heat is generated following the direction of the fibres. The fibres in the laminate are oriented along the x-axis (from left to right for Figure 3.1a). Increased heating at the edges of the laminate can be witnessed for the orientations $\alpha = 0[deg]$ and $\alpha = 45[deg]$, which can be explained by the geometry of the coil. The copper rods connected to the centre of the coil will also generate a magnetic field, increasing the flux at the edges over which the connecting rods reside. The temperature scales of the IR-camera are included but will not be used to quantify heating.

The Helmholtz coil forces the current in the laminate to follow the shape of the excitation current going through the coil itself. The law of induction dictates that the alternating magnetic flux generated by the coil is opposed by the eddy currents going through the laminate. The eddy currents will try to mirror the currents in the coil. However, due to the orientation of the fibres and the non-conductive behaviour of the matrix, the path the eddy currents can follow deviates from this mirroring path. The different orientations are created by rotating the laminate over a positive angle of either 45- or 90 [deg]. The heating images seem to indicate that at the locations where the eddy currents want to go perpendicular to the fibre direction (in z-direction), heating is maximised. Whether this is due to an increased resistance originating from fibre-fibre contacts in transverse direction, or if this is due to a displacement current originating from the dielectric properties of the matrix, will be answered by looking at the electric properties of the material in Chapter 4. The reason for the heating pattern to stretch all the way from sample's end to sample's end is expected to be caused by the much larger electric resistance perpendicular to the fibre compared to the electric resistance parallel to the fibre.

By also recording the transient thermal behaviour of the laminate after the power was turned off, a deeper understanding of the conduction of heat throughout the material could be made. Figure 3.2 shows the difference between the thermal images taken after 15 [s] of heating and 15 [s] after the power was turned off for the $[0]_{4S}$ laminate. The laminate is heated by the Helmholtz coil and was under an orientation of $\alpha = 90[deg]$. The fibres within the laminate are always oriented along the x-axis.

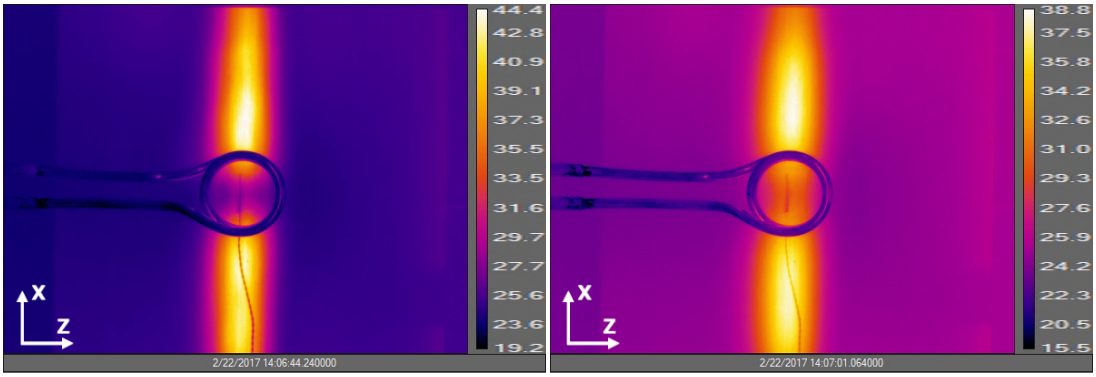


(a) At end of heating

(b) 15 [s] after end of heating

Figure 3.2: Transient thermal response $[0]_{4S}$, Helmholtz coil, 400 [A], $\alpha = 90[deg]$

Figure 3.2 clearly shows how the heat is spread out primarily in the direction of the fibre. Initially, no heat was generated at the centre of the coil. However, the heat is conducted to the centre of the coil by the carbon fibres. The figures also indicate the limited heat conduction in the direction perpendicular to the fibres. This corresponds to the thermal conductivity of the material given in Chapter 2. The laminate cools down gradually due to the radiation and convection of heat over the free surfaces of the laminate. Rotating the laminate, rotates the heating pattern, but does not influence the transient thermal response of the material.

To compare the generation of heat for the different laminate orientations, the increase in temperature recorded by the thermocouples will be used. Figure 3.3 shows the locations of the different thermocouples and the related temperatures measured for the $[0]_{4S}$ laminate under an orientation of $\alpha = 0[deg]$ heated by the Helmholtz coil. Appendix I includes the exact locations for all of the thermocouple locations used in the different thermal imaging experiments.

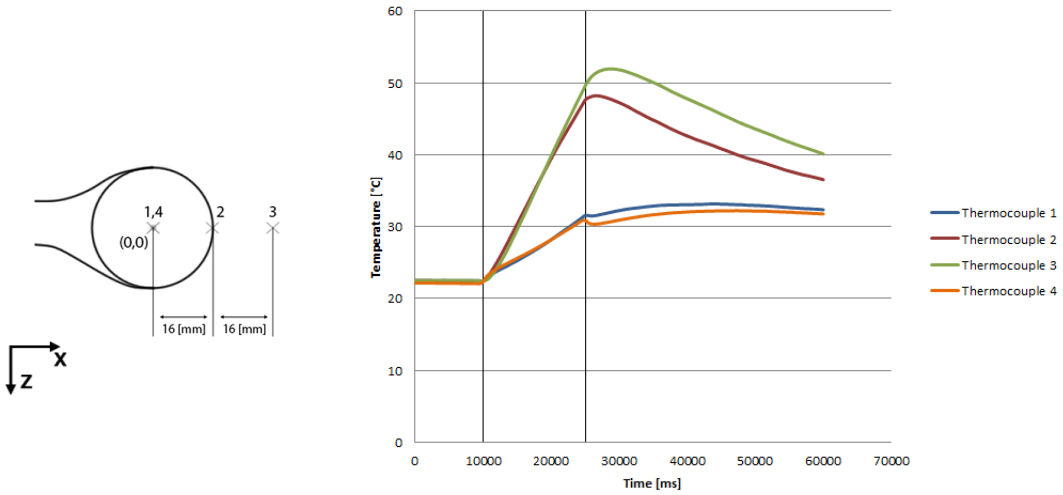


(a) Thermocouple positions

(b) Thermocouple temperatures

Figure 3.3: Thermocouple locations and temperatures $[0]_{4S}$ laminate, $\alpha = 0[deg]$, $I = 400[A]$

Figure 3.3b shows the temperatures of the thermocouples with respect to time. The solid vertical lines represent the start and the end of the heating phase, which has a duration of 15 [s] in total. A total of four thermocouples have been used, with the maximum temperature measured by thermocouple 3. Thermocouples 1,2 and 3 are located on the bottom of the laminate and thermocouple 4 on the top, relative to the coil. There is only a limited difference between the top and bottom thermocouple, witnessed for all different heating experiments. The difference is however non-significant. Figure 3.3b shows the temperature increasing even after turning off the generator power. This effect is stronger for thermocouples 1 and 4. This can be explained by the conduction of heat within the laminate, as shown in Figure 3.2. When the thermocouples are not located in the area of maximum heating, heat conduction throughout the laminate causes the increase in temperature after the power has been turned off. The heating experiments have been performed at different amperage settings. Increasing the amperage through the coil increases the maximum temperatures measured for the different thermocouples.

Because the location of maximum temperature is not constant, one can only compare the temperatures occurring at the centre of the coil at the top and bottom of the laminate for the different orientations. These locations will always be fixed relatively to the coil. Figure 3.4 shows the temperatures occurring for the different orientations.

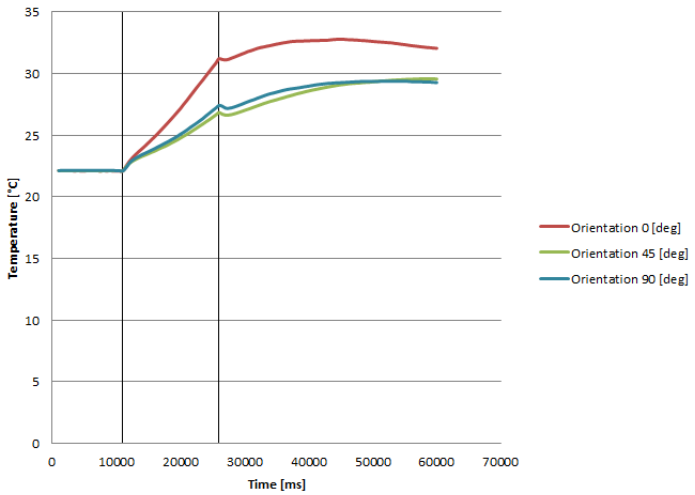


Figure 3.4: Temperatures thermocouple 1 $[0]_{4S}$, 400 [A], all orientations

Although the differences are small, it seems that the orientation $\alpha = 0[deg]$ gives increased temperatures for the heating of the centre of the laminate. Apparently, when the fibres are aligned with the connecting copper rods of the coil, more heat is generated. It is assumed that this has to do with the geometry of the coil. The coil does not have a constant coupling distance for the different parts of the coil's geometry. At certain positions, the coil is actually closer to the laminate. It is expected that this causes an increase in eddy currents at these particular positions. The computational model of Chapter 5 will be used in order to investigate this assumption.

Using a different coil geometry will cause a difference in the eddy current paths generated inside the laminate. As mentioned, the eddy currents want to mimic the direction of the excitation current but are limited by the orientation of the fibres. Next to the Helmholtz coil, the Hairpin coil has also been tested for all three orientations. Figure 3.5 shows the heating results for the $[0]_{4S}$ laminate under the three different orientations heated with the Hairpin coil. The coupling distance and amperage settings have been kept constant.

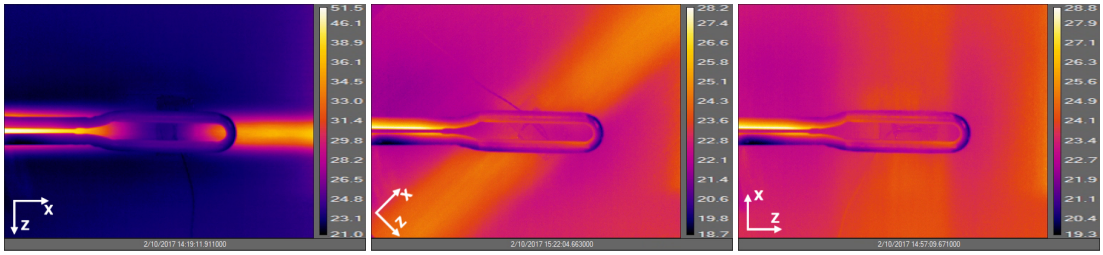

(a) $\alpha = 0[deg]$ (b) $\alpha = 45[deg]$ (c) $\alpha = 90[deg]$

Figure 3.5: Results thermal imaging experiments $[0]_{4S}$ laminate heated by Hairpin coil at 400 [A]

The heating patterns for the Helmholtz and Hairpin coil look similar for the orientation of $\alpha = 0[deg]$. The Hairpin coil also creates an area of heat generation which stretches over the entire width of the sample. Figure 3.5 also shows how with increasing orientation angle, the amount of heat being generated decreases. Thermocouple temperatures show negligible temperature increases registered for the orientations $\alpha = 45[deg]$ and $\alpha = 90[deg]$. The eddy currents have to overcome a much larger electric resistance for the orientation $\alpha = 90[deg]$. Electric resistance experiments have to be performed to find the relation between the electric resistivity in fibre-direction and transverse to the fibre direction. This could explain why the orientations of $\alpha = 45[deg]$ and $\alpha = 90[deg]$ barely heat up. The difference in coil geometry only influences the heat generation pattern. The coil geometry does not influence the conduction of heat throughout the laminate.

Based on the findings of the current section, laminates with the fibres all in the same direction can be heated up by both the Helmholtz as the Hairpin coil. Although it must be noted that the actual increase in temperature is limited. The fibre orientation with respect to the coil influences the amount of heat generated.

## 3.2. LAMINATE LAY-UP $[0,90]_{2S}$

The Helmholtz and the Hairpin coil have been used to heat up the $[0,90]_{2S}$ laminate for the orientations $\alpha = 0[deg]$ and $\alpha = 45[deg]$. The coupling distance was set to approximately 10 [mm] and the laminate was heated for 15 [s] for a variety of amperage settings. Figure 3.6 shows the instant heating behaviour of the $[0,90]_{2S}$ laminate and the Helmholtz coil for both orientations. The fibres within the laminate are oriented along the x- and z-axes. It was decided to analyse the instant heating behaviour instead of the heating pattern after 15 [s]. The instant behaviour excludes the conduction of heat and accurately shows the locations of maximum heating.

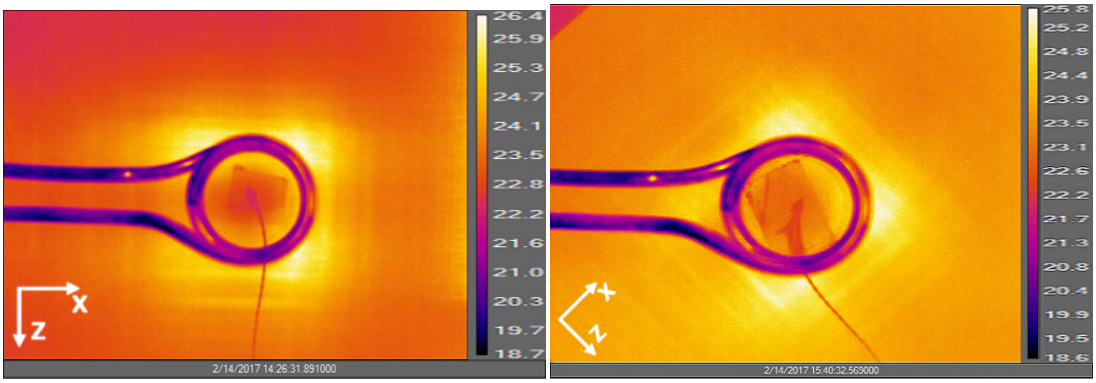

(a) $\alpha = 0[deg]$ (b) $\alpha = 45[deg]$

Figure 3.6: Results heating experiments $[0,90]_{2S}$ laminate with the Helmholtz coil at 70 [A]

The increase in temperature was much larger than what was witnessed for the $[0]_{4S}$ laminate. The current was set to 70 [A], in order to prevent thermal degradation of the material. The images show square heating paths that occur immediately after turning on the power. Heat is being generated both in the direction of the fibres and at the junction locations. Heating seems to be a superposition of all of the separate current paths that occur in the laminate, rotated with the laminate orientation. Heating is maximised at the locations where the current has to change direction. This behaviour corresponds to thermal images found in literature [24, 81]. The images show how the current will keep on following the fibre direction until it has no other direction to go but through the thickness to an adjacent ply. It is assumed this is being caused by the much larger through thickness resistance, opposed to the resistance encountered parallel to the fibre.

The transient thermal response of the $[0,90]_{2S}$ laminate has also been investigated. Since the coil and laminate orientation only influence the generation of heat and not the distribution, only a single heating experiment is analysed. Figure 3.7 shows the distribution of heat through the $[0,90]_{2S}$ laminate, heated by the Helmholtz coil, for an orientation of 0 [deg].

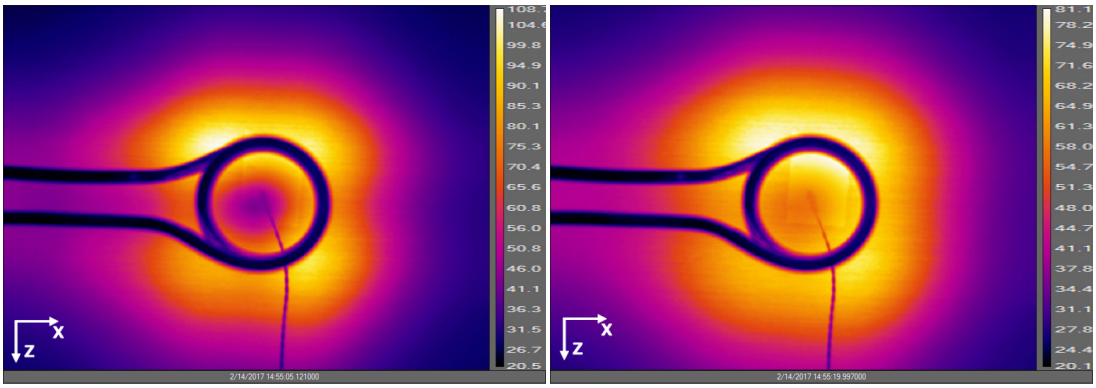

(a) After 15 [s] of heating (b) 15 [s] after end of heating

Figure 3.7: Transient thermal response $[0,90]_{2S}$, Helmholtz coil, 70 [A], $\alpha = 0[deg]$

The figures show again how the heat is primarily conducted in the direction of the fibres. The heating pattern of Figure 3.7 shows the square heating pattern due to the fibre orientations within the laminate. There is an equal amount of plies in both the 0- and 90 [deg] directions. The middle thermocouples will measure an increase of temperature after the power is turned off, due to conduction of heat from the hotter areas.

The same tests have been performed for the Hairpin coil. Because it is already known that the Hairpin coil creates a reduced magnetic field strength, higher amperages have been used to witness the heating behaviour. Figure 3.8 shows the results for both orientations at an amperage of 150 [A]. The fibres within the laminate are oriented along the x- and z-axis.

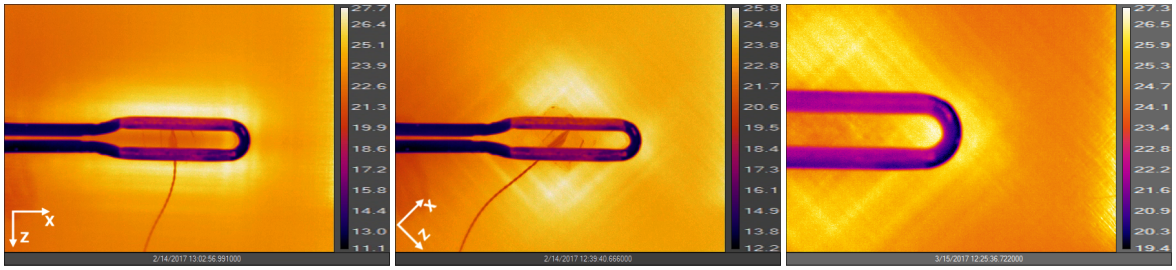

(a) $\alpha = 0[deg]$ (b) $\alpha = 45[deg]$ (c) Zoomed at the tip

Figure 3.8: Results heating experiments $[0,90]_{2S}$ with Hairpin coil at 150 [A]

It again shows the summation of square current paths occurring due to the orientation of fibres in the laminate. Most of the heat is generated at the locations where the current has to change direction, either real or by displacement currents.

In order to quantify the amount of heat being generated, the temperature increase of thermocouple 1 will be compared for both orientations and coils. The exact locations of all thermocouples for all heating experiments can be found in Appendix I. Thermocouple 1 is always located at the centre of the coil, on the bottom of the laminate. Figure 3.9a shows this temperature increase for the Helmholtz coil and Figure 3.9b for the Hairpin coil.

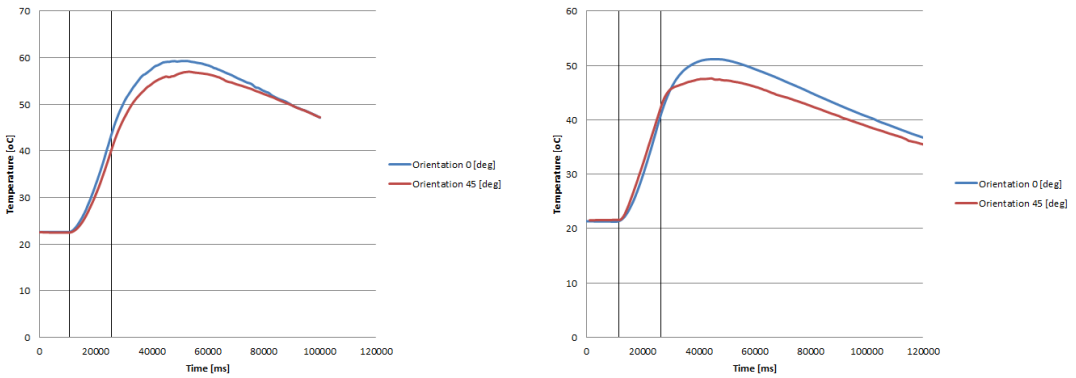


(a) Helmholtz coil at 70 [A] (b) Hairpin coil at 150 [A]

Figure 3.9: Temperatures thermocouple 1 $[0,90]_{2S}$, Helmholtz and Hairpin coil

Although small, Figure 3.9 shows that for an orientation of $\alpha = 0[deg]$, the maximum temperature increase is larger. Apparently, when the fibres are aligned with the copper rods of the coil, an increase in heat generation occurs.

The instant thermal response of the $[0,90]_{2S}$ laminate showed how there are certain current paths present during induction heating, with most of the heat being generated at the locations where the current has to change direction. The IR-images show how eddy currents tend to follow the fibre direction until the excitation current forces the eddy currents to change direction. Electric resistance experiments are to be used to compare the electric resistivity in fibre direction and through thickness direction to be able to explain this behaviour. Aligning the 0-deg fibre direction with the copper attachment rods of the coil's geometry seems to increase the maximum temperatures occurring in the laminate. This behaviour was also witnessed for the $[0]_{4S}$ laminate. It is expected to be caused by the antisymmetric geometry of the Helmholtz coil and the magnetic field vector created by the Hairpin coil.

## 3.3. LAMINATE LAY-UP $[45,-45,0,90]_S$

Finally, the thermal response of the $[45,-45,0,90]_S$ laminate has been tested using both the Helmholtz and Hairpin coils. The coupling distance is set to approximately 10 [mm] and the laminate is heated for 15 [s].

Figure 3.10 shows the immediate heating response for the Helmholtz coil and the three different orientations.

(a) $\alpha = 0[deg]$ (b) $\alpha = 45[deg]$ (c) $\alpha = 90[deg]$

Figure 3.10: Results heating experiments $[45,\text{-}45,0,90]_S$ with Helmholtz coil at 70 [A]

Although some square circuit lines are still visible, the difference between the orientations is much less pronounced as was witnessed with the $[0,90]_{2S}$ laminate. Figure 3.11 shows the transient thermal response of the laminate when subjected to the Helmholtz coil under an orientation of $\alpha = 0[deg]$.

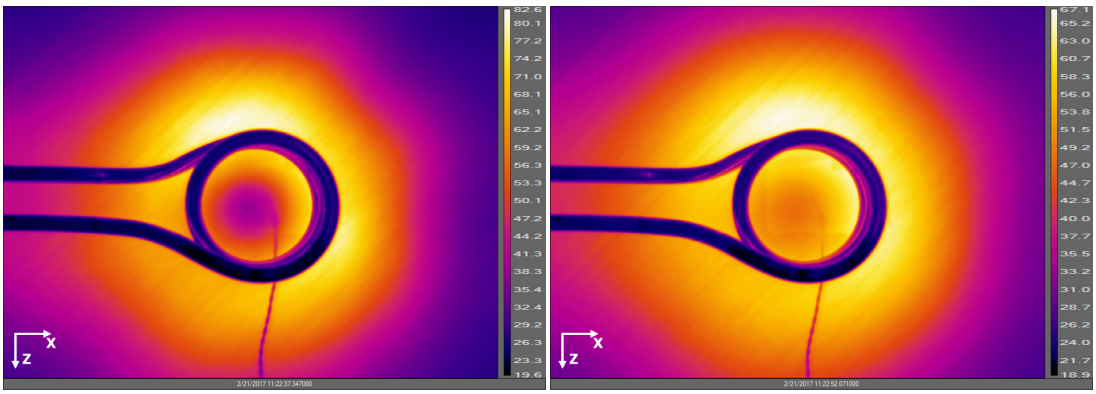

(a) After 15 [s] of heating (b) 15 [s] after end of heating

Figure 3.11: Transient thermal response $[45,\text{-}45,0,90]_S$, Helmholtz coil, 70 [A], $\alpha = 0[deg]$

Comparing these results with the results found from Figure 3.7, clearly shows how the heat is now conducted in radial direction. The thermal images indicate how the orientations of the fibres dictate the thermal conduction through the laminates.

Similar heating experiments have been performed using the Hairpin coil. Figure 3.12 shows the instant thermal response during induction heating of the $[45,\text{-}45,0,90]_S$ laminate with the Hairpin coil.

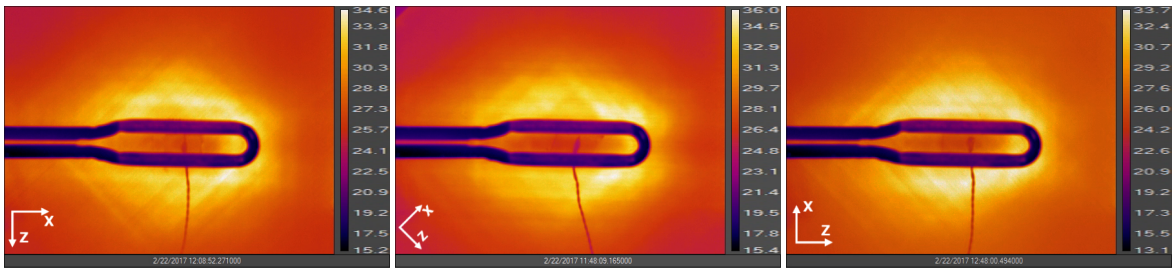

(a) $\alpha = 0[deg]$ (b) $\alpha = 45[deg]$ (c) $\alpha = 90[deg]$

Figure 3.12: Results heating experiments $[45,\text{-}45,0,90]_S$ laminate with Hairpin coil at 250 [A]

Only minor differences are witnessed with regards to the locations of maximum heating. It is assumed to be related to the outer layers of the laminate for the different orientations. Rotating the laminate with respect to

the coil does not seem to have an effect on the overall heating pattern when heating the $[45,\text{-}45,0,90]_S$ laminate with the Hairpin coil. Comparing the temperatures for thermocouple 1 and both coils is done in Figure 3.13.

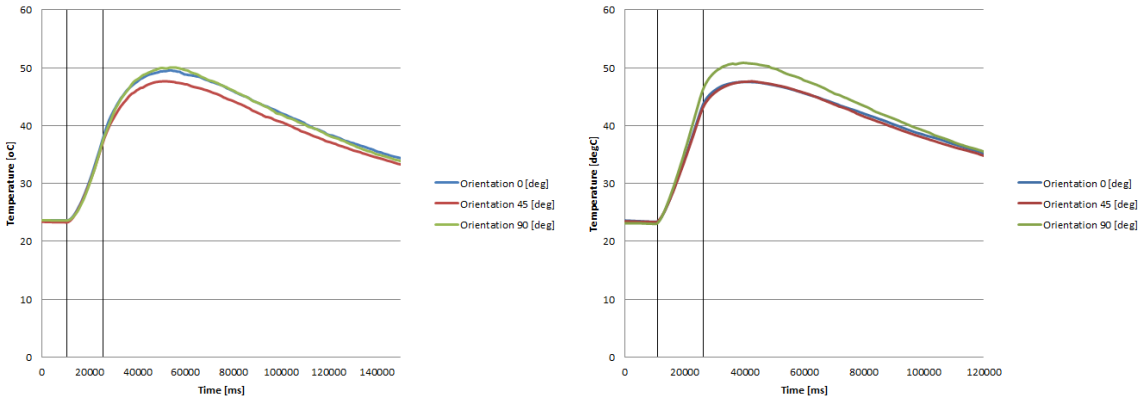


(a) Helmholtz coil at 70 [A]

(b) Hairpin coil at 150 [A]

Figure 3.13: Comparing temperatures thermocouple 1 for the $[45,\text{-}45,0,90]_S$ laminate, heated by Helmholtz and Hairpin coils

Figure 3.13a shows a reduction of 4% in the maximum temperature increase for the $[45,\text{-}45,0,90]_S$ laminate under an orientation of $\alpha = 45[deg]$. This reduced temperature increase, for the orientation of 45 [deg], was also witnessed for the other thermocouples. The computational model will be used to see whether this difference can be explained based on the electromagnetic behaviour related to the laminate lay-up. When this is not the case, the heating experiments should be re-evaluated to see whether the standard deviation, in doing experiments, could explain the difference witnessed.

An increase in maximum temperature for the orientation $\alpha = 90[deg]$ is measured for the heating experiments performed with the Hairpin coil, given in Figure 3.13b. A possible explanation can be sought by looking into the minor differences in heating patterns recorded for the different orientations. Figure 3.12c shows how the area of maximum heating is more spread out around the geometry of the coil for the orientation of $\alpha = 90[deg]$. Areas of maximum heating of Figures 3.12a and 3.12b are shifted more towards the tip of the coil. With the area of maximum heating closer to the centre, the centre will heat up quicker due to the conduction of heat.

Heating of the $[45,\text{-}45,0,90]_S$ laminate by both coils showed an almost constant heating pattern to occur in the laminate for the different orientations. Only minor differences in maximum temperature were registered for the different laminate orientations. Although the square current paths were still visible with the instant thermal behaviour, the IR-images also showed the presence of more complex current paths to occur in the quasi-isotropic laminate.

## 3.4. Conclusion

The heating experiments showed the thermal response of the UD CF-PEKK material due to a changing magnetic field for three different laminate lay-ups. The different coil geometries and laminate orientations showed the influence of fibre orientation on this thermal response. The heating of the $[0]_{4S}$ laminate showed an area in which heat was generated that stretched out over the entire width of the laminate. Square heating patterns were witnessed for the instant thermal response of the $[0,90]_{2S}$ laminate to both the Helmholtz and Hairpin coils. This behaviour was also present in the heating of the $[45,\text{-}45,0,90]_S$ laminate, but much less pronounced. A more homogeneous heating pattern was recorded for the heating of the $[45,\text{-}45,0,90]_S$ laminate, which was less affected by the laminate orientation angle $\alpha$. Heat is being conducted primarily in the fibre-directions, just as the thermal conductivity properties of the UD CF-PEKK material indicate. Electric resistance experiments will be performed to compare electric resistivity in fibre direction, perpendicular to fibre direction and in through-thickness direction. These should help in explaining the thermal behaviour of the different laminae.

# 4

# ELECTRIC MATERIAL PROPERTIES

In order to further understand the thermal responsive behaviour witnessed in Chapter 3, the electric conductivity properties of the Uni-Directional (UD) Carbon Fibre (CF)-Poly(Ether-Ketone-Ketone) (PEKK) material will be measured. These should shed light on whether the conduction of current perpendicular to the fibre is even possible. Next to using the electric conductivity values to explain the thermal behaviour of the three different laminate lay-ups, these values are necessary as an input to the computational model. The electric conductivity in fibre direction, transverse to the fibre direction and through-the-thickness direction are going to be measured. Samples made from the $[0]_{4S}$ laminate will be used to find the electric conductivity in fibre direction and perpendicular to the fibre direction. The through-the-thickness conductivity will be measured based on samples made from the $[0]_{4S}$, $[0,90]_{2S}$, $[45,\text{-}45,0,90]_S$ and $[45,\text{-}45,0,90]_{2S}$ laminates. By using the different laminate lay-ups, the influence of fibre orientation on the through-the-thickness conductivity should become apparent. The measurement set-ups from Sections 2.4 and 2.5 will be used to find the relevant material properties.

## 4.1. ELECTRIC CONDUCTIVITY IN FIBRE DIRECTION

The electric conductivity of the material can be measured using the measurement set-up of Section 2.5. Samples are cut to size and the electric resistance over the samples is measured. With the help of Equation 4.1, this resistance is then used to calculate the electric conductivity $\sigma$ of the material.

$$\sigma = \frac{1}{\rho} = \frac{1}{R\frac{A_c}{l}} = \frac{l}{Rw_c t} \tag{4.1}$$

Equation 4.1 shows how the electric conductivity $\sigma$ equals the inverse of the electric resistivity $\rho$ of the material. The electric resistivity can then be computed with the help of Ohm's law and the length $l$ and thickness $t$ of the sample. The cross-section over which the current crosses the sample has been taken as $A_c$. The distinction between sample cross-section $A_s$ and current cross-section $A_c$ has deliberately been made. Due to poor contact between samples and the copper terminals of the measurement set-up, currents do not take full advantage of the entire width of the sample. Small air gaps between the sample and the copper terminals prohibit currents from entering the sample at certain locations. The actual cross-section $A_c$ over which the current crosses the sample depends on both the positioning of the sample as well as the amount of weight placed on top of the measurement apparatus. The effect of these influences have been included in Appendix G. Weights were used to clamp the samples in between the copper terminals of the conductivity measurement apparatus. By placing weight on top of the measurement set-up, a constant clamping pressure was realised. The amount of weight used, influences the resistance measured. In order to know how much weight one should use, the relation between this weight and the resistance measured is investigated. Results are given in Figure 4.1 for three of the $[0]_{4S}$ samples. The dimensions of the samples are included in Appendix G.

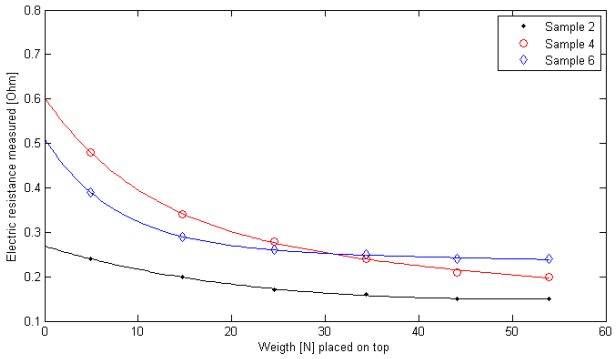


Figure 4.1: Influence pressure on resistance measurement samples $[0]_{4S}$ at RT

Figure 4.1 shows that by increasing the weight placed on top, the electric resistance decreases. By increasing the amount of weight placed on top of the apparatus, the contact between resistance sample and copper terminals is improved. It indicates that this reduction in resistance converges at a certain amount of weight. The complete list of results is included in Appendix G. Based on these findings, all of the resistance measurements were performed with approximately 50 [N] of weight pressing on the samples. Figure 4.1 already indicates that there is quite some spread in the resistances measured at 50 [N] for the different samples. It is assumed that this is also being caused by improper contact between sample and copper terminals. To prove this, Direct-Current (DC)-heating experiments have been performed and the Infrared (IR)-camera was used to record the heating of the samples. Heat is being generated due to currents going through the material. The heating images thus indicate where currents flow through the material and more importantly, where they do not. Figure 4.2 shows how the IR-camera can detect the effective width through which the current actually goes through the material.

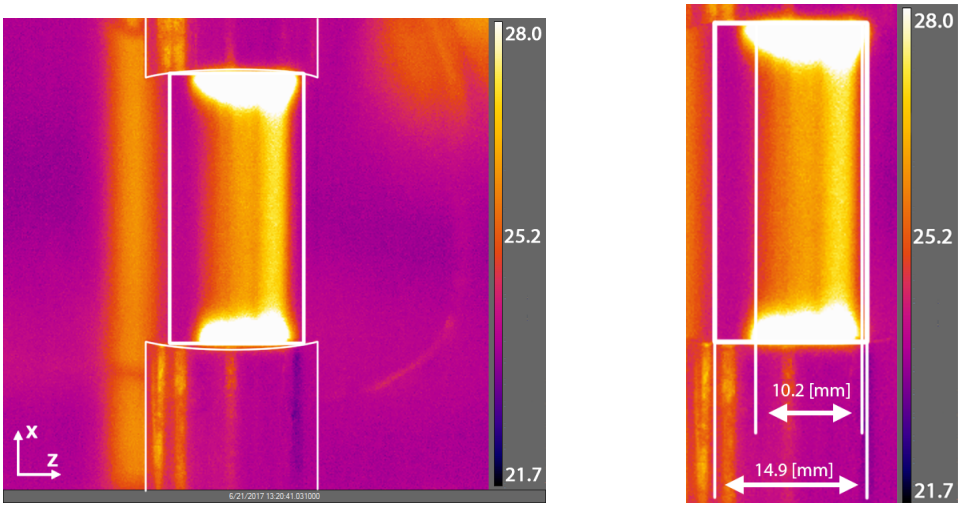


(a) Image DC heating

(b) Computing effective current width

Figure 4.2: Direct current heating images $[0]_{4S}$, Sample 3

The white lines were added to clearly show the outlining of the sample's geometry and the copper terminals. The carbon fibres are oriented along the x-axis and the current flows in the direction of the positive x-axis. Figure 4.2a shows the instant thermal response of the sample to a 5.3 [A] current going through the sample. The yellow areas indicate where the sample is heating up. Knowing that this is being caused by currents flowing through the sample, the yellow area indirectly indicates where currents are flowing through the sample and what the effective current width is. Based on the thermal response, created due to Joule heating, one can clearly see that the current indeed does not take full advantage of the entire width of the sample. With the ends of the sample sputtered with gold, the resistance is apparently still too large for the current to cross the sample over the entire width available. Basing the computation of the conductivity of the material on the

entire width of the sample would yield an under-estimation of the material's electric conductivity. By using the actual width over which the current crossed the sample, one has a better estimate of the material's true electric conductivity. Whether the current takes full use of the entire thickness of the sample is also unknown. Without a method to prove or disprove this, the entire thickness of the sample is used to compute the electric conductivity of the material.

The current used during DC-heating experiments was kept at a constant amplitude of 5.3 [A] for all the different samples. Only the instant thermal response was used, heating the samples no more than a fraction of a second. The samples reached maximum temperatures of approximately 40 [$^oC$]. By only heating for a very short time frame, thermal degradation of the material was prevented. With the help of Equation 4.1, the conductivity of the material can be calculated. The results for the individual samples are included in Appendix G. Based on these results, the average conductivity of the material in fibre direction at room temperature was calculated to be approximately equal to 18.2±3.3 [kS/m]. In literature, the conductivity of UD carbon-fibre composites ranges from 1-61 [kS/m] at Room Temperature (RT) [10, 82–90], depending on the method of measuring.

With the electric conductivity of the material dependent on temperature, resistance measurements at increasing temperatures were performed for the $[0]_{4S}$ CF-PEKK samples. Figure 4.3 shows the results for samples 3 and 5.

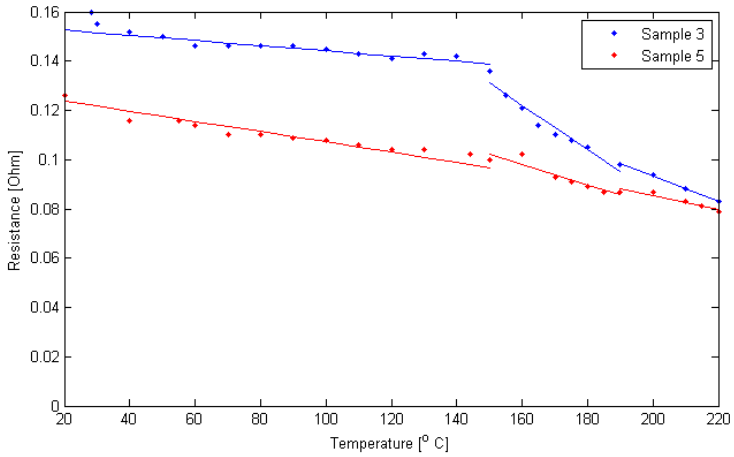


Figure 4.3: At elevated temperature

The temperature domain can be divided into three parts: before reaching glass transition temperature, around the glass transition temperature and at higher temperatures than the glass transition temperature. With the glass transition temperature approximately 160 [$^oC$], it shows a reduction in resistance measured around this temperature especially apparent for sample 3. It is expected that due to the softening of the material, the contact between copper terminals and sample is increased, reducing the resistance. This behaviour is much less apparent for sample 5. This reduction in resistance has nothing to do with the thermal response of the electric conductivity of the material, but everything with the contact area between sample and copper terminal. Sample 5 shows a much more linear and constant descending resistance measurement with respect to temperature. It is assumed that the contact between sample 5 and the copper terminals was already good enough to not be affected by softening of the material. The slope of electrical resistance of sample 5 is used to compute the resistance temperature coefficient for the $[0]_{4S}$ samples. With the help of Equation 4.2a [91], a temperature coefficient of $-1.69 \cdot 10^{-03} [K^{-1}]$ was found. The temperature coefficient can be used to compute the material's conductivity at elevated temperatures. This can be computed with the help of Equations 4.2b and 4.1.

$$\alpha = \frac{1}{R_0} \frac{dR}{dT} \tag{4.2a}$$

$$R = R_{ref} \left[1 + \alpha \left(T - T_{ref}\right)\right] \tag{4.2b}$$

At elevated temperatures, the electric conductivity of the UD CF-PEKK material in fibre direction goes up. The higher the temperature, the better the conduction of electrons.

### 4.1.1. ELECTRIC CONDUCTIVITY TRANSVERSE TO FIBRE DIRECTION

In order to find out whether currents are able to go into the transverse fibre direction, samples were cut from the $[0]_{4S}$ laminate under an orientation of 90 [deg]. The dimensions of the samples have been kept equal to those used for the measurements in fibre-direction. The influence of the position of the sample with respect to the copper terminals has again been investigated. Results showed however, that for the $[90]_{4S}$ samples, the positioning had negligible influence on the resistances measured. The same was witnessed for the influence of the amount of weight placed on top of the measurement equipment. Increasing the weight from 0 to 50 [N] reduces the average resistance of the samples measured by only 0.5%. The dimensions of the samples together with all of the experimental results found for the $[90]_{2S}$ samples, can be found in Appendix G. The reason for these factors having less of an influence on the resistances measured can be explained by the fact that these resistances are of a different order of magnitude, when compared to the $[0]_{4S}$ samples. Due to the much higher resistance in transverse direction, the current will make use of the full width of the sample to cross the material. By utilising the entire width of the sample, the resistance the current encounters is minimised. This behaviour was also recorded with the thermal camera. Figure 4.4 shows the thermal images obtained for two of the samples tested. This heating behaviour was recorded for all of the samples tested.

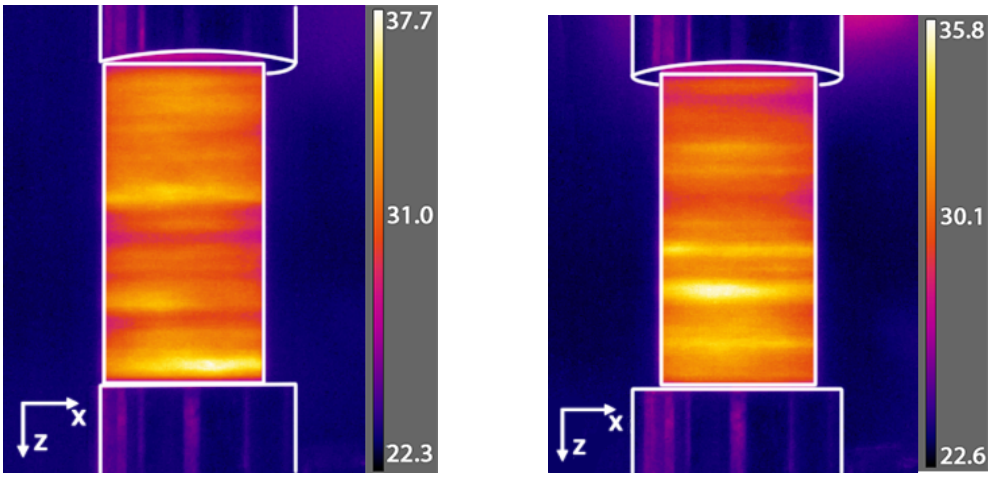


(a) Sample 2 (b) Sample 3

Figure 4.4: DC Heating images $[90]_{4S}$ samples

The white lines represent the outer edges of the samples and copper terminals. The fibres are oriented along the x-axis and current goes in the negative z-axis. Due to the increased resistances, the current takes advantage of the entire width of the sample, even though the contact between sample and copper terminals is expected to be as bad as with the $[0]_{4S}$ samples. This explains why the clamping weight and positioning of the samples have much less of an influence on the resistances measured. The current uses the entire cross-section of the sample, being less dependent on the contact between sample and copper terminals. Appendix G gives the results of the resistances measured for all of the different $[90]_{4S}$ samples. The average transverse conductivity of the CF-PEKK material equals approximately 12.6±2.3 [S/m]. In literature, the transverse conductivity of UD CF composites ranges from 0-250 [S/m] [10, 82–90]. The electric conductivity in transverse direction is approximately a factor 1400 smaller than the electric conductivity in fibre direction.

The temperature-dependent behaviour for three of the $[90]_{4S}$ samples has been measured. The results are given in Figure 4.5.

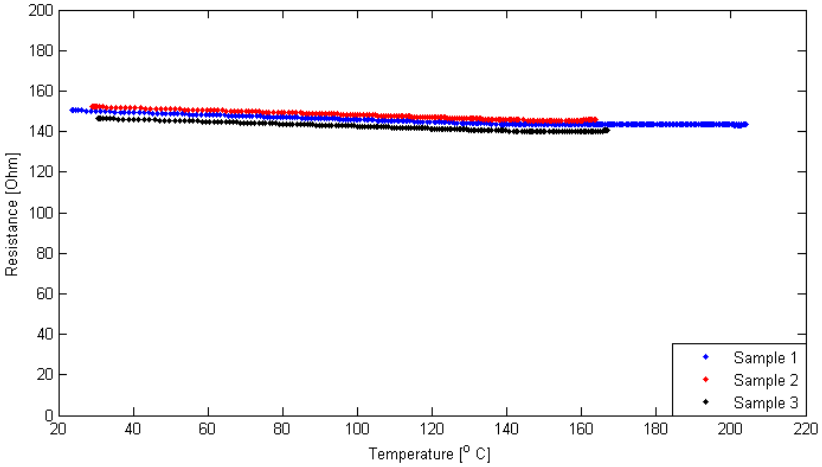


Figure 4.5: Temperature dependent resistance measurement results $[90]_{4S}$ samples

Figure 4.5 shows that the resistance is approximately constant with respect to temperature. Using Equation 4.2a, an average temperature coefficient of resistance of $-0.38 \cdot 10^{-03}$ $[K^{-1}]$ was found. The small temperature coefficient in combination with the large resistances measured in transverse direction makes the electric conductivity in transverse direction for the UD CF-PEKK approximately constant with respect to temperature.

### 4.1.2. THROUGH-THE-THICKNESS ELECTRIC CONDUCTIVITY

The electric conductivity in through-the-thickness direction for the $[0]_{4S}$, $[0,90]_{2S}$, $[45,-45,0,90]_{S}$ and $[45,-45,0,90]_{2S}$ laminates was measured. All laminates were included in order to see the effect of the lay-up on the electric conductivity of the laminate. A total of ten samples were tested for each of the laminate lay-ups. The dimensions of the samples were kept constant between the lay-ups and were approximately 6x6 [mm]. The influence of positioning the samples between the copper terminals as well as the influence of the applied pressure over the samples was again investigated. Appendix G gives all of the raw data and shows how the positioning of the sample and the pressure over the sample have almost no influence on the resistances measured. The average through-the-thickness electric conductivity for the different laminate lay-ups are given in Table 4.1.

Table 4.1: Results through-the-thickness electric conductivity at room temperature

| Laminate lay-up | Electric conductivity $[S/m]$ |
|---|---|
| $[0]_{4S}$ | 1.0±0.1 |
| $[0,90]_{2S}$ | 0.7±0.1 |
| $[45,-45,0,90]_{S}$ | 0.6±0.1 |
| $[45,-45,0,90]_{2S}$ | 0.6±0.1 |

Table 4.1 shows the influence of the laminate lay-up on the through-the-thickness material conductivity. All relative values are approximately a factor 10 smaller than the transverse conductivity of 12.6 [S/m] measured for the UD CF-PEKK material. The results of Table 4.1 help in explaining the heating behaviour of the $[0,90]_{2S}$ laminate seen in Chapter 3. Square heating patterns occurred due to the much smaller conductivity in through-thickness direction with respect to the conductivity in fibre direction. The path of least resistance will include as little jumps through-the-thickness as possible. This will create square circuits inside of the laminate, heating up the laminate through Joule losses. At the corners of these squares, heating is maximised due to the much smaller electric conductivity encountered when going through the thickness.

The through-the-thickness conductivity ranges between 0 and 1 [S/m]. Comparing these values with values found in literature, one can see that the through-the-thickness conductivity in literature ranges between 0-250 [S/m] for UD CF composites [10, 82–90]. Table 4.1 shows how the laminate lay-up influences the conductivity of sample in through-thickness direction. It is expected that the relative adjacent fibre angles within the laminate lay-ups influence the through-the-thickness conductivity of the material. By examining the microstructure of the material, one should get a clear view of why the through-the-thickness conductivity depends

on the laminate lay-up.

The electric properties of the material in through-the-thickness direction were also measured dependent on temperature. The results for the $[0,90]_{2S}$ lay-up are given in Figure 4.6.

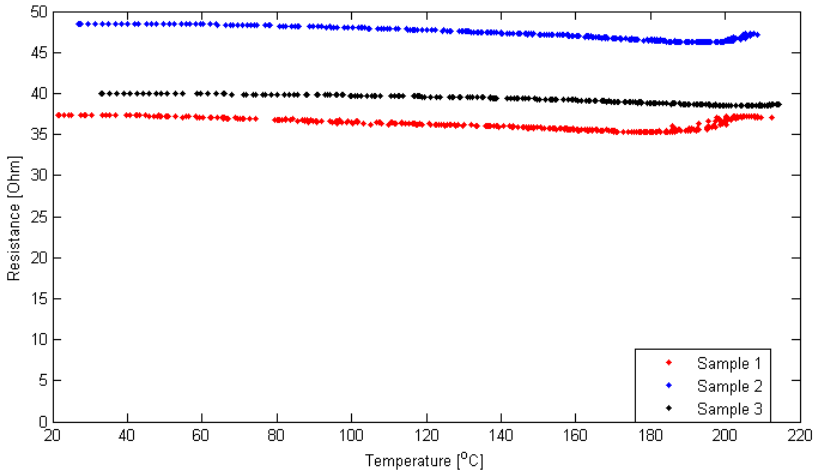


Figure 4.6: Temperature dependent behaviour $[0,90]_{2S}$ samples

The temperature dependent behaviour shows a slight reduction in resistance measured up until a temperature of approximately 200 $[^oC]$, at which this resistance increases slightly for the three different samples. Crystallisation of the matrix could explain the increase in resistance at certain temperature levels. It is expected that the resistance will decrease again once the crystal structure melts. Using Equation 4.2a, the temperature coefficient of resistance up until this point equals approximately $-0.30 \cdot 10^{-03} [K^{-1}]$. The temperature coefficient of resistance in through-thickness direction is similar to the value found in transverse direction.

The measurement results show an influence of relative fibre orientations on the through-the-thickness conductivity of the laminate lay-up. Examining the micro-structure of the material should give insight into where this difference is originating from.

## 4.2. MICRO-STRUCTURE

Conductivity measurement results showed how the current is able to go through-the-thickness of the material as well as in transverse direction to the fibre. In order to prove that this is due to fibre-fibre contact, the micro-structure is analysed with the help of the experimental set-up of Section 2.6. The cross-sections of the $[0]_{4S}$ and $[0,90]_{2S}$ laminates have been visualised and are given in Figures 4.7 and 4.8.

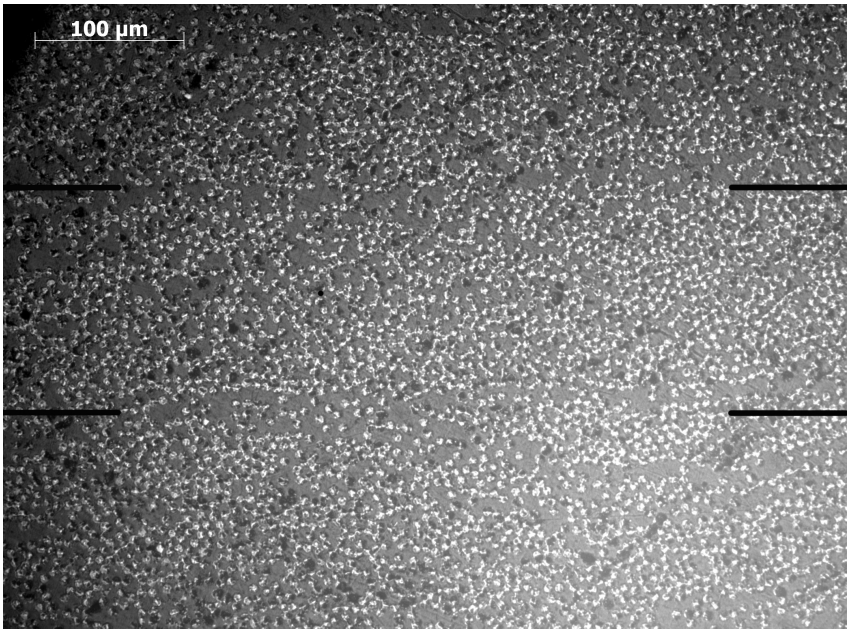


Figure 4.7: Microscopy images cross-section $[0]_{4S}$, zoomed 20x

One can see the distribution of fibre (white) opposed to matrix (grey). All black areas represent damaged areas on the cross-section surface. The solid black lines have been added in order to visualise the original position of plies, based on the original ply thickness. These lines indicate where the ply interface is expected to be. From a first glance, it seems that the $[0]_{4S}$ laminate has a more or less homogenised distribution of fibres and matrix. Fibres are in contact and an electrical current path exists in both transverse (left to right) and through-the-thickness (top to bottom) direction. Looking closely however at Figure 4.7, one can see matrix rich areas to be present near the original ply interface. Fibre migration over the interface has taken place, enabling fibre contact in thickness direction but a resin rich area still resides on that diffused interface. The resin rich area is stretched in the transverse direction, affecting the through-the-thickness conduction primarily. It is expected that this causes the through-the-thickness conductivity of the $[0]_{4S}$ laminate to be smaller than its transverse conductivity. The images confirm fibre-fibre contact to exists in both transverse and through-the-thickness direction.

The cross-section of the $[0,90]_{2S}$ laminate has also been investigated. The samples were cut under an angle of 45 [deg], in order to visualise the cross-sections of the fibres of the individual layers. Figure 4.8 shows the cross-section of the $[0,90]_{2S}$ laminate.

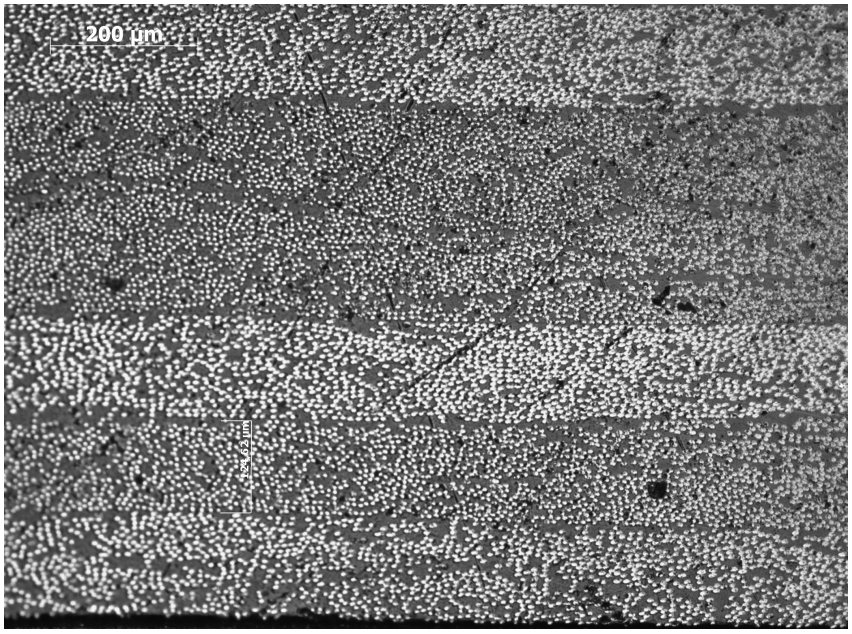


Figure 4.8: Microscopy images cross-section $[0,90]_{2S}$, zoomed in 10x

Figure 4.8 clearly shows the different laminate plies. In between the fibre plies, one can still see an interface present caused by resin rich areas. Although there is fibre-fibre contact between the individual plies, resin rich areas limit the amount of paths an electrical current can follow in through-thickness direction. The effect is more pronounced than what was witnessed in Figure 4.7. This explains the reduced through-the-thickness conductivity for the $[0,90]_{2S}$ laminate compared to the $[0]_{4S}$ laminate. When the fibre plies are oriented over a relative fibre angle of 90 [deg] with each other, fibres cannot migrate over the interface, resulting in a more concentrated resin rich area compared to the $[0]_{4S}$ laminate interfaces. The same resin rich areas are also present in between the plies for the $[45,-45,0,90]_S$ laminate. The interface is equivalent to what is shown in Figure 4.8.

The microscopy images clearly show different regions in the micro-structure of the laminate lay-ups. It is not an even distribution of fibre and matrix; matrix rich areas are present around the interfaces between plies. The resin rich areas in between fibre plies will cause an increase in resistance encountered when currents flow through-the-thickness. Based on the micro-structure, the distinction between volume and interface resistance can be made. Figure 4.9 shows what this means for the through-the-thickness resistance measurements. Note that no capacitive elements are included in Figure 4.9. Whether this assumption is valid, will be examined in Section 4.5. When dealing with a direct current, capacitors behave like open circuits.

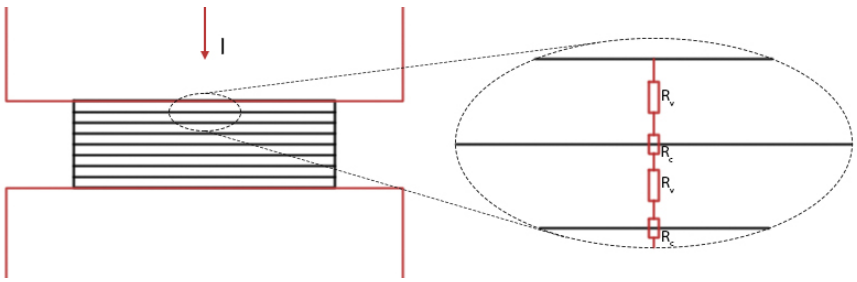


Figure 4.9: Distinction volume and interface resistances

Figure 4.9 shows a through-the-thickness sample clamped between the copper terminals. A current goes through the sample and encounters different resistances. The total resistances have been measured in Section 4.1.2. These total resistances showed a dependency on the laminate lay-up. Together with the fact that matrix rich areas are located at the interfaces between fibre plies, the current research states that the total through-the-thickness resistance is comprised of separate volume and interface resistances. The volume resistance in this case is described as the resistance the current encounters when going through the volume of the ply. This

will be a material property. The interface or contact resistance, is the resistance the current encounters when crossing the interface between plies. This resistance will be dependent on the relative fibre angle between plies. The results from Section 4.1.2 can be used to find these relative volume and contact resistances.

## 4.3. THROUGH-THE-THICKNESS VOLUME AND CONTACT RESISTIVITIES

In order to find the relative values for the volume and contact resistances for the through-the-thickness electric properties of the UD CF-PEKK material, the results of Section 4.1.2 can be used. Based on through-the-thickness resistance measurements and microscopy images, it was assumed that the total through-the-thickness resistances consists of separate volume and contact resistances. The makes the total through-the-thickness resistance of an 8-ply laminate consists of 8 volume resistances and 7 interface resistances. Equation 4.3 shows the relation of resistors in series and Ohm's law to find the relevant material properties for the $[0]_{4S}$ through-thickness resistance samples.

$$\left.\begin{aligned} R_{[0]4S} &= 8R_{volume} + 7R_{\text{inter}face} \\ R_{volume} &= \rho_v \frac{t_{ply}}{A_{ply}} \\ R_{\text{inter}face} &= \rho_{c\gamma} \frac{1}{A_{ply}} \end{aligned}\right\} R_{[0]4S} = 8\rho_v \frac{t_{ply}}{A_{ply}} + 7\rho_{c0} \frac{1}{A_{ply}} \tag{4.3}$$

In this equation $t_{ply}$ and $A_{ply}$ represent the fibre ply thickness and cross-sectional area of the sample. The volume resistivity $\rho_v$ is used to find the volume resistance and is expected to be a material property. The parameter $\rho_{c\gamma}$ stands for the contact resistivity dependent on the relative fibre angle $\gamma$ between plies. With the $[0]_{4S}$ lay-up, all fibre plies are oriented over a relative fibre angle of 0 [deg] with respect to each other. Adding the through-thickness resistance measurements of the other laminate lay-ups, results in the linear system of equations given in Equation 4.4.

$$\begin{bmatrix} 8\frac{t_{[0]4S}}{A_{[0]4S}} & \frac{7}{A_{[0]4S}} & 0 & 0 \\ 8\frac{t_{[0,90]2S}}{A_{[0,90]2S}} & \frac{1}{A_{[0,90]2S}} & 0 & \frac{6}{A_{[0,90]2S}} \\ 8\frac{t_{[45,-45,0,90]S}}{A_{[45,-45,0,90]S}} & \frac{1}{A_{[45,-45,0,90]S}} & \frac{2}{A_{[45,-45,0,90]S}} & \frac{4}{A_{[45,-45,0,90]S}} \\ 16\frac{t_{[45,-45,0,90]2S}}{A_{[45,-45,0,90]2S}} & \frac{1}{A_{[45,-45,0,90]2S}} & \frac{6}{A_{[45,-45,0,90]2S}} & \frac{8}{A_{[45,-45,0,90]2S}} \end{bmatrix} \begin{bmatrix} \rho_{vol} \\ \rho_{c0} \\ \rho_{c45} \\ \rho_{c90} \end{bmatrix} = \begin{bmatrix} R_{[0]_{4S}} \\ R_{[0,90]_{2S}} \\ R_{[45,-45,0,90]_S} \\ R_{[45,-45,0,90]_{2S}} \end{bmatrix} \tag{4.4}$$

It depends on the geometry of the samples and the average resistances measured in the through-thickness direction for the different lay-ups, which have been measured and are included in Appendix G. The volume and contact resistivities can be found by solving the system of equations. This is possible since the number of unknowns equals the number of equations. The average through-the-thickness resistances measured are given in Table 4.2a. The output to solving the system of equations is given in Table 4.2b.

Table 4.2: Input and output values volume and contact resistivity

(a) Average input resistances through thickness

| Laminate lay-up | Resistance [Ω] |
|---|---|
| $[0]_{4S}$ | 30.8±3.8 |
| $[0,90]_{2S}$ | 45.7±8.5 |
| $[45,-45,0,90]_S$ | 52.6±11.5 |
| $[45,-45,0,90]_{2S}$ | 115.8±27.3 |

(b) Volume and contact resistivities and conductivities

| Parameter | Resistivity | Conductivity |
|---|---|---|
| $\rho_{vol}$ | 0.69 $[\Omega \cdot m]$ | 1.45 $[Sm^{-1}]$ |
| $\rho_{c0}$ | $0.50{\cdot}10^{-04}$ $[\Omega \cdot m^2]$ | $2.0{\cdot}10^{04}$ $[Sm^{-2}]$ |
| $\rho_{c45}$ | $2.7{\cdot}10^{-04}$ $[\Omega \cdot m^2]$ | $3.7{\cdot}10^{03}$ $[Sm^{-2}]$ |
| $\rho_{c90}$ | $1.2{\cdot}10^{-04}$ $[\Omega \cdot m^2]$ | $8.3{\cdot}10^{03}$ $[Sm^{-2}]$ |

The results are given both in their relative resistivity as conductivity. The conductivity is simply the inverse of the resistivity. An average volume conductivity of 1.45 $[Sm^{-1}]$ was found. This is a material property and will be taken as a constant for the different laminate lay-ups. The contact resistivities dictate the total through-thickness resistance. Table 4.2b shows that the contact resistivity $\rho_{c0}$ has the smallest value and $\rho_{c45}$ the largest. This can also be seen from the through-thickness resistance measurements of Table 4.2a. The smallest through-thickness resistance was measured for the $[0]_{4S}$ laminate lay-up and the largest for the [45,-45,0,90]$_S$ laminate lay-up. One must however stress the fact that this is based purely on the average values of the through-thickness resistance measurements. Viewing the different standard deviations, one can see from Table 4.2a that the difference between the $[0,90]_{2S}$ and [45,-45,0,90]$_S$ laminates is non-significant. The relative high standard deviations are presumed to be caused by the micro-structure of the laminates. Through-thickness resistance depends on the amount of fibre-fibre contacts between the individual plies. Areas at

which there are lots of contacts will yield lower resistance samples and vice versa. One method to overcome this problem is to make the dimensions of the samples bigger. With larger samples, the area over which the material properties are measured is also larger. This would average out the effects of the micro-structure on the electric material properties. However, due to misalignment of the copper terminals with the samples, the contact between samples and copper terminals is non-perfect. The larger the sample's dimensions, the worse the contact between sample and copper terminals. The only method of finding the actual material properties is to measure as many samples as possible. The standard deviation will not go down but the estimate of the average will be closer to the actual value. This research uses a minimum of 10 samples to determine the material properties in through-thickness direction.

With all of the electric conductivity properties for the different laminate lay-ups known, one has all the information needed to model the laminates electrically for the computational induction heating model. However, there is no guarantee that these values are accurate. Before putting the electric properties to use, the different electric properties found for the material should be validated.

## 4.4. VALIDATION ELECTRIC MATERIAL PROPERTIES

All of the electric properties of the UD CF-PEKK material have been measured and an innovative procedure was used to distinguish between electric through-thickness material properties and electric interface resistance present between plies. In order to check whether the material properties found, can accurately be used to model the material during induction heating, validation of these material properties should be performed. One of the methods of validating the material properties is by measuring the resistance of a sample with laminate lay-up $[45,\text{-}45]_{2S}$ in longitudinal direction. By measuring the resistance and predicting the resistance based on the material properties found, one can find out whether these material properties are constant no matter how the current travels through the material. The total resistance measured for the $[45,\text{-}45]_{2S}$ samples will be based on almost all of the material properties found in previous sections. By having the length of the samples bigger than their width, the currents will have to jump through the thickness in order to go from one copper terminal to the other. Due to the much smaller conductivity in through-thickness direction compared to the fibre direction, the currents are expected to jump only once through-the-thickness. The total resistance measured for the $[45,\text{-}45]_{2S}$ samples with aspect ratios larger than 1, will depend on the electric conductivity in fibre direction, the transverse conductivity as well as the through-thickness conductivity and the contact resistivity between plies. Validation will take place by predicting the resistance of the $[45,\text{-}45]_{2S}$ samples in longitudinal direction with the help of a computational model. By comparing these predicted values with the actual resistances measured experimentally, one can see whether the material properties are accurate and consistent. The length of the $[45,\text{-}45]_{2S}$ samples will be 10% bigger than their width, to force the current to jump through-the-thickness. The dimensions of the samples are included in Appendix G.

The experimental results of Section 4.1 showed how the contact between sample and copper terminal affects the resistances measured. This will also influence the resistance measured for the $[45,\text{-}45]_{2S}$ samples. In order to take this into account, the DC heating set-up of Section 2.5 will also be used to visualise the contact between $[45,\text{-}45]_{2S}$ sample and copper terminal. Figure 4.10 shows the heating images for two of the samples tested.

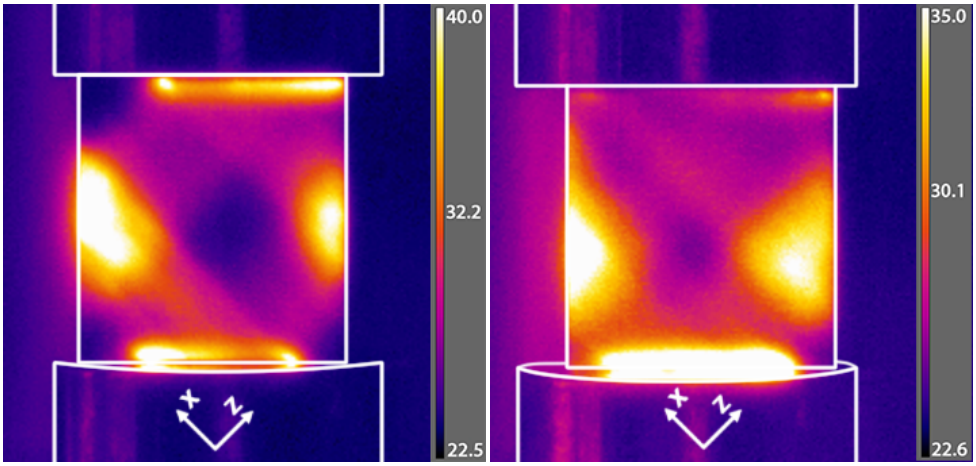


(a) DC Heating image $[45,-45]_{2S}$ sample 1 in longitudinal direction

(b) DC Heating image $[45,-45]_{2S}$ sample 3 in longitudinal direction

Figure 4.10: DC-heating images $[45,-45]_{2S}$ samples

Figure 4.10 shows the outlining of the copper terminals and the sample indicated by the white lines. The fibres are oriented along the x- and z-axes. The thermal images show heat to be generated in the direction of the fibres and at the area at which the currents jump through the thickness. The thermal images show how most of the heat is being generated at the locations where the current is forced to change direction. This is as expected. Due to the laminate lay-up of the sample, the current has to jump from fibre ply to adjacent fibre ply in order to cross the sample. Due to the much smaller conductivity in thickness direction, computed in Section 4.3, the current is expected to jump only once through the thickness. The results shown in Figure 4.10 are used as a visual tool to show how currents cross the $[45,-45]_{2S}$ samples. Next to that, the figures are used to visualise the contact between sample and copper terminals. The width over which the current enters the sample as well as the width over which the current exits the sample, will have an influence on the total resistance measured. This will be taken into account when modelling these resistance experiments. A total of ten samples were cut to size and tested on electric resistance. The dimensions of the samples as well as the test results are included in Appendix G. Five of these samples were further analysed with the help of Photoshop (finding the contact width between copper terminal and sample) and modelled with the help of a computational model.

The resistance experiments were modelled with the help of a computational model. With the help of Comsol Multiphysics, the resistance of the $[45,-45]_{2S}$ samples is predicted by solving an Electric Currents physics model. The sample has been modelled and the contact area between sample and copper terminals has been taken into account. A detailed description of the computational model is included in Appendix H. Table 4.3 shows both the experimental resistance results as well as the Comsol predicted results.

Table 4.3: Comsol model resistance predictions $[45,-45]_{2S}$ samples

| Sample | Resistance measured [Ω] | Resistance prediction Comsol [Ω] | Difference [%] |
|---|---|---|---|
| 1 | 0.54 | 0.539 | -0.19 |
| 3 | 0.43 | 0.432 | 0.47 |
| 4 | 0.43 | 0.425 | -1.2 |
| Ori1 | 0.52 | 0.530 | 1.9 |
| Ori2 | 0.42 | 0.434 | 3.3 |

The table shows a maximum difference of 3.3% found between experimental results and Comsol predictions for the longitudinal resistances of the $[45,-45]_{2S}$ samples with an aspect ratio of approximately 1. Table 4.3 shows how Comsol is able to predict the resistances found experimentally. With the Comsol model based on the material input taken from previous sections, the material properties are deemed validated.

## 4.5. ALTERNATING-CURRENT RESPONSE

One of the three heating mechanisms that could be present in the heating of the UD CF-PEKK laminates is heating due to dielectric heating. Dielectric heating is based on the accumulation of charge within the UD CF-PEKK material, locally creating strong electric fields. These electric fields rotate the dipoles that are present within the dielectric matrix. This accumulation of charge can be visualised by monitoring the voltage present over the sample and comparing this with the output voltage. Without accumulation of charge, no interply electric fields are created. All of the material properties have been measured using a direct current. Accumulation of charge is a time-dependent process and should become apparent when using alternating currents. When charge accumelates, it will be at the interface between plies [55, 57, 58, 92]. For this reason, the $[0,90]_{2S}$ laminate has been tested with the help of alternating currents. A total of five through-thickness resistance samples were cut from the $[0,90]_{2S}$ laminate. The dimensions of the samples were taken slightly bigger than the DC-resistance samples used for finding the through thickness resistance of the $[0,90]_{2S}$ laminate. This was done in order to limit any fringing and stray capacitance effects. The copper terminal used to input the alternating current , is made from copper and is circular in shape. With the diameter equal to approximately 10 [mm], the sample dimensions have been kept approximately equal to 11x11 [mm]. The dimensions of the different samples are included in Appendix G. The measurement set-up of Section 2.4 was used to subject the sample to the alternating current. Figure 4.11 shows the circuit used to visualise any time-dependent behaviour.

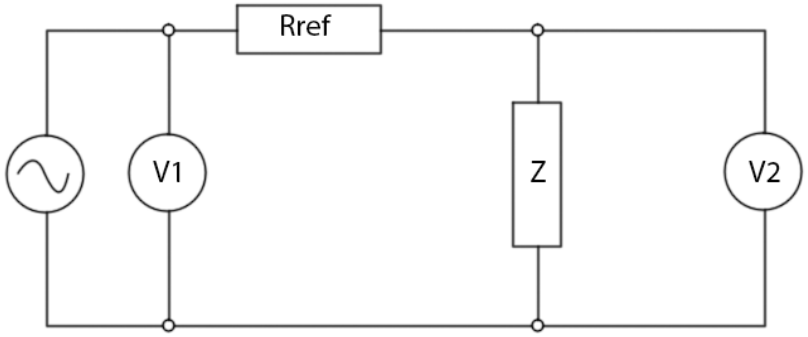


Figure 4.11: Circuit for finding capacitive behaviour through-the-thickness $[0,90]_{2S}$ samples CF-PEKK material

The alternating current source used is a Wavetek model 188, able of producing sinusoidal waves ranging from 1 [Hz] to 5 [MHz]. A reference resistance $R_{ref}$ is needed in order to visualise any time-dependent behaviour. If this resistance is not included, and the sample $Z$ behaves as a capacitor, the sample would immediately charge. The larger the reference resistance, the longer the possible capacitor $Z$ takes to charge. Taking larger reference resistances helps with visualising the time-dependent effect. However, one also has to take into account that the circuit of Figure 4.11 acts as a voltage divider. Taking very large reference resistances reduces the voltage present over the sample. Reference resistances ranging from 10 [$\Omega$] to 10 [$k\Omega$] have been used. The output voltage $V1$ and voltage over the sample $V2$ are measured with the help of an oscilloscope and compared to each other. When any accumulation of charge occurs within the sample, this will become apparent by a phase shift between the output voltage signal $V1$ and the voltage present over the sample $V2$. When the sample behaves as a resistor, this phase difference will be zero; no accumulation of charge occurs.

A total of five samples were analysed. The result for samples 1 and 2 are shown in Figure 4.12.

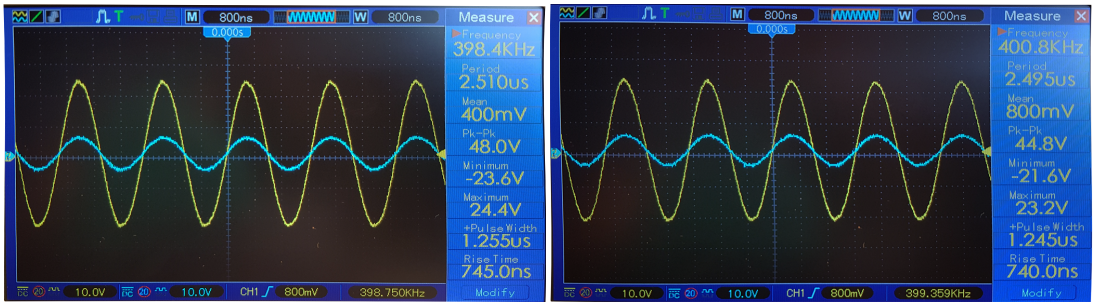


(a) Sample 1 at a frequency of 400 [kHz]

(b) Sample 2 at a frequency of 400 [kHz]

Figure 4.12: Oscillating voltage output for $[0,90]_{2S}$ samples

Figures 4.12a and 4.12b show the relation between output voltage $V1$ (yellow line) and the voltage over the sample $V2$ (blue line). The frequency of the current source is approximately 400 [kHz]. This is similar to the frequency of the current going through the copper coil during induction heating. The results from Figure 4.12 have been performed using a 100 [Ω] reference resistance. Increasing the magnitude of the reference resistance only reduced the voltage over the sample, it did not influence the phase between source and sample voltage. The frequency was varied between 1 [Hz] and 1 [MHz]. No phase differences were recorded for any of the samples. The results indicate that when applying alternating currents to the material, the material still behaves as a resistor. No capacitive effects were recorded for any of the samples.

It is expected that dielectric heating will not play a role in the induction heating of the UD CF-PEKK laminates. This assumption is based on the findings of three separate experiments. The conductivity measurement results showed a non-zero electric conductivity in both the transverse and through-the-thickness directions for the UD CF-PEKK material. This indicates electric current paths to exist in these directions. This was confirmed by microscopy images, showing fibre-fibre connections to exist in both transverse and through-the-thickness directions for the material. When electric current paths are available, accumulation of charge is not expected to take place. The zero phase shift angle measured with the oscilloscope for the through-thickness samples of the $[0,90]_{2S}$ laminate also showed how the material behaves purely as a resistor. The induction heating problem will be modelled with the help of Comsol Multiphysics. Comsol is able to take the permittivity properties of the matrix into account. The permittivity properties will be included but based on these findings, it is expected that its influence on the heating results is negligible.

## 4.6. Conclusion

The electric material properties of the UD CF-PEKK material have been found in the current chapter. A distinction has been made between the electric material properties and electric contact resistance properties that are believed to be present between fibre plies. Table 4.4 shows the electric material properties of the UD CF-PEKK material at room temperature, for the different laminate lay-ups tested.

Table 4.4: Final results electric resistance measurements CF-PEKK material

| | Conductivity RT |
|---|---|
| Longitudinal $[0]_{4S}$ | 18.2±3.3 [kS/m] |
| Transverse $[0]_{4S}$ | 12.6±0.7 [S/m] |
| through-the-thickness $[0]_{4S}$ | 1.0±0.1 [S/m] |
| through-the-thickness $[0,90]_{2S}$ | 0.7±0.1 [S/m] |
| through-the-thickness $[45,-45,0,90]_{S}$ | 0.6±0.1 [S/m] |
| through-the-thickness $[45,-45,0,90]_{2S}$ | 0.6±0.1 [S/m] |

RT = Room Temperature

Table 4.4 indicates that the electric conductivity in fibre direction is maximised. Even though the electric conductivities in transverse and through-thickness directions are much smaller, they are non-zero. This indicates that electric current paths exists in every direction of the UD CF-PEKK laminates. Table 4.4 shows the relatively large standard deviation for the measurements performed in fibre direction. Due to the very small resistances

measured in fibre direction, the measurement became very sensitive to the electric contact existing between sample and copper terminals of the measurement set-up. Effective current widths were used to compute the electric conductivity in fibre-direction. These were obtained by using DC-heating experiments. Temperature-dependent measurements showed a significant dependency of the electric conductivity on the temperature to be present only in fibre-direction. Electric conductivity in transverse and through-thickness directions were found to be approximately constant with respect to temperature.

Table 4.4 shows how the laminate lay-up influences the through-thickness conductivity measurements made. Apparently, the relative fibre angles between plies influence the resistances the laminate offers to electric currents. Together with analysing the micro-structure of the material and the Alternating-Current (AC)-measurements, a distinction was made between the resistance the current encounters when going through the volume of the plies and the resistance encountered when crossing the interface between plies. With this assumption, a constant through-thickness electric resistivity $\rho_{vol}$ could be found as a material property for the UD CF-PEKK material. And a contact resistivity $\rho_{c\gamma}$, dependent on the relative fibre angle $\gamma$ between plies, can be used as an additional electric constraint in order to model the material within the computational model. Based on the through-the-thickness resistance measurements, the through-thickness volume resistivity as well as the relative fibre angle resistivities of the UD CF-PEKK material could be deduced. These are repeated in Table 4.5, with the conductivity equal to the inverse of the resistivity.

Table 4.5: Through-thickness volume and contact resistivities of UD CF-PEKK

| Parameter | Resistivity | Conductivity |
|---|---|---|
| $\rho_{vol}$ | 0.69 $[\Omega \cdot m]$ | 1.45 $[Sm^{-1}]$ |
| $\rho_{c0}$ | $0.50 \cdot 10^{-04}$ $[\Omega \cdot m^2]$ | $2.0 \cdot 10^{04}$ $[Sm^{-2}]$ |
| $\rho_{c45}$ | $2.7 \cdot 10^{-04}$ $[\Omega \cdot m^2]$ | $3.7 \cdot 10^{03}$ $[Sm^{-2}]$ |
| $\rho_{c90}$ | $1.2 \cdot 10^{-04}$ $[\Omega \cdot m^2]$ | $8.3 \cdot 10^{03}$ $[Sm^{-2}]$ |

The through-thickness volume resistivity will be used as a constant material input the computational model. The contact resistivities will be added as constraints between plies.

Together with the results from Chapter 3, this chapter tried to find an answer to the first main sub-research question: *'Which heating principle is dominant in the heating of UD lay-up CF-PEKK laminates?'*. Based on the conclusions from Chapters 3 and 4, this research states that Joule junction heating is the dominant heating principle in the heating of the UD CF-PEKK laminates.

Heating of the UD CF-PEKK laminates depends on Joule heating both in fibre direction and at fibre-fibre contacts. Based on thermal images, one could witness most of the heat being generated at the locations where currents could no longer follow the direction of the fibre, but had to cross either in transverse direction or in through-the-thickness direction. Conductivity measurements were performed and showed the much larger resistance the current encounters when going in these directions, explaining the fact that most of the heat was being generated at these locations. The fibre orientation within the UD laminate lay-up thus dictates the locations where heat is being generated. At the same time, the locations of maximum heating are also closely related to the coil geometry. The coil creates the magnetic field vector causing the generation of eddy currents. The eddy currents will try to oppose the excitation magnetic field vector. The fibre orientations however dictate the direction in which the current will actually travel. The non-zero conductivity measurements showed the possible current paths apparent within the material in transverse and through-the-thickness direction. This was confirmed by microscopy images, showing fibre-fibre contacts. Results obtained with the oscilloscope showed that the material did not exhibit any time-dependent behaviour to the alternating excitation current. This adds to the reasoning that actually, Joule heating is the only form of heating apparent in the UD CF-PEKK lay-ups, with junction joule heating being dominant.

# 5
# COMPUTATIONAL MODEL

The results from Chapters 3 and 4 will be used in order to attempt to model the physics behind the induction heating process. This chapter will try to find an answer to the question whether it is possible to model the inductive behaviour of the Uni-Directional (UD) Carbon Fibre (CF)-Poly(Ether-Ketone-Ketone) (PEKK) laminates. An attempt was made to model the induction heating physics with the help of Ansys. After simulating the induction heating of the $[0]_{4S}$ and $[0,90]_{2S}$ laminates, it was found that Ansys is not able to correctly predict the heating patterns and temperatures recorded during experiments. Due to this, it was decided to continue modelling with the help of Comsol Multiphysics. The limitations of Ansys are discussed in Appendix K.

## 5.1. COMSOL MODEL SET-UP

The flow chart on which the computational model is based, is shown in Figure 5.1.

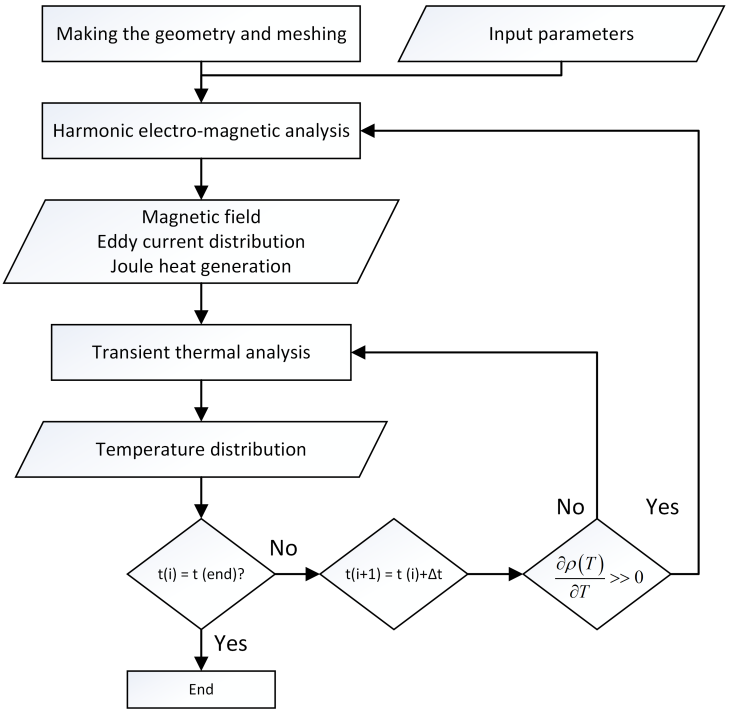


Figure 5.1: Flow chart computational model

The program starts by defining the input parameters and modelling the geometry. It imports the material properties, applies the boundary conditions and loads and meshes the geometry. After that, the harmonic Three-Dimensional (3D) Electromagnetic (EM)-module starts. The output of the EM-module is the eddy current distribution and the equivalent Joule heat generation. The Joule heat generation will be transferred from the EM-module to the Thermal (TH)-module as a body load. The boundary conditions and loads will be adjusted in order to be able to solve the thermal analysis. After the thermal analysis, the temperature increase throughout the laminate is known and based on the time increment and the temperature dependent material properties, the model re-iterates.

### 5.1.1. GEOMETRY

The Helmholtz and Hairpin coils have both been modelled by using a 3D Bézier polygon. With the Bézier polygon, one can accurately draw the shape of the coil using a combination of linear, quadratic and cubic line segments. The centreline of the coil object is drawn and one can sweep the cross-section of the coil along the Bézier polygon in order to create the 3D solid object. Figure 5.2 shows the Helmholtz coil object with respect to the laminate.

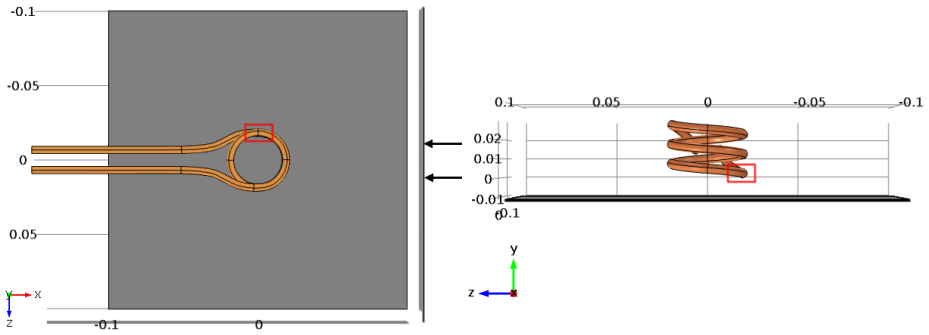


(a) Top view (b) Side view

Figure 5.2: Helmholtz coil solid geometry

Figure 5.2b shows how the Helmholtz coil geometry is not equally distanced from the laminate at the different sections of the coil. The coupling distance was taken as the minimum distance between coil and laminate. The red square added indicates the location where this distance is minimised. This varying coupling distance will influence heating results, for the varying magnetic field flux being stronger at these areas beneath the coil. Due to limitations in available computational power, it was decided to not model the coil object as a 3D solid. The reason for this was based on the quality of the mesh of the solid coil object. With the solid coil objects, the mesh was of a low quality and the coil would need a large amount of elements for the result to converge. Keeping in mind that the model is to be used to optimise the process parameters discussed in Chapter 1, the model should not require a lot of computational power and should be able to analyse the multi-physics problem in a relatively short amount of time. With the solid coil object, Comsol took several days to find a solution for a single problem, compared to just approximately an hour with the line object. That is why it was decided to model the coil as a line object, to enable one to do multiple analyses in a short amount of time. There are also disadvantages encountered when modelling the coil as a line object. One is unable to include the cooling water running through the coil during induction heating. Heating experiments from Chapters 3 and 4 showed that the cooling water keeps the coil at a constant temperature of approximately 20 $[^oC]$. However, this could be taken into account by setting the ambient temperature to a constant 20 $[^oC]$. Using a hollow coil object and modelling the flow of water would have considerably increased the complexity of the model and not necessarily improved temperature results in the laminate. One different aspect that is now neglected is the fact that alternating currents always reside on the outer surfaces of the conductors through which the electric field is present. This skin effect is also neglected when using the line object for the coil geometry. Whether this has a large effect on the final result of the model has not been addressed by the current research, and is included in the recommendations.

The laminates were modelled using block objects. Each ply was modelled separately by adding layers to the laminate object. By modelling each individual ply, one can take into account the eddy current paths throughout the laminate. When the laminate would have been modelled using only a single solid object, the through thickness electric properties of the material could not have been properly taken into account. This prohibits one to model the heating behaviour witnessed in Chapter 3 accurately.

In order to model the changing magnetic fields, the air also has to be modelled. The air was modelled using a block object. The dimensions of the air domain were taken 50% larger than the dimensions of the laminate, in order to reduce any edge effects on the magnetic field. In order to optimise the meshing of the air domain, several partitions will be used. The solid ply objects obtain a relatively large aspect ratio. The thickness is much smaller than their relative width and length. Meshing could become problematic with such small edges with

respect to the overall size of the total model. In order to overcome this problem, the air domain is partitioned at the locations where it is adjacent to these small ply dimensions. Figure 5.3 shows these locations.

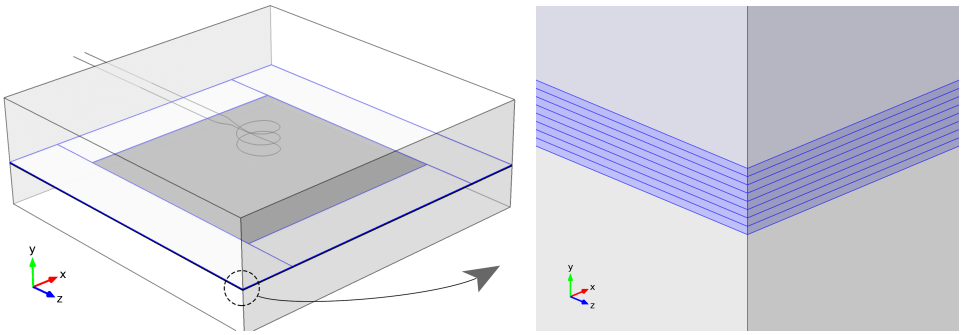

(a) Partitions air domain (b) Zoomed in through thickness

Figure 5.3: Air domain Comsol model partitioned

The blue lines indicate where the air domain has been partitioned. The dark solid in the middle represents the laminate domain. The air domain is everywhere around the laminate and coil domains. The sole purpose to partitioning the air domain at these locations is to have a smooth transitioning mesh from the laminate domain to the air domain. Small edges are prevented, possibly causing irregularities in the global air domain mesh. These partitioned air domains will be meshed using the same meshing strategy as was used for the ply domains. This way, the mesh perfectly transitions between the laminate and the air. Small edges are prevented and the needed amount of elements reduced. The complete Comsol model containing all of the different objects is shown in Figure 5.4.

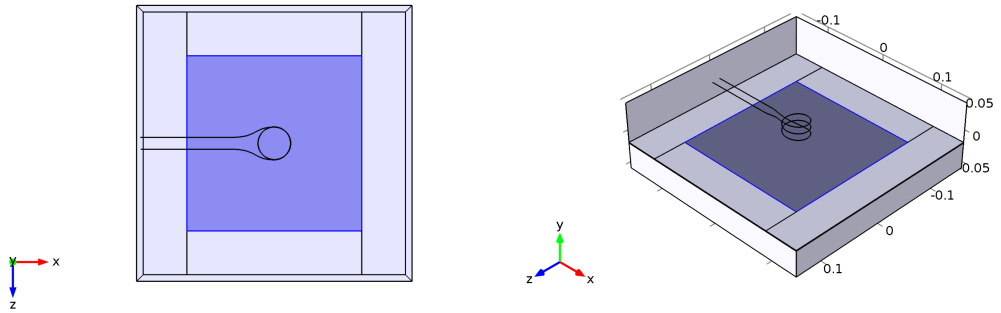


(a) Geometry Comsol model top view (b) Geometry Comsol model isometric view

Figure 5.4: Geometry computational model

Figure 5.4 shows the different objects, with the centre of the coordinate system located in the middle of the coil, with the bottom of the coil at y=0 (Figure 5.2). All of the grey objects represent the air domains, the blue objects are the individual plies and the line object represents the coil. The different orientations $\alpha$ investigated in Chapters 3 and 4 are included in the Comsol model by rotating the coil accordingly.

### 5.1.2. MESHING

The individual plies have been meshed using hexahedral elements. Different meshing strategies were applied to the different laminates, as shown in Figure 5.5.

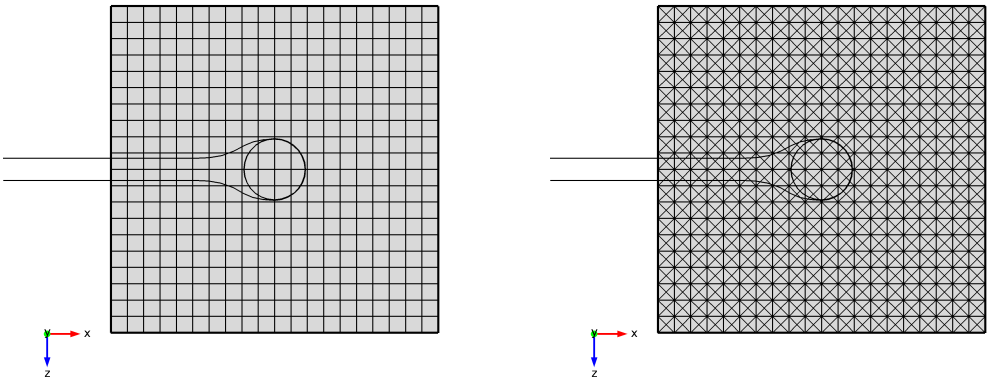

(a) Used for laminates $[0]_{4S}$ and $[0,90]_{2S}$ (b) Used for laminate $[45,-45,0,90]_S$

Figure 5.5: Meshing of the laminate domain

The mapped quadrilateral elements of Figure 5.5a are swept in thickness direction to produce the hexahedral elements. The elements of Figure5.5b are produced by inserting an additional node at the centre of the mapped elements of Figure 5.5a. These are again swept through the thickness of the laminate to create the triangular prism elements. With this meshing strategy, the elements are oriented in the same directions as the primary material properties of the individual plies. The added nodes in the centre of the mapped elements of Figure 5.5b are needed to have the elements also aligned with the material properties of the 45- and -45 [deg] layers within the laminate lay-up. Due to the maximisation of the electric properties of the material in these distinct directions (fibre directions), the eddy current density will also be maximised in these directions. The mesh aligns with the physics of interest. The amount of elements needed in thickness direction depends on the skin depth of the material. Chapter 1 showed how the skin depth is influenced by the magnetic permeability and electric conductivity of the material and the frequency at which the magnetic flux fluctuates. The skin depth shows how the currents primarily flow near outer surfaces of conducting materials. In order to take this into account, enough elements are needed in thickness direction to be able to model this behaviour. The Comsol manual advices to have a maximum element size of halve of the skin depth in thickness direction [93]. Using Equation 1.15, the minimum skin depth is calculated to be approximately equal to 6 [mm]. With the laminate thickness equal to approximately 1 [mm], 8 element divisions in thickness direction will be enough to incorporate the skin depth effect.

The partitioned air domain sections were meshed using mapped quadrilateral elements, sweeping these mapped surfaces through their thicknesses. The mesh perfectly connects to the mesh of the laminate. The rest of the air domain is meshed using tetrahedral elements. The tetrahedral elements were necessary in order to mesh the volume around the coil object. In order to have a smooth transition between the elements of the laminate and the air domain, the surface elements of Figure 5.5a were converted to triangular elements. This was only done to enable the transition between hexahedral to tetrahedral elements. This was not necessary for the elements seen in Figure 5.5b.

### 5.1.3. MATERIAL DEFINITION

From Chapters 2 and 4, the temperature dependent material properties were imported into Comsol. The UD material properties are assigned to each ply individually. In order to incorporate the fibre direction of each ply, the material properties are rotated accordingly. This was done by rotating the local coordinate system over the relative fibre angle. This local coordinate system is then used within the physics module, in which the material properties are loaded. This enables one to include all of the different fibre angles needed. The material properties for the CF-PEKK plies were taken as a constant. In order to incorporate the through-the-thickness electric behaviour, varying surface resistivities were applied between the fibre plies. This makes for a generalisable approach into modelling laminates of different lay-ups.

The material properties for air and copper were already included in a material library within Comsol. The electric conductivity of the air was adjusted and set to a value 1000 times smaller than the smallest conductivity of the laminate in any direction. This was done to prevent currents leaking to the air domain.

### 5.1.4. CONSTRAINTS

Several different loads and boundary conditions were applied to the model. These can be divided into the magnetic field constraints and the heat transfer constraints. For the Magnetic and Electric Fields study, an initial magnetic vector potential and an electric potential of zero were applied to all domains. The outer boundaries of the air domains were magnetically insulated and an edge current was applied as a load to the coil line object. A surface resistivity was applied to the interface boundaries between plies by setting a contact impedance constraint. A varying surface resistivity and a surface capacitance of 0 $[F/m^2]$ were applied, based on the findings of Chapter 4.

For the Heat Transfer study, heat transfer in solids was used to model the conduction of heat through the laminate only. Heat conduction through the air and coil objects was neglected to reduce the computational power required to solve the model and be able to apply heat convection and radiation on the laminate's outer surfaces. A convective heat flux boundary condition and a diffuse surface boundary condition were applied on the outer surfaces of the laminate domain. These simulate the convection and radiation of heat from the laminate. The beginning temperature measured by the thermocouples for the separate heating experiments were used as starting temperature for the model.

A multi-physics study is added in order to couple the magnetic and electric fields and heat transfer studies. The electromagnetic heat source constraint is applied, which transfers the generation of heat from the magnetic fields study to the heat transfer study. A boundary electromagnetic heat source constraint is applied that maps the electromagnetic surface losses as a heat source in the heat transfer study. The heat transfer study computes the conduction of heat and the increase in temperature of the laminate. This temperature increase is coupled back to the magnetic fields study by a temperature coupling constraint.

### 5.1.5. MESH CONVERGENCE STUDY

The finer one meshes the model, the more accurate the results will become. However, the finer mesh will also require additional computational effort. In order to analyse the accuracy of the model, a mesh convergence study is included for the three laminates analysed in Chapters 3 and 4. The mesh convergence studies were performed with the Helmholtz coil. The mesh size was reduced by locally refining the mesh of the laminate domain. Thermocouples have been used to measure the temperature increase in Chapter 3. All of the thermocouple locations have been included in Appendix I. It was decided to take the temperature at the location of thermocouple number three to analyse the mesh convergence of the three models. This specific thermocouple was chosen because of its positioning at locations of maximum heating. Figure 5.6 shows the influence of the amount of elements used to mesh the laminate domain on this maximum temperature prediction.

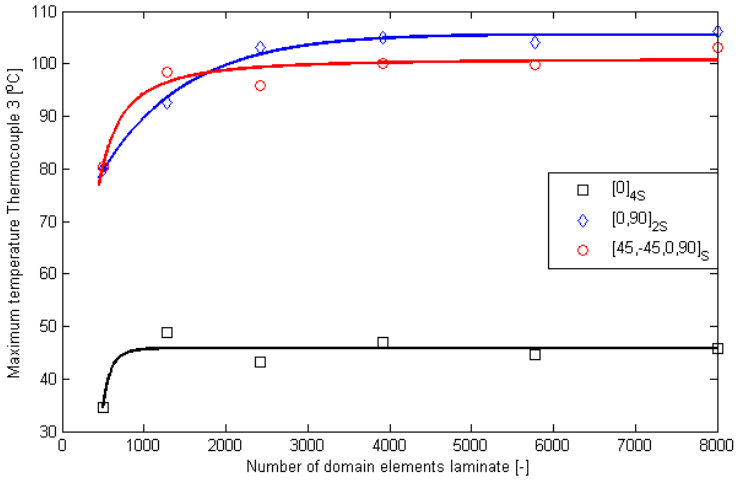


Figure 5.6: Mesh convergence study for Helmholtz coil

Figure 5.6 shows that with an increasing number of elements in the laminate domain, the maximum temperature for the three different laminae converges. The mesh convergence study was only applied on the models with the Helmholtz coil under an orientation of $\alpha = 0[deg]$. It is assumed that for different coils and orientations, the models will still converge.

### 5.1.6. DETAILS OF ANALYSIS

In order to find a solution to the multi-physics problem, one could either use a direct or an iterative solver. The difference between the direct and iterative solvers is that the iterative solvers gradually come to a solution instead of finding the solution in one big computational step. With the iterative solvers, one can visually see the error estimate as a function of the number of iterations. Iterative solvers require much less memory, making the model solve in a considerably less amount of time. This is the main reason for choosing an iterative solver. Next to that, one can visually see whether the model converges to a solution based on the error residual plotted during solving. Using a different solver type will not change the outcome but only influences the relative speed of finding a solution [94]. The reason for modelling the coil as a line object also has to do with these solver options. When the coil was modelled as a 3D solid instead of a line object, inversion of mesh elements occurred due to the quadratic and cubic shapes present in the coil's geometry. The iterative solvers no longer converged to a solution. The direct solver had to be used but increased the time to find a solution considerably. As an example, with the iterative solver and the coil line object, a solution could be found in approximately one hour. With the 3D solid coil and the direct solver, a solution was found in approximately two days. That is why the coil was modelled using a line object, enabling one to use the iterative solver.

There are multiple different iterative solvers available within Comsol. Luckily, the optimal solver type and settings are automatically set by Comsol for the predefined physics problems. For the induction heating physics, the Flexible Generalized Minimum RESidual iterative method (FGMRES) solver is used. The entire problem is solved using two different studies. The first study solves a frequency-transient step and finds a solution for both the magnetic and electric fields and the heat transfer physics. The first study is used to solve for the first 15 [s] of heating. The second study solves a time-dependent step and only solves the heat transfer physics for computing the cooling phase of the multi-physics problem.

## 5.2. COMSOL MODEL VALIDATION

In order to validate the Comsol model, all heating experiments for both the Helmholtz and the Hairpin coils have been modelled and compared to the experimental results. Both the heating patterns as well as the thermocouple temperatures will be compared. Comparing heating patterns suggests whether Comsol is able to reproduce the thermal behaviour witnessed with heating experiments. Comparing temperatures will give the quantifiable difference between Comsol predictions and measured experimental temperatures.

### 5.2.1. HEATING PATTERN

The heating patterns for the different laminate lay-ups and laminate orientations are analysed and compared with thermal images obtained from induction heating experiments.

#### LAMINATE LAY-UP $[0]_{4S}$

Figure 5.7 shows the actual heating patterns recorded during experiments and Figure 5.8 shows the prediction of the heating pattern computed by the Comsol model for the $[0]_{4S}$ laminate, heated by the Helmholtz coil at 400 [A].

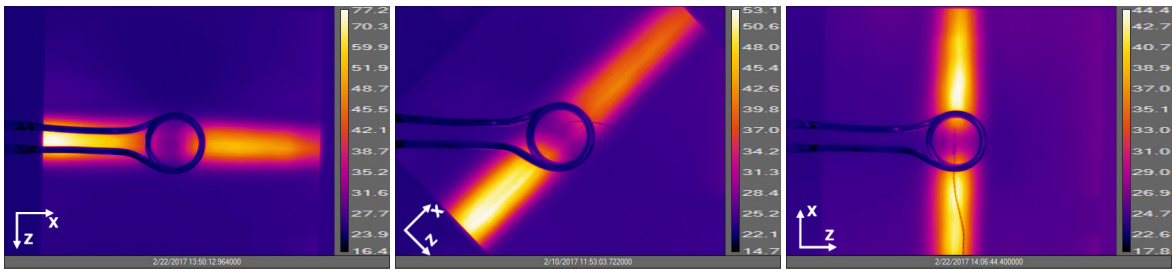

(a) $\alpha = 0[deg]$ (b) $\alpha = 45[deg]$ (c) $\alpha = 90[deg]$

Figure 5.7: Results heating experiments $[0]_{4S}$ laminate, Helmholtz coil at 400 [A] at t = 15 [s]

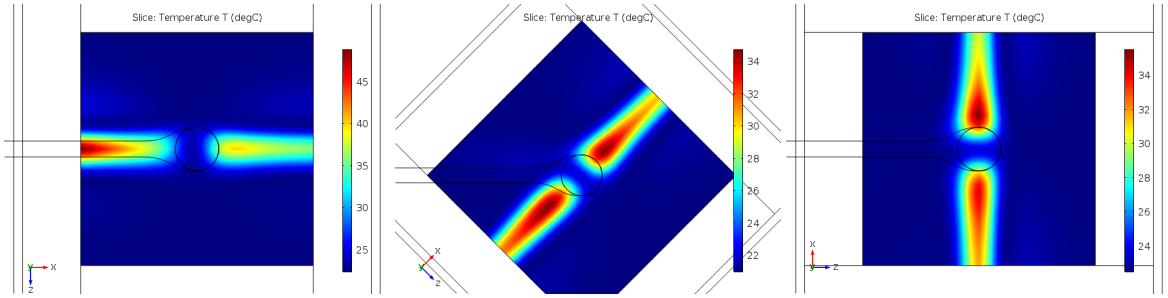


(a) $\alpha = 0[deg]$ (b) $\alpha = 45[deg]$ (c) $\alpha = 90[deg]$

Figure 5.8: Heating pattern prediction Comsol $[0]_{4S}$ laminate, Helmholtz coil, 400 [A] at t = 15 [s]

Figure 5.8 shows how the heating pattern simply rotates with orientation angle of the laminate with respect to the coil. The exact same behaviour was also recorded during experiments, shown in Figure 5.7. The model is even able to take the edge effect into account, witnessed in Figures 5.7a and 5.8a. It shows that Comsol is able to predict the heating pattern that is generated for the $[0]_{4S}$ laminate heated by the Helmholtz coil. The results for the Hairpin coil and the $[0]_{4S}$ laminate also agreed with the experimental results of Chapter 3. These results are included in Appendix F.

**Reason behind heating pattern** With the heating pattern of the Comsol model agreeing with experimental results, one is able to use the model to further understand what is actually causing the heating pattern to stretch over the entire width of the laminate. It is expected that due to the increased resistance the current encounters when going in transverse direction, the current simply spreads over the entire width of the laminate in order to find the path of least resistance. With the conductivity in fibre direction approximately a factor 1400 greater than in transverse direction, the resistance the current encounters in fibre direction is negligible with respect to the resistance encountered in transverse direction. One could use an equivalent circuit of resistors to model the possible current paths the current is able to take. Figure 5.9 shows what this means for the current going through the $[0]_{4S}$ laminate when oriented over an orientation of $\alpha = 0[deg]$.

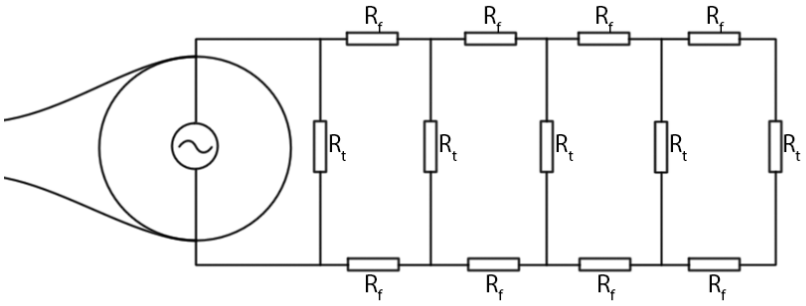


Figure 5.9: Equivalent circuit $[0]_{4S}$ laminate, $\alpha = 0[deg]$

The currents are being generated primarily in the direction of the fibre in the vicinity of the coil. Due to the orientation of the fibres and based on the heating experiments of Chapter 3, the currents then travel in the direction of the fibre and cross the fibres in transverse direction in order to close the circuit loop. Figure 5.9 shows a highly simplified approach into modelling this behaviour. In reality, there are many more possible paths inside the micro-structure of the laminate for the current to follow. The resistances in fibre direction $R_f$ and transverse direction $R_t$ will not all be equal to each other and the emf created by the coil is substituted by an alternating current source. With Kirchhoff's node and loop laws, one can compute the distribution of currents as they cross in transverse direction. This will be based on the relative values for the resistances encountered both in fibre and in transverse directions. The smaller the resistances encountered in fibre direction, the less of an influence they will have on the current paths followed by the eddy currents within the laminate. In other words, the larger the ratio $R_f/R_t$, the more the current will utilise the complete geometry of

the laminate to complete the equivalent circuit within the laminate. This behaviour can be visualised by using the Comsol model and varying the transverse conductivity of the material.

Figure 5.10 shows the transverse current density for varying transverse conductivities of the $[0]_{4S}$ laminate under $\alpha = 90[deg]$. The focus is on the transverse current density $J_z$, due to the generation of heat being primarily dependent on this current density. Note that the orientation of the laminate deviates from the orientation used in Figure 5.9. This orientation was chosen because it does not include the edge effects witnessed for the orientations $\alpha = 0[deg]$ and $\alpha = 45[deg]$.

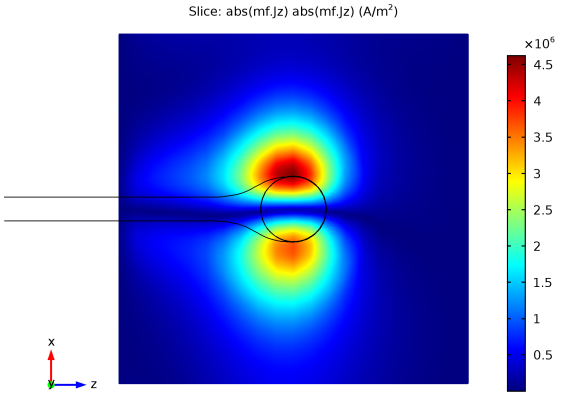


(a) Transverse conductivity $\sigma_T = 18300[S/m]$

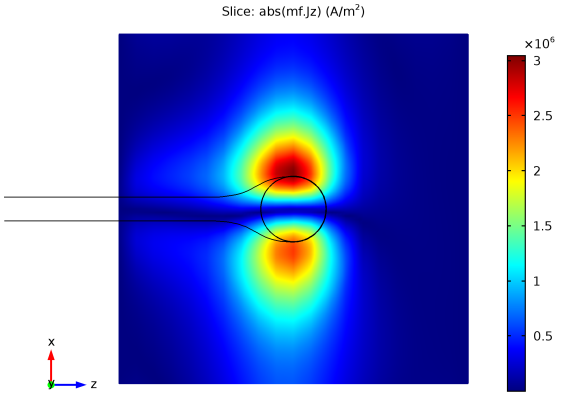


(b) Transverse conductivity $\sigma_T = 10000[S/m]$

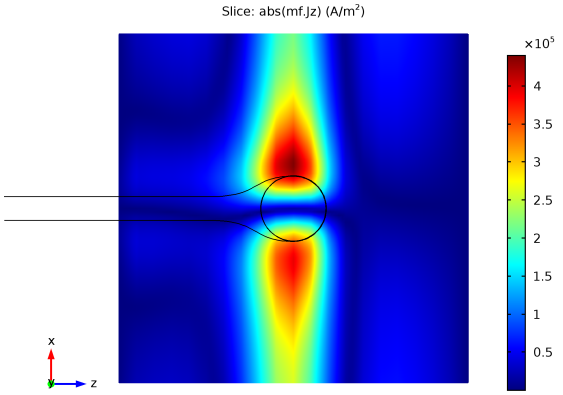


(c) Transverse conductivity $\sigma_T = 1000[S/m]$

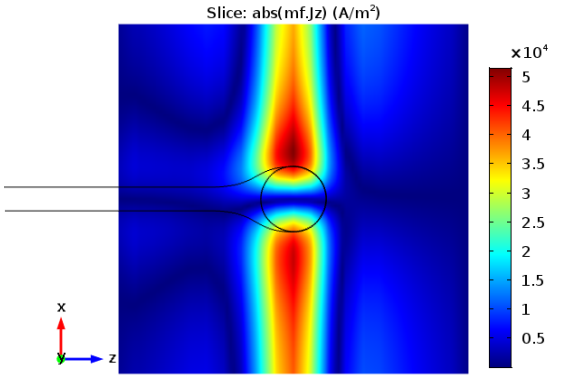


(d) Transverse conductivity $\sigma_T = 100[S/m]$

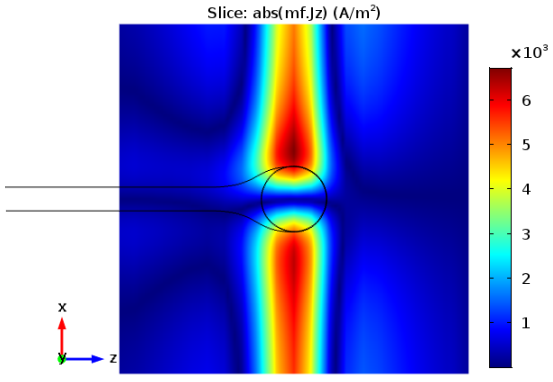


(e) Transverse conductivity $\sigma_T = 12.6[S/m]$

Figure 5.10: Absolute transverse current density with respect to varying transverse conductivity $[0]_{4S}$ laminate, $\alpha = 90[deg]$

Note that the electric conductivity in fibre direction is approximately 18.3 [kS/m] and the measured transverse conductivity is approximately 13 [S/m]. These transverse conductivities correspond to the material properties used to create Figures 5.10a and 5.10e. Figure 5.10 shows that with decreasing transverse electric conductivity, the transverse current density $J_z$ starts spreading over the entire width of the laminate. The resistance encountered when going in fibre direction becomes negligible. Note that there is also a limit in how the current density spreads. Figures 5.10d and 5.10e do not show a difference in transverse current density pattern but only in the amplitude of the maximum current densities. With the transverse current density being dominant in the heating of the $[0]_{4S}$ laminate, the negligible fibre resistance explains why the heating pattern stretches over the entire width of the laminate.

**Maximised heating for $\alpha = 0[deg]$** The heating experiments of Chapter 3 showed an increased maximum temperature to occur when the $[0]_{4S}$ laminate had an orientation of $\alpha = 0[deg]$ with respect to the Helmholtz coil. The results obtained with Comsol agree with these experimental findings. The Comsol model is used to find the reason behind the increased temperatures when the laminate is oriented over $\alpha = 0[deg]$. Examining eddy current densities shows that the eddy current density in fibre direction is maximised when the laminate has a relative angle of 0 [deg] with respect to the coil. The increased eddy current density can be explained when looking at Figure 5.2. A varying coupling distance causes the coil to be closest to the laminate when the copper tubing of the coil is aligned with the fibre orientation within the laminate. This causes an increase in magnetic flux and thus an increase in the induced electric field in the direction of the fibre. When the fibre is thus aligned with this part of the coil, the induced eddy current density is maximised. With the generation of heat depending on this eddy current density, the increase in maximum temperature for the $[0]_{4S}$ laminate under an angle of $\alpha = 0[deg]$, can be explained by looking at the geometry of the coil.

LAMINATE LAY-UP $[0,90]_{2S}$

The heating pattern witnessed for the $[0,90]_{2S}$ laminate and the Helmholtz coil showed maximum heating at distinct locations around the projected location of the coil on the laminate. Figure 5.11 shows the experimentally recorded heating patterns and Figure 5.12 shows the results from the Comsol model for the $[0,90]_{2S}$ laminate heated by the Helmholtz coil.

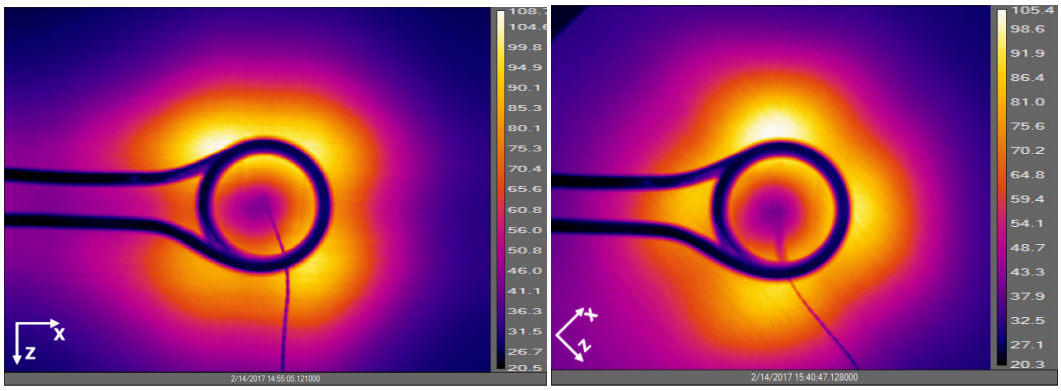


(a) $\alpha = 0[deg]$ (b) $\alpha = 45[deg]$

Figure 5.11: Experimental heating response $[0,90]_{2S}$ laminate, Helmholtz coil, 70 [A] at t = 15 [s]

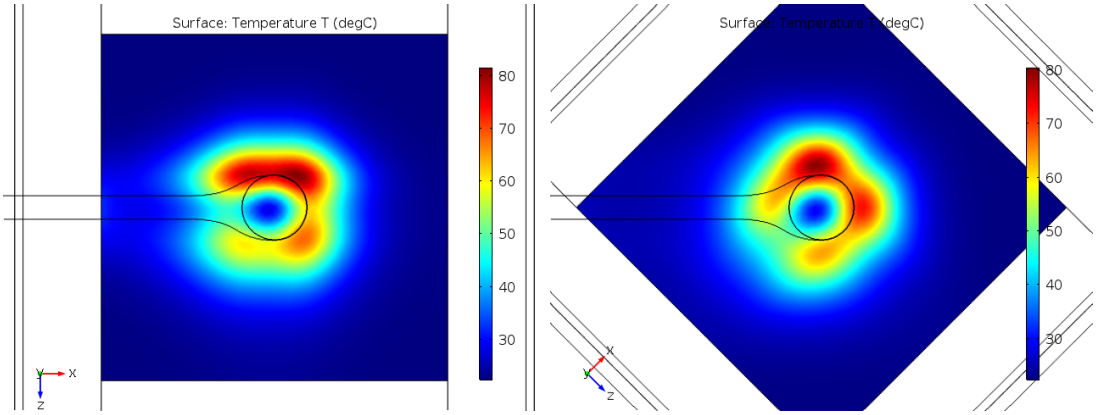


(a) $\alpha = 0[deg]$ (b) $\alpha = 45[deg]$

Figure 5.12: Comsol predicted heating pattern $[0,90]_{4S}$ laminate, Helmholtz coil, 70 [A] at t = 15 [s]

Figure 5.12 shows that Comsol is also capable of predicting the heating pattern of a UD $[0,90]_{2S}$ CF-PEKK laminate, when heated with the Helmholtz coil. There are distinct locations around the coil where heating is maximised. The heating pattern rotates along with the orientation of the laminate with respect to the coil. The results for the Hairpin coil are included in Appendix F and also agree reasonably well with what was recorded during the induction heating experiments. The only difference was with the heating pattern for the orientation of $\alpha = 0[deg]$. Figure 5.13 shows both the actual and the predicted heating patterns for the heating of the $[0,90]_{2S}$ laminate with the Hairpin coil at 150 [A].

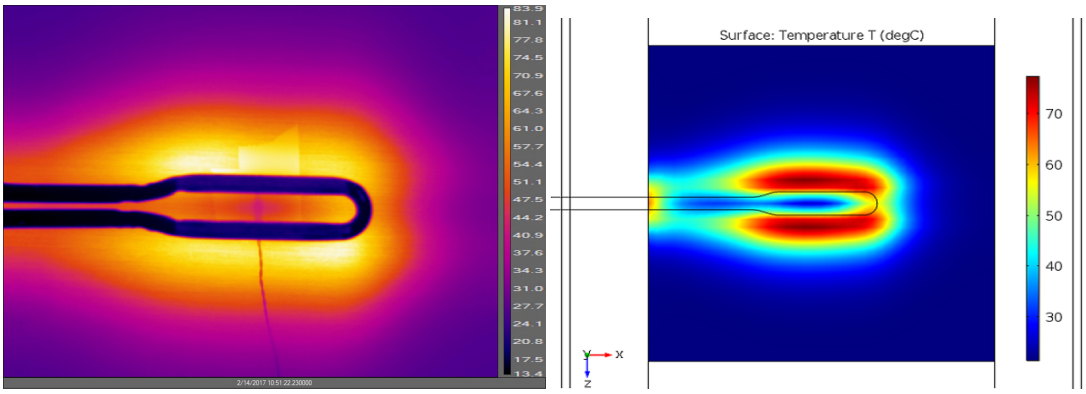


(a) IR-image after 15 [s] heating (b) Comsol prediction after 15 [s] heating

Figure 5.13: Heating pattern comparison $[0,90]_{2S}$ laminate, Hairpin coil, $\alpha = 0[deg]$, $I = 150[A]$

The difference is in the location of the area of maximum heating. With the Comsol model, it is predicted that most of the heat will be generated over an area spread out around the coil. In reality, most of the heat is generated either at the tip of the coil or at the beginning of the geometry where the coil becomes wider. This is the only difference witnessed between the heating patterns of the Comsol models compared to experimental results for the $[0,90]_{2S}$ laminate. This could cause differences to occur between the temperature predictions for the thermocouples located at these areas.

LAMINATE LAY-UP $[45,-45,0,90]_S$

Finally, the quasi-isotropic laminate was modelled. Figure 5.14 shows the recorded thermal images and Figure 5.15 shows the Comsol results for the heating of the $[45,-45,0,90]_S$ laminate, heated by the Helmholtz coil.

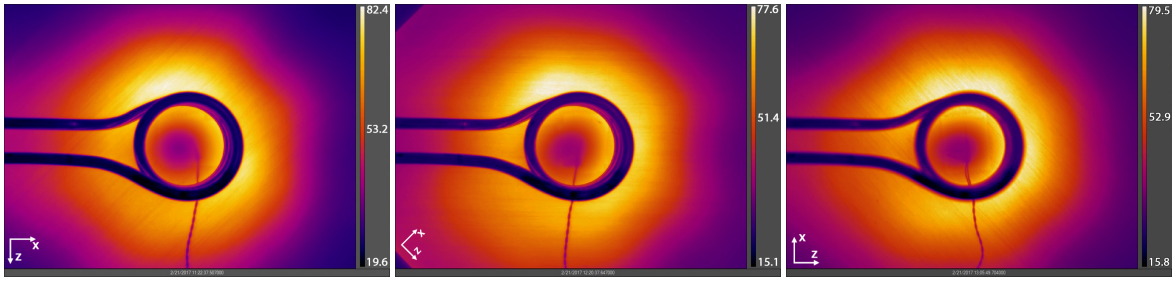


(a) $\alpha = 0[deg]$ (b) $\alpha = 45[deg]$ (c) $\alpha = 90[deg]$

Figure 5.14: Results heating experiments $[45,-45,0,90]_S$ laminate, Helmholtz coil at 70 [A] after 15 [s]

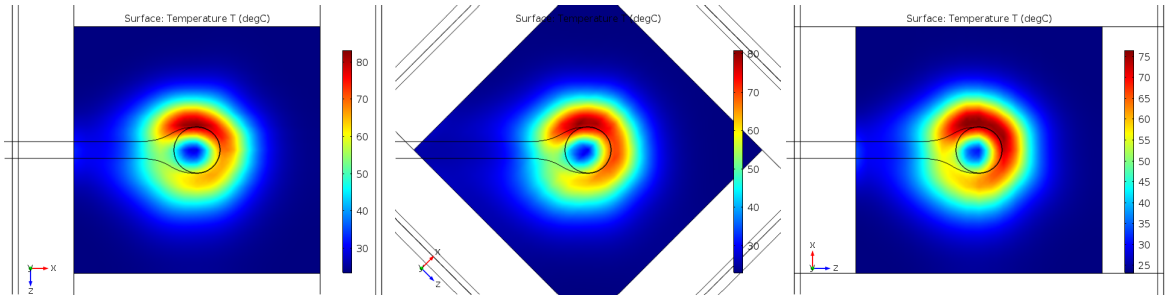


(a) $\alpha = 0[deg]$ (b) $\alpha = 45[deg]$ (c) $\alpha = 90[deg]$

Figure 5.15: Heating pattern $[45,-45,0,90]_S$ laminate, Helmholtz coil, 70 [A] at t = 15 [s]

Again, the heating predictions correspond to the heating patterns witnessed with the experimental results. What stands out is that for the orientation $\alpha = 90[deg]$, the heating pattern seems to be more spread out than for the other orientations. This causes a lower maximum temperature to occur.

The heating pattern results show that Comsol is able to model the multi-physics behaviour the laminate exhibits when being heated by an electromagnetic source. With the separate Comsol models able to predict the heating patterns witnessed experimentally, one can compare the thermocouple temperatures in order to validate the model.

### 5.2.2. THERMOCOUPLE TEMPERATURES

With Comsol being able to predict the heating patterns for the different lay-ups and fibre orientations, the temperatures recorded by the thermocouples will be compared in order to quantify the differences between the model and experiments. All of the raw data is included in Appendix J for both the Helmholtz and Hairpin coils. This appendix also includes the settings used during induction heating experiments. Table 5.1 gives the difference between Comsol and experimental temperatures after 15 [s] of heating.

Table 5.1: Percentage differences Comsol and experimental results thermocouple temperatures

| | | | Thermocouple difference [%] | | | |
|---|---|---|---|---|---|---|
| Coil | Laminate | Orientation [deg] | TC1 | TC2 | TC3 | TC4 |
| Helmholtz | $[0]_{4S}$ | 0 | -24.6 | -27.7 | -19.4 | -22.9 |
| | | 45 | -14.7 | -7.8 | -8.1 | -19.1 |
| | | 90 | -16.9 | -18.7 | -10.1 | -17.7 |
| | $[0,90]_{2S}$ | 0 | -31.8 | 0.4 | -17.2 | -28.9 |
| | | 45 | -24.2 | -24.4 | -13.0 | -23.2 |
| | $[45,-45,0,90]_S$ | 0 | -21.4 | 3.7 | 10.9 | -27.4 |
| | | 45 | -20.5 | 2.5 | 10.8 | -17.3 |
| | | 90 | -17.2 | 3.3 | -1.3 | -11.8 |
| Hairpin | $[0]_{4S}$ | 0 | -4.8 | 11.9 | 12.4 | -3.0 |
| | | 45 | 2.1 | 8.2 | 6.6 | 4.9 |
| | | 90 | -3.3 | -1.7 | -1.9 | -3.1 |
| | $[0,90]_{2S}$ | 0 | -32 | -7.3 | 21.9 | -32.6 |
| | | 45 | 18.8 | 0.8 | -0.5 | 23 |
| | $[45,-45,0,90]_S$ | 0 | -8.0 | 7.5 | 18.2 | -8.7 |
| | | 45 | -1.6 | 15.9 | 21.4 | -1.6 |
| | | 90 | 3.3 | 11.6 | 0.9 | 8.6 |

This section will focus on the largest differences witnessed for the different laminate lay-ups tested. The current section focuses on the temperature results and will analyse these. A complete discussion is added in Section 5.3.

LAMINATE LAY-UP $[0]_{4S}$

Table 5.1 shows the temperature differences recorded for the $[0]_{4S}$ laminate, heated by the Helmholtz and Hairpin coils. Looking at the results for the heating experiments done with the Helmholtz coil and the $[0]_{4S}$ laminate, the biggest differences are witnessed for the orientation of $\alpha = 0[deg]$. Figure 5.16 shows the recorded and predicted thermocouple temperatures.

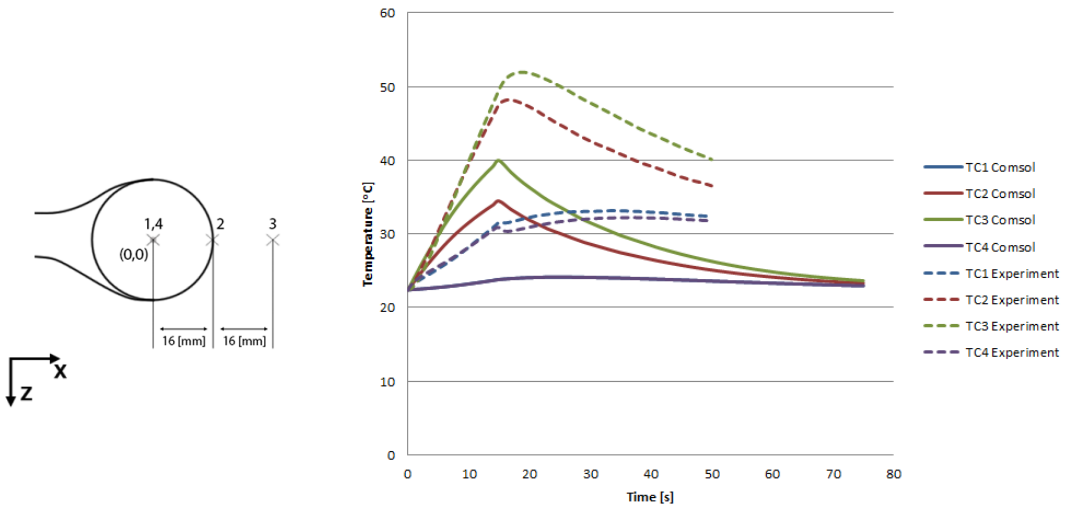


(a) Thermocouple positions

(b) Thermocouple temperature predictions

Figure 5.16: Thermocouple temperatures $[0]_{4S}$ laminate, $\alpha = 0[deg]$, Helmholtz coil, 400 [A]

Figure 5.16a shows the locations of the thermocouples used during induction heating experiments. Thermocouples TC1 and TC4 are located in the centre of the laminate on the bottom and top surface of the laminate respectively, relative to the coil. Thermocouples TC2 and TC3 are located on the bottom of the laminate relative to the coil. Figure 5.16b shows how all of the temperatures are underestimated, with the biggest differences

occurring for thermocouples TC1 and TC4. From the results of Chapter 3, one can see that these thermocouples are not located in an area where heat is being generated. Thermocouples TC1 and TC4 only heat up, due to heat conduction from hotter areas. With all of the thermocouples showing an under-estimation of the occurring temperatures, it is understandable that the centre temperature prediction will also be underestimated. The biggest temperature difference recorded after 15 [s] of heating comes from thermocouple TC2 and equals an under-estimation of 27.7%. One of the other differences that one can see from the results of Figure 5.16b, is the fact that the laminate cools down quicker with the Comsol model than during experiments. The Comsol induction heating model is able to predict the correct heating pattern, but lacks the ability to predict the correct occurring temperatures. Section 5.3 will discuss the possible causes for the deviation, after reviewing all of the model's results.

Looking at the results for the $[0]_{4S}$ laminate heated by the Hairpin coil, one can see that the Comsol predictions are actually much closer to the experimental results. The biggest differences were recorded for the orientation of $\alpha = 0[deg]$ and equal approximately 12.4% after 15 [s] of heating. Figure 5.17 shows the recorded and predicted thermocouple temperatures for the $[0]_{4S}$ laminate under an orientation of $\alpha = 0[deg]$, heated by the Hairpin coil.

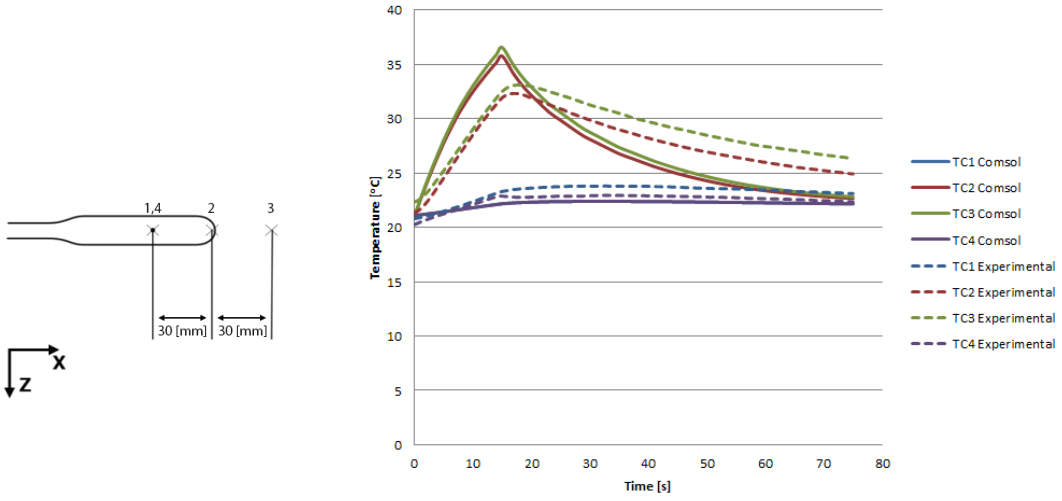


(a) Thermocouple positions

(b) Thermocouple temperature predictions

Figure 5.17: Thermocouple temperatures $[0]_{4S}$ laminate, $\alpha = 0[deg]$, Hairpin coil, 400 [A]

Figure 5.17b shows how the differences between temperatures are smaller than what was recorded for the Helmholtz induction heating experiments. One important difference however is the fact that the temperatures are being overestimated in this case. This difference will be discussed in Section 5.3. One important aspect to take into account is the fact the temperatures cool down quicker in the Comsol model than what was stored during experiments. This could imply incorrect thermal material properties or thermal boundary conditions.

Comsol is able to predict the heating patterns that occur during induction heating but is limited in the prediction of temperatures. The maximum temperature prediction for the $[0]_{4S}$ laminate heated by the Helmholtz coil is underestimated. The same heating experiments performed with the Hairpin coil are causing an overestimation of the maximum temperatures predicted by Comsol. A maximum difference of 27.7% was recorded. Whether this difference occurs for the other lay-ups as well, will be investigated next.

#### LAMINATE LAY-UP $[0,90]_{2S}$

Looking at the heating results for the $[0,90]_{2S}$ laminate and the Helmholtz coil (Table 5.1), one can see that the biggest differences are witnessed when the laminate is oriented over an angle of $\alpha = 0[deg]$. Figure 5.18 shows the thermocouple temperatures recorded for the $[0,90]_{2S}$ laminate under an orientation $\alpha = 0[deg]$, heated by the Helmholtz coil.

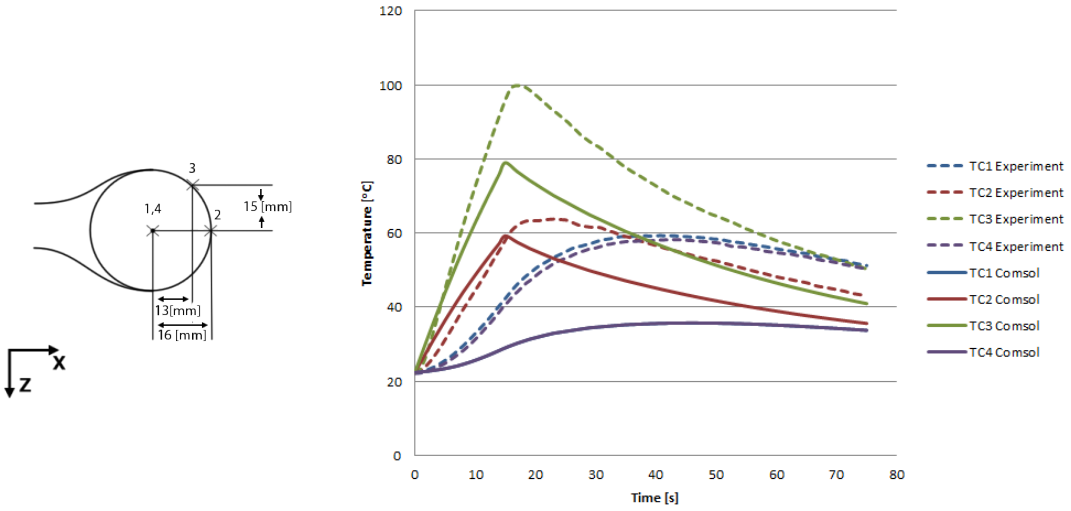


(a) Thermocouple positions (b) Thermocouple temperature predictions

Figure 5.18: Thermocouple temperature predictions $[0,90]_{2S}$ laminate, $\alpha = 0[deg]$, Helmholtz coil, 70 [A]

Figure 5.18a shows the locations of the thermocouples, relative to the coil. Thermocouples TC1 and TC4 are always at the centre of the laminate on the bottom and top surface respectively, relative to the coil. Looking at Figure 5.18b, one can again see that the temperatures are being underestimated, just as was the case for the $[0]_{4S}$ heated by the Helmholtz coil. The biggest differences again are recorded for the thermocouples located in the centre of the laminate. The centre of the laminate heats up purely based on the conduction of heat from hotter areas within the laminate. Deviating centre temperature could imply incorrect thermal properties of the material. At t = 15 [s], the power is turned off and the cooling phase is initiated. Looking at the temperature slopes during the cooling phase, one can see that cooling now is similar between the Comsol model and the experimental results.

Figure 5.19 shows the temperatures recorded during heating the $[0,90]_{2S}$ laminate under an orientation of $\alpha = 0[deg]$ with the Hairpin coil.

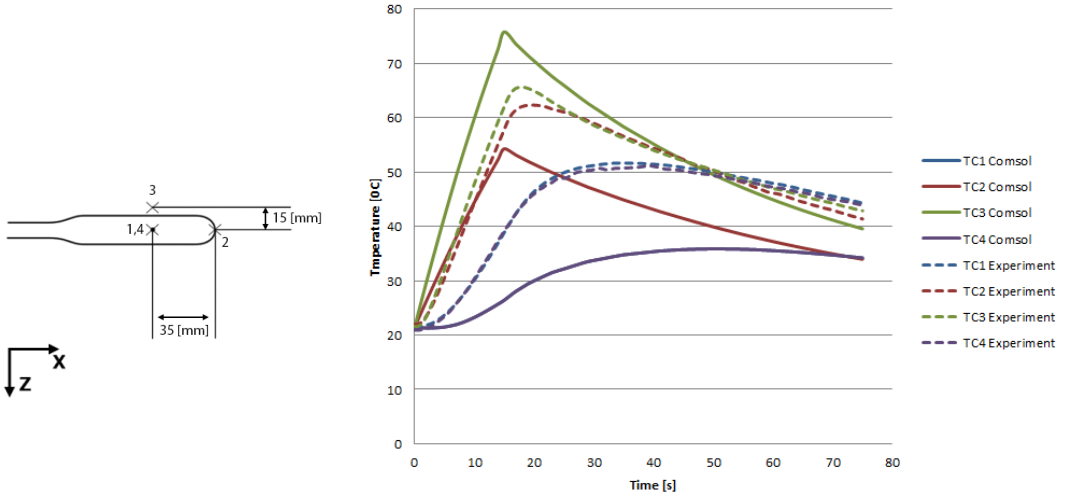


(a) Thermocouple positions (b) Thermocouple temperature predictions

Figure 5.19: Thermocouple temperature predictions $[0,90]_{2S}$ laminate, $\alpha = 0[deg]$, Hairpin coil, 150 [A]

Figure 5.19b shows how thermocouple TC3 is being overestimated and TC2 underestimated. Looking at Figure 5.13, one can see that is likely to be caused by minor differences in the prediction of the heating pattern for the Hairpin coil. The biggest differences are again recorded for the centre of the laminate.

LAMINATE LAY-UP $[45,\text{-}45,0,90]_S$

The final lay-up modelled was the $[45,\text{-}45,0,90]_S$ laminate. Table 5.1 shows that the temperature predictions for the Helmholtz coil show good agreement for the thermocouples TC2 and TC3 and again show an under-estimation for thermocouples TC1 and TC4 for all three orientations. Figure 5.20 shows the thermocouple locations and the recorded temperatures with respect to time for the $[45,\text{-}45,0,90]_S$ laminate at an orientation of $\alpha = 0[deg]$, heated by the Helmholtz coil at 70 [A].

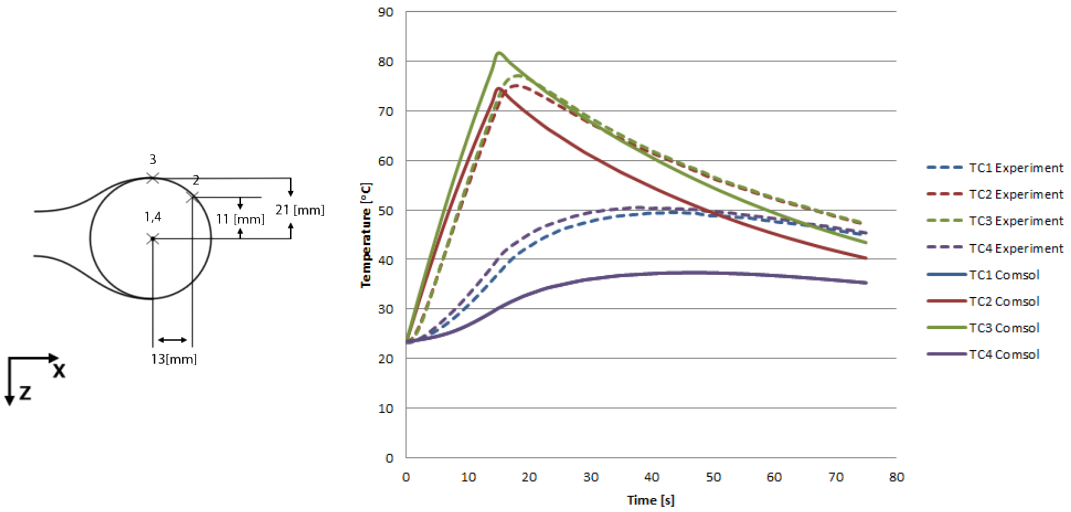


(a) Thermocouple positions (b) Thermocouple temperature predictions

Figure 5.20: Thermocouple temperature predictions $[45,\text{-}45,0,90]_S$ laminate, $\alpha = 0[deg]$, Helmholtz coil, 70 [A]

Figure 5.20b shows similar temperatures recorded for thermocouples TC2 and TC3. The centre of the laminate is still underestimated with respect to the temperature prediction done by Comsol. The overall transient temperature response predicted by Comsol corresponds with what was measured experimentally.

Figure 5.21 shows the thermocouple locations and temperatures predicted for the $[45,\text{-}45,0,90]_S$ laminate under an orientation of $\alpha = 0[deg]$, heated by the Hairpin coil.

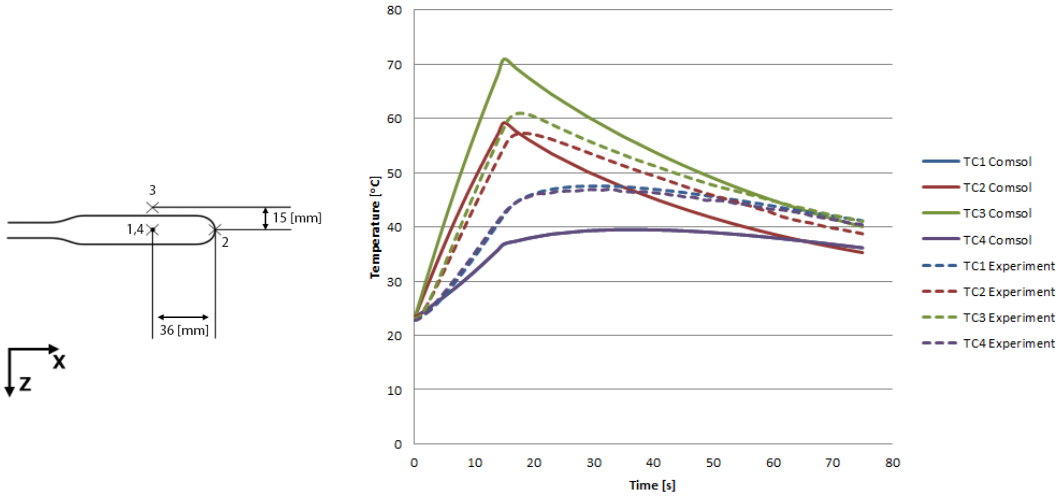


(a) Thermocouple positions (b) Thermocouple temperature predictions

Figure 5.21: Thermocouple temperature predictions $[45,\text{-}45,0,90]_S$ laminate, $\alpha = 0[deg]$, Hairpin coil, 150 [A]

The temperatures predicted for the Hairpin coil and the $[45,\text{-}45,0,90]_S$ laminate show an over-estimation of the temperatures of thermocouple TC3. The same is happening as for the $[0,90]_{2S}$ laminate heated by the Hairpin

coil. Comsol predicts the maximum generation of heat to occur alongside the length of the Hairpin coil, as shown in Figure 5.13. The IR-images however show the location of maximum heat generation to be more shifter towards the tip of the coil. This difference in heating pattern causes the difference in temperatures. The centre of the laminate is again being underestimated in temperature prediction. Examining the cooling phase, it seems that the laminate cools down faster in the Comsol model than what was recorded during experiments.

## 5.3. COMSOL RESULTS DISCUSSION

**Centre temperatures and cooling** One of the major differences between the Comsol predictions and the experimental results was the fact that the centre of the laminate was consistently being underestimated by the Comsol model based on temperature increases. This effect was witnessed for all of the laminate lay-ups, orientations and coils used. From the results of Chapter 3, one can see that the amount of heat being generated at the middle of the laminate is limited. Heating of the centre of the laminate depends mainly on the conduction of heat from hotter areas within the laminate. Consistent errors in the temperature increase of the centre of the laminate could be caused by the following:

- Overall underestimation of temperature increases
- Incorrect thermal material properties
- Inaccuracies occurring during experiments

When all of the temperatures are underestimated and the temperature at the centre being dependent on the conduction of heat, it makes sense that the centre of the laminate will also be underestimated. However, looking at Table 5.1, one can see that the temperature at the centre of the laminate is underestimated, even when the other thermocouple temperatures are overestimated. A different possible cause for the deviation is that the thermal material properties used in the Comsol model were inaccurate. The thermal conductivity was measured only at three temperature points and the relation was assumed linear with respect to temperature. The thermal conductivity should be properly measured at additional temperatures to include accurate temperature dependent heat conductivity properties in the Comsol model. The thermal material properties were either based on a limited amount of data points or on a reference material taken from literature. Proper investigation of the thermal material properties of the UD CF-PEKK material should be conducted. Finally, errors in the experimental temperature data could also be present. The temperatures were measured with the help of thermocouple wires. These have a certain exposed wire length to them. The locations of the thermocouple wires are based on the locations of the tips of the wires. Due to a lack in knowledge when performing the induction heating experiments, it was unknown that actually, the temperature is measured at the location where the exposed thermocouple wires first touch. There is a large probability that this does not correspond with the tip of the thermocouple wire. This means that the experimental temperature measurements were performed at locations away from the centre. This explains why the experimental temperature predictions are much higher. Recommended is to redo the induction heating experiments and use thermocouple wires containing only one point of contact between the exposed metal wires.

Comparing the temperatures of the thermocouples during the cooling phase showed how the Comsol prediction of the cooling of the laminate was overestimated for certain induction heating experiments, but was accurate for other. One of the mechanisms that cool the laminate during experiments was heat convection over the free surfaces of the laminate. During the induction heating experiments it was noted that the convection of air was different, between the different experiments performed. This was caused by the cooling equipment, cooling the copper coil. The entire induction heating set-up was located in a small room, in which also the cooling equipment was located. At random instances, the cooling equipment started blowing air into the room, increasing the effective air flow over the laminate. This will affect the temperatures measured and could cause more rapid or slower cooling between the separate induction heating experiments. Recommended is that the induction heating experiments are once again performed, ensuring the environment is kept constant during measurement.

**Differences between coils** Comparing the heating temperature results for the different coils, one can see another effect occurring. Table 5.1 shows how the temperatures for the laminates heated by the Helmholtz coil are almost all underestimated. Comparing this with the heating experiments performed with the Hairpin coil,

one can see that the temperature predictions are actually more often overestimated. With the material properties, laminate lay-ups and laminate orientations kept constant between coils, the only difference is the coil itself and possible environmental conditions. Both coils are modelled as line objects, following their actual shape. One difference between the coils however is the fact that the Helmholtz coil has a varying coupling distance with respect to the laminate. What is meant, is shown in Figure 5.2. When the induction heating experiments were performed, the importance of the coupling distance on the temperature increase was yet unknown. The coupling distance was set approximately equal to 10 [mm] with the help of a ruler. Next to the fact that a ruler is much too inaccurate, the location used for defining the coupling distance of the Helmholtz coil varied between heating experiments. The coupling distance has a large influence on the temperature increases in the laminates. Before addressing any problems within the Comsol model itself, it is of key importance that the experimental results are deemed accurate. It is recommended that the induction heating experiments are repeated and the coupling distance is measured using a different approach than a ruler. There are multiple methods of setting the coupling distance more accurately.

- Using the rotation wheel of the plateau on which the generator resides.
- Using a calliper.
- using a reference material

The generator and coil are moved up and down by setting the plateau on which they reside. A wheel underneath the plateau is rotated clockwise to move the plateau up and counter-clockwise to move the plateau down. One can let the coil touch the surface of the laminate, and then count the number of rotations the wheel makes to reach a coupling distance of 10 [mm]. This is an accurate approach into keeping the coupling distance constant between heating experiments. One full rotation equals approximately 1 [mm] in movement of the plateau. In order to accurately set the coupling distance to 10 [mm], a calliper can be used. The accuracy of the calliper is much higher than that of a ruler and the human eye. Attaching one part of the calliper to a stationary part of the set-up, and the movable part of the calliper to the plateau, one can accurately define the coupling distance. One other approach of having constant coupling distances is to use a reference material. When the coil is set to the correct distance, one could heat up a reference material at certain amperage for certain duration. The temperatures that are recorded should always be the same when the coupling distance is kept the same. One should measure the temperature increases of the reference material once at a coupling distance of 10 [mm]. When doing induction heating experiments at later instances, one could check whether the coupling distance is set correctly, by repeating the heating experiment of the reference material before doing anything else. When the temperatures excited in the reference material correspond to the temperatures found when the coupling distance was 10 [mm], the coupling distance is set.

The inaccurate coupling distance for the Helmholtz coil could explain why the prediction in temperatures for the heating experiments done with the Helmholtz coil were almost all underestimated. Not the lowest point of the coil was used to measure the distance between coil and laminate, but simply a point that was easiest to reach. This means that the true coupling distance was smaller than what was used during modelling. One other aspect worth considering in the modelling of the coil is the fact that a line object is used. When alternating currents flow through a conducting material, the skin effect causes the currents to primarily reside on the outer surfaces of that conducting material. Next to that, the proximity effect adds to that and causes an unsymmetrical distribution of charge over the cross-section of the copper tubes used for the copper coils. This has been explained in Section 1.2.4. This unsymmetrical distribution of charge could influence the heating of the UD CF-PEKK laminates. This effect could never be included when using a line object for the coil geometry. Recommended is to model the coil as a hollow solid and see what the influence is on the temperature increase predicted in Comsol. Due to meshing errors, this was not included in the current research.

**Differences between laminate lay-ups** Heating with the Helmholtz coil showed good correspondence between temperatures for the $[45,\text{-}45,0,90]_S$ laminate and an underestimation of temperatures for the $[0]_{4S}$ and $[0,90]_{2S}$ lay-ups. This effect was not recorded for the heating experiments performed with the Hairpin coil. The only possible explanation for this deviation to occur is the possible errors in the experimental procedure used during the induction heating experiments. The heating experiments should be re-evaluated and performed multiple times to get a feeling into the standard deviation witnessed for the experimental results. Only when the experimental results are deemed correct, can one know for a fact whether the model is able or unable to predict the temperatures of the UD CF-PEKK laminates during induction heating.

## 5.4. CONCLUSION AND RECOMMENDATIONS

Different computational models were written in order to find a method of modelling the inductive behaviour of the UD CF-PEKK material. The Ansys model showed the importance of electric contact between plies and showed deviating results for both the heating patterns and temperature predictions. Based on these findings, it was decided to continue modelling with the help of Comsol Multiphysics. A computational model was written in which all plies were modelled separate, including the material properties from Chapters 2 and 4. Validation showed a converging computational model, capable of predicting the correct heating patterns witnessed from heating experiments for the separate laminate lay-ups. The differences between thermocouple temperatures showed that there is still a lot of room for improvement. One of the main points of attention is focussing on the repeatability of the heating experiments themselves. This research has neglected the standard deviation also present in the measurement of the temperatures during the heating experiments. Next to that, the thermal properties of the UD CF-PEKK material were either based on literature or on a limited amount of data points. The thermal properties also influence the temperature increase and thermal behaviour of the UD CF-PEKK material during induction heating. Additional research should be performed into finding the thermal properties of the material. Finally, the model included several simplifications which all could influence the final results found. One of them was the simplified geometry of the coil. Additional research should be performed on the effect of using solid or wire objects for modelling the coil geometry. All in all, one is able to model the induction heating behaviour of UD CF-PEKK laminates. However, in order to have accurate temperature predictions for all different lay-ups and coils, a lot of work still remains.

# 6

# CONCLUSION AND RECOMMENDATIONS

This report investigated the thermal response of Uni-Directional (UD) Carbon Fibre (CF)-Poly(Ether-Ketone-Ketone) (PEKK) laminates, when heated by induction heating. It tried to answer the main research question:

*"What is the influence of the fibre lay-up, fibre orientation and the inherent electrical properties of fibre and matrix of an UD CF-PEKK laminate on the heat generation during induction heating and how can one model this behaviour?"*

The problem was divided into two main sub-parts. First, it tried finding an answer to what is actually generating the heat and second, how one could model this induction heating phenomenon. All in all with respect to how this is being influenced by fibre lay-up, fibre orientation and the electric properties of fibre and matrix.

**Which heating principle is dominant in the heating of UD lay-up CF-PEKK laminates?** It is stated that the heating principle dominant in the heating of the UD CF-PEKK laminates is Joule heating at the fibre-fibre junctions. this is based on experimental results. First, thermal images showed most of the heat to be generated at the locations where the currents were forced to go into a direction perpendicular to the fibre. This was noticed for both of the $[0]_{4S}$ and $[0,90]_{2S}$ laminates and could be assumed for the $[45,-45,0,90]_S$ laminate. Second, the conductivity measurements showed non-zero conductivity for both transverse and through thickness measurements of the UD CF-PEKK material. This indicates the presence of electric current paths, through which the currents will run. Third, microscopy images of the cross-sections of the different laminate lay-ups showed fibre-fibre contact to exist. This was present in both through-the-thickness as in transverse direction. Last, the material did not show any capacitive behaviour when subjected to an Alternating-Current (AC). This indicates that there is no accumulation of charge happening inside of the material. This will make Joule heating the only form of heating present during induction heating. With Joule heating maximised at the locations where the conductivity is minimised.

This report sets itself apart for making the distinction between the volume fibre ply conductivity and an interface resistivity present between fibre plies. Caused by an increase in the presence of matrix at the interface, any currents going in the thickness direction of the laminate will encounter greatest resistance when crossing this interface. The interface resistivity is found to be dependent on relative fibre ply angles and was taken into account when modelling the induction heating of UD CF-PEKK laminates. This resulted in constant material properties and varying constraints between fibre plies. This makes for a generalisable approach to modelling laminates of different fibre ply lay-ups. The fibre orientation and fibre lay-up dictate the pattern of heat generation due to the maximised electric conductivity in fibre direction. The UD lay-up causes an increase in the resistance between fibre plies, causing junction heating through thickness to be the dominant form of heating for the UD CF-PEKK laminates. The fact that the PEKK matrix is a dielectric matrix containing dipoles does not seem to affect the generation of heat due to the absence of charge accumulation within the UD CF-PEKK laminates.

**Is it possible to model the electromagnetic induction heating of UD CF-PEKK laminates and accurately predict temperatures within an error limit of 10%?** A computational model was written in which all plies were modelled separately, including the material properties found in Chapters 2 and 3. Validation showed a converging computational model, capable of predicting the correct heating patterns witnessed from heating experiments for the separate laminate lay-ups, laminate orientations and coils. The influence of the fibre orientation and fibre lay-up, based on the inherent properties of fibre and matrix, were correctly implemented in the model. The model can be used to increase one's knowledge into what is happening inside of the laminates when heated by induction. When comparing all of the thermocouple temperatures, it showed conflicting results. Temperatures predicted during induction heating tests performed with the Hairpin coil, matched better

with experimental results than the results obtained with the Helmholtz coil. The temperature differences for the heating of the $[45,\text{-}45,0,90]_S$ laminate were much more accurate than the same predictions for the $[0,90]_{2S}$ and $[0]_{4S}$ laminates heated by the Helmholtz coil. It is expected that most of the deviations occur from errors in the experimental results obtained during an early stage of the project. The computational model could not be validated based on the error limit of 10%. There are different recommendations that can be made that should improve the results of the model.

## 6.1. RECOMMENDATIONS

There are different recommendations that can be made, focussing on different parts of the research. The main focus for improving the computational model however, should be put on finding the correct thermal material properties and on the repeatability of the experimental induction heating experiments.

**Thermal material properties** The thermal properties used to model the induction heating of the UD CF-PEKK material were based on a limited amount of data points or on a reference material taken from literature. It is recommended to properly measure the thermal properties of the material with respect to temperature. It is recommended to focus on the thermal conductivity of the material.

**Thermal imaging** In Chapter 3, the Infrared (IR)-camera was used to witness the thermal response of the UD CF-PEKK material to an electromagnetic wave induced by the coil. Amperage settings were determined based on the temperature increase of the material after 15 [s] of heating. Degradation of the material was prevented, in order to enable one to do multiple experiments with the same material. Recommended is to reduce the duration of the induction heating experiments and increase the amperage through the coil. The larger the current going through the coil, the better the thermal response of the material is visualised. A total duration of 15 [s] of heating was chosen to also incorporate the transient thermal response of heat conduction. Afterwards, this was deemed less important. The increase in temperature of the material was approximately linear with respect to time and the transient thermal behaviour could also be visualised by looking at the cooling phase after induction heating.

**Electric material properties** The electric conductivity of the material was found by utilising the experimental set-up described in Chapter 2. In fibre direction, it was found that this electric conductivity was very dependent on the quality of the contact between the samples and the copper terminals. This dependency was taken into account by using a thermal camera to visualise current paths. When one does not have the ability to use a thermal camera, it is recommended to make the geometry of the samples such that the total resistance measured increases. Increases the sample resistance will increase the accuracy of the resistance measurement. This can be achieved by increasing the aspect ratio of the sample geometry. A completely different method of measuring could also be utilised. Etching away the matrix from the sample's ends, exposing the carbon fibres, one could make the contact between the multimeter terminals and carbon fibres directly. No need for any clamping devices, possibly improving the electric conductivity measurement results in fibre direction.

**Surface resistivity** This report proposed a method for finding the surface resistivity between fibre plies. The surface resistivity was found, based on the through-thickness resistance measurements done on four different lay-ups. When one has the resources, it is also possible to manufacture laminate lay-ups consisting of varying amount of plies. By varying the number of plies, one varies the amount of interfaces within the laminate lay-up and the total thickness of the laminate. This offers a more general approach into finding the contact resistivities dependent on the relative fibre angles.

**Standard deviation experimental results** One of the main points of attention is focussing on the repeatability of the heating experiments themselves. This research has neglected the standard deviation also present in the measurement of the temperatures during the heating experiments. The locations of the thermocouples, the influences of the environment and most of all, the measurement of the coupling distance between coil and laminate. All will influence the experimental temperatures found. It is expected that these measurements are not accurate and should be repeated.

**Computational model** The computational model included a simplified coil geometry. As explained, this will never be able to model the distribution of currents with respect to the coil's cross-section. This distribution of currents originates from the skin depth and proximity effects present in conducting materials exposed to alternating currents. It is recommended to investigate whether this effect can be modelled within Comsol and if it has a large influence on the increase of temperature predicted by Comsol.

# BIBLIOGRAPHY


[1] T. Kruse and T.A. Schmid Fuertes. “Bonding of CFRP primary aerospace structures - Boundary conditions for certification in relation with new design and technology developments”. In: *Society for the advancement of material and process engineering* (2013).

[2] A. da Costa, E. Botelho, and M. Costa. “A review of welding technologies for thermoplastic composites in aerospace applications”. In: *Journal of aerospace technology and management* 4 (2012), pp. 255–265.

[3] W. Lin and O. Buneman. “Induction heating model for graphite Fiber/Thermoplastic matrix composites”. In: *SAMPE Journal* 27.6 (Nov. 1991), pp. 45–51.

[4] A. Yousefpour, M. Hojjati, and J. Immarigeon. “Fusion Bonding/welding of thermoplastic composites”. In: *Thermoplastic composite materials* 17 (July 2004), pp. 303–341.

[5] Federal Aviation Administration. *Advisory circular*. Composite aircraft structure. U.S. Department of Transportation, Sept. 2009.

[6] C. Ageorges, L. Ye, and M. Hou. “Advances in fusion bonding techniques for joining thermoplastic matrix composites: a review”. In: *Composites part a: applied science and manufacturing* 32 (2001), pp. 839–857.

[7] T. Kruse, T. Korwien, and S. Heckner. “Bonding of CFRP primary aerospace structures - Crackstopping in composite bonded joints under fatigue”. In: *International conference on composite materials* (2015).

[8] E.M. Silverman and R. Griese. “Joining methods for graphite/PEEK thermoplastic composites”. In: *Sampe Journal* 25 (1989), pp. 34–38.

[9] I.F. Villegas et al. “Process and performance evaluation of ultrasonic, induction and resistance welding of advanced thermoplastic composites”. In: *Journal of thermoplastic composite* 26.8 (2012), pp. 1007–1024.

[10] P.G. OSaughnessey, M. Dube, and I.F. Villegas. “Modeling and experimental investigation of induction welding of thermoplastic composites and comparison with other welding processes”. In: *Journal of composite materials* (2015).

[11] D. Stavrov and H.E.N. Bersee. “Resistance welding of thermoplastic composites-an overview”. In: *Composites part A: Applied Science and Manufacturing* 36.1 (2005), pp. 39–54.

[12] M.H.J. Doldersum. *Industrialization of thermoplastic control surfaces*. Tech. rep. GKN Fokker Aerostructures, June 2014.

[13] W.P. van Rossum. *Inductive behavior carbon composites*. Internal technical report. Kok & Van Engelen composite structrures BV, June 2014.

[14] M. Maissan. *Analysis and improvement of a finite element model for an induction welding process*. Internal technical report. Kok & Van Engelen composite structrures BV, Jan. 2015.

[15] S. Tijhuis. *Inudction welding of thermoplastic grid frame panel S004*. Internal technical report. Kok & Van Engelen composite structrures BV, Jan. 2015.

[16] R. van Holland. *Induction welding of thick laminates: Third year internship of InHolland Aeronautical Engineering*. Internal technical report. Kok & Van Engelen composite structrures BV, Apr. 2016.

[17] C.A. Butler, R.L. McCullough R. Pitchumani, and J.W. Gillespie. “An analysis of mechanisms governing fusion bonding of thermoplastic composites”. In: *Journal of thermoplastic composite materials* 11 (July 1998), pp. 338–363.

[18] R. Wolfson. *Essential university physics*. Vol. 2. Pearson Addison-Wesley, 2007, pp. 331–530.

[19] R. Rudolf, P. Mitschang, and M. Neitzel. “Induction heating of continuous carbon-fibre reinforced thermoplastics”. In: *Composites part A: applied science and manufacturing* 31 (May 2000), pp. 1191–1202.

[20] M. Duhovic et al. “Simulating the joining of composite materials by electromagnetic induction”. In: *12th international LS-DYNA users conference* 2 (June 2012).

[21] M. Didi et al. “Simulating the induction spot welding of hybrid material joints”. In: *10th European LS-DYNA conference* (2015).

[22] T. Ahmed, D. Stavrov, and H. Bersee. “Induction welding of thermoplastic composites - An overview”. In: *Composites part A - Applied science and manufacturing* 37 (2006), pp. 1638–1651.

[23] M. Humbert and P. Mitschang. “Characterization and modification of the temperature distribution during continuous induction welding”. In: *16th European conference on composite materials* (June 2014).

[24] H.J. Kim et al. “Development of a numerical model to predict in-plane heat generation patterns during induction processing of carbon fiber-reinforced prepreg stacks”. In: *Journal of composite materials* 37.16 (2003), pp. 1461–1483.

[25] S. Yarlagadda et al. “A study on the induction heating of conductive fiber reinforced composites”. In: *Journal of composite materials* 36.4 (2002), pp. 401–421.

[26] R.C. Metaxas and R.J. Meredith. *Industrial Microwave Heating Industrial Microwave Heating*. 1983. ISBN: 9780906048894.

[27] D.M.P. Mingos and D.R. Baghurst. “Applications of Microwave Dielectric Heating Effects to Synthetic Problems in Chemistry”. In: *Chemical Society Reviews* 20.1 (1991), pp. 1–47.

[28] Agilent Technologies. *Agilent - Basics of measuring the dielectic properties of materials*. Application note. Agilent. 2006.

[29] R. Wolfson. *Essential university physics*. Vol. 2. Pearson Addison-Wesley, 2007, pp. 264–330.

[30] L.M. Jiji. *Heat Convection*. New York: Springer, 2006.

[31] W.C. Reynolds and P. Colonna. *Thermodynamics: Fundamentals and engineering applications*. Cambridge University Press. 40 West 20th Street New York, 2016.

[32] S.T. Holmes and J.W. Gillespie. “Thermal analysis for resistance welding of large-scale thermoplastic composite joints”. In: *Journal of reinforced plastics and composites* 12 (June 1993), pp. 723–736.

[33] C. Ageorges et al. “Characteristics of resistance welding of lap shear coupons. Part I : Heat transfer”. In: *Composites Part A: Applied Science and Manufacturing* 29.8 (1998), pp. 899–909.

[34] M. Duhovic et al. “Advanced 3D finite element simulation of thermoplastic carbon fiber composite induction welding”. In: *16th European conference on composite materials* (June 2014).

[35] P. Mitschang, R. Rudolf, and M. Neitzel. “Continuous induction welding process, modelling and realisation”. In: *Thermoplastic composite materials* 15 (Mar. 2002), pp. 127–153.

[36] F. Caretto. “Studying the induction welding process applied to thermoplastic-matrix composites”. In: *Studi&recerche* (2011), pp. 103–111.

[37] A.K. Miller et al. “Joining of composite materials by induction heating”. In: *United states Patent* (Aug. 1993). Patent number:5240542.

[38] S. Pappada et al. “Induction welding of PPS-Carbon composites: modeling and experimental results”. In: *19th international conference on composite materials* (July 2013).

[39] S. Pappada et al. “Fabrication of a thermoplastic matrix composite stiffened panel by induction welding”. In: *Aerospace science and technology* 43 (Mar. 2015), pp. 314–320.

[40] T. Bayerl et al. “The heatin of polymer composites by electromagnetic induction - a review”. In: *Composites part A* 57 (2013), pp. 27–40.

[41] S.L. Semiatin. *Elements of induction heating: design, control and applications*. ASM International, 1988.

[42] S. Pappada et al. “Finite element simulation to support continuous induction welding of PPS-Carbon composite”. In: *SEICO 13* (2013), pp. 358–363.

[43] M. Duhovic et al. “Further advances in simulating the processing of composite materials by electromagnetic induction”. In: *Engineering Journal* 3.6 (June 2014), pp. 34–50.

[44] R.S. Ruffini et al. “Enhancing induction heating processes by applying magnetic flux controllers”. In: *Heat treating: proceedings of the 19th conference* (Nov. 1999), pp. 162–167.

[45] V.S. Nemkov and R.C. Goldstein. “Practical use of computer simulation for advanced induction coil and process design”. In: *Proceedings of the 25th ASM heat treating society conference* (June 2000), pp. 65–74.

[46] Nemkov V. “Magnetic Flux Control in Induction Installations”. In: *Proc. of the Int. Symp. HES13, Heating by Electromagnetic Sources, Padua, Italy*. 2013.

[47] R.C. Goldstein, V. Nemkov, and J. Jackowski. “Virtual prototyping of induction heat treating”. In: *Proceedings of the 25th ASM heat treating society conference* (Sept. 2009), pp. 86–90.

[48] F. Li, X. Li, and Y.K. Rong. “Numerical simulation of the moving induction heating process with magnetic flux concentrator”. In: *Advances in Mechanical Engineering* 5 (2013). 907295.

[49] V Rudnev, D Loveless, and R Cook. *Handbook of induction heating*. 2002.

[50] P. Mitschang, M. Humbert, and L. Moser. “Susceptorless continuous induction welding of carbon fiber reinforced thermoplastics”. In: *The 19th international conference on composite materials* (July 2013).

[51] I. Çaldichoury et al. “LS-DYNA R7: Coupled Multiphysics analysis involving Electromagnetism (EM), Incompressible CFD (ICFD) and solid mechanics thermal solver for conjugate heat transfer problem solving”. In: *Proceedings of the 9th European LS-DYNA users conference* (2013).

[52] W. Lin, O Buneman, and A.K. Miller. “Induction heating model for graphite fiber/thermoplastic matrix composites”. In: *SAMPE Journal* 27.6 (1991), pp. 45–51.

[53] A.k. Miller et al. In: *SAMPE Journal* 26.4 (1990), pp. 37–54.

[54] W. Lin, A.K. Miller, and O. Buneman. In: *24th International SAMPE technical conference* 24.606 (1992).

[55] B.K. Fink, R.L. McCullough, and J.W. Gillespie. “A local theory of heating in cross-ply carbon fiber thermoplastic composites by magnetic induction”. In: *Polymer engineering and science* 32.5 (Mar. 1992), pp. 357–369.

[56] B.K. Fink, R.L. McCullough, and J.W. Gillespie. “Induction heating of carbon-fiber composites: electrical potential distribution model”. In: *ARMY RESEARCH LAB ABERDEEN PROVING GROUND MD* (Nov. 1991).

[57] B.K. Fink, R.L. McCullough, and J.W. Gillespie. “Induction heating of composites: thermal generation model”. In: *ARMY RESEARCH LAB ABERDEEN PROVING GROUND MD* (Sept. 2000).

[58] B.K. Fink, R.L. McCullough, and J.W. Gillespie. “Experimental verification of models for induction heating of continuous-carbon-fiber composites”. In: *Polymer composites* 17.2 (Apr. 1996), pp. 198–209.

[59] B.K. Fink, R.L. McCullough, and J.W. Gillespie. “A model to predict the through-thickness distribution of heat generation in cross-ply carbon-fiber composites subject to alternating magnetic fields”. In: *Composites Science and Technology* 55 (1995), pp. 119–130.

[60] Y. Wan et al. “Advanced Measurement, Characterization and Simulation of Thermoplastic Composite Induction Welding”. In: *KMUTNB: International Journal of Applied Science and Technology* 7.4 (2014), pp. 1–12. ISSN: 1906-151X. URL: http://ojs.kmutnb.ac.th/index.php/ijst/article/view/293.

[61] F. Lionetto et al. “Finite element modeling of continuous induction welding of thermoplastic matrix composites”. In: *Materials & Design* 120 (2017), pp. 212–221. ISSN: 0264-1275. DOI: 10.1016/j.matdes.2017.02.024.

[62] P. Mitschang and D. Maurer. “Quality Controlled Induction Welding by Adapted Process Parameters”. In: *SAMPE Journal* 53.1 (2017), pp. 42–50.

[63] T. Spahr. *Arkema innovative chemistry - KEPSTAN PEKK Polymer*. Technical presentation. Oct. 2015.

[64] M.H. Salek. “Effect of processing parameters on the mechanical properties of Carbon/PEKK thermoplastic composite materials”. MA thesis. Concordia University, Apr. 2005.

[65] Gharda chemicals limited. *PEKK (Polyether Ketone Ketone)*. Product specification-provisional.

[66] Cytec. *PEKK Thermoplastic polymer*. Technical Datasheet.

[67] TenCate. *TenCate Cetex TC1320 PEKK Thermoplastic Resin system*. Product Dataheet. Apr. 2015.

[68] J. Pan et al. “Dielectric characteristics of poly(ether ketone ketone) for high temperature capacitive energy storage”. In: *Applied Physics Letters* 95.022902 (2009), pp. 11–14.

[69] Kepstan Arkema. *Technical data - 7000 series*. Technical data sheet.

[70] R.L. Mazur et al. “Environmental effects on viscoelastic behavior of carbon fibre/PEKK thermoplastic composites”. In: *Journal of reinforced plastics and composites* 0.00 (2013), pp. 1–9.

[71] Cytec. *APC-2-PEEK Thermoplastic polymer*. Technical Datasheet.

[72] Ticona. *Fortron PPS glass reinforced*. Technical Datasheet. Jan. 2007.

[73] K.P. Menard. *Dynamic mechanical analysis: a practical introduction*. CRC press, 2008. ISBN: 0-8493-8688-8.

[74] C L Choy et al. "Thermal Conductivity of Poly ( ether Ether Ketone ) and Its Short-Fiber Composites". In: *Journal of polymer science part B: Polymer physics* 32.8 (1994), pp. 1389–1397.

[75] ASTM International. *Standard test method for determining specific heat capacity by differential scanning calorimetry*. ASTM Standard. E1269-11.

[76] O. Schieler. "Optimized induction welding process for the efficient manufacturing of TPC aerospace parts". In: *Sciety for the advancement of material and process engineering* (2014).

[77] ANSYS. *Solid state induction heating equipment*. 9th ed. Ambrell operation and maintenance instructions. 2007.

[78] Keithley. *Model 2701 Ethernet-Based DMM/ Data Acquisition System*. User's Manual. Tektronix. Aug. 2011.

[79] FLIR Research and Science. *FLIR A655sc High-Resolution Science Grade LWIR Camera*. http://www.flir.com/science/display/?id=46802. [Online; Visited: 23-06-17].

[80] Struers. *Secotom-10*. http://www.struers.com/en-GB/Products/Cutting/Cutting-equipment/Secotom. [Online; Visited 19-06-17].

[81] F. Lundström et al. "Induction heating of carbon fiber composites: Investigation of electrical and thermal properties". In: *International Journal of Applied Electromagnetics and Mechanics* 53 (2017), pp. 21–30. DOI: 10.3233/JAE-162235.

[82] A. Todoroki, M. Tanaka, and Y. Shimamura. "Measurement of orthotropic electric conductance of CFRP laminates and analysis of the effect on delamination monitoring with an electric resistance change method". In: *Composites Science and technology* 62 (2002), pp. 619–628.

[83] D. Stavrov and H.E.N. Bersee. *Induction Welding of Thermoplastic Composites*. Tech. rep. Internal report KVE, pp. 1–31.

[84] H. Menana and M. Féliachi. "3-D Eddy current computation in carbon-fiber reinforced composites". In: *IEEE Transactions on magnetics* 45.3 (Mar. 2009), pp. 1008–1011.

[85] R. Schueler, S.P. Joshi, and K. Schulte. "Damage detection in CFRP by electrical conductivity mapping". In: *Composites Science and Technology* 61 (2001), pp. 921–930.

[86] K.J. Lodge. "The electrical properties of joints in carbon fibre composites". In: 07 (1982), pp. 305–310.

[87] J. Cheng et al. "Novel electromagnetic modeling approach of carbon fiber-reinforced polymer laminate for calculation of eddy currents and eddy current testing signals". In: *Journal of composite materials* 0.0 (2014), pp. 1–15.

[88] X. Wang and D.D.L. Chung. "Sensing delamination in a carbon fiber polymer- matrix composite during fatigue by electrical resistance measurement". In: *Polymer composites* 18.6 (1997), pp. 692–700.

[89] X. Wang and D.D.L. Chung. "An electromechanical study of the transverse behavior of carbon fiber polymer-matrix composite". In: *Composite interfaces* 5.3 (1997), pp. 191–199. DOI: 10.1163/156855498X00144.

[90] J.C. Abry et al. "In situ detection of damage in CFRP laminates by electrical resistance measurements". In: *Composites Science and Technology* 59.6 (1999), pp. 925–935.

[91] K. Takahashi and H.T. Hahn. "Investigation of temperature dependency of electrical resistance changes for structural management of graphite / polymer composite". In: 45.25 (2011), pp. 2603–2611. DOI: 10.1177/0021998311416683.

[92] B.K. Fink, R.L. McCullough, and J.W. Gillespie. "Induction heating of carbon-fiber composites: electrical potential distribution model". In: *ARMY RESEARCH LAB ABERDEEN PROVING GROUND MD* (Nov. 1999).

[93] Comsol. *COMSOL Multiphysics Release notes 5.2*. Comsol 5.2. 2015.

[94] W. Frei. *Solutions to Linear Systems of Equations: Direct and Iterative Solvers*. https://www.comsol.com/blogs/solutions-linear-systems-equations-direct-iterative-solvers/. 2013.

[95] ANSYS. *ANSYS Mechanical APDL Coupled-Field Analysis Guide*. 11th ed. ANSYS. 2010.

[96] ANSYS. “Electromagnetics”. In: *ANSYS Mechanical APDL Theory reference*. Vol. 15. 2013, pp. 177–226.

# Appendices

# A

# GRADUATION ASSIGNMENT

*PROJECT NOTE*

| | | | |
|---|---|---|---|
| To | KVE R&D | Written by | Maarten Labordus |
| Description | Afstudeeropdracht Bas de Wit | Date | 1 juni 2016 |
| Project code | K-KV63 | Reference | K-KV63-042PN-ML |
| Cc | Matthijs Bosboom | | |

**Achtergrond & probleemstelling**

KVE Composite Structures BV heeft een lasproces ontwikkeld voor koolstofvezelversterkte thermoplast composieten op basis van inductie. Hierbij worden met een inductiespoel wervelstromen opgewekt in de koolstofvezels, waarmee warmte wordt gegenereerd die de matrix laat smelten. Als twee onderdelen daarbij op elkaar worden geklemd, kan na afkoeling een structurele verbinding worden gemaakt. Dit proces wordt met name toegepast in de vliegtuigbouw bij het assembleren van stuurvlakken en accesspanels. Fokker heeft het KVE las-proces in licentie bij het lassen van stuurvlakken voor het G650 programma.

Het lasproces voor het lassen van koolstof-weefsel-versterkt PPS is op dit moment goed ontwikkeld. Ook zijn er FEM-simulaties die een goede voorspellende waarde hebben. Voor toekomstige programma's wordt gekeken naar UD-koolstof tapes met een PEKK matrix. Voor laminaten op basis van dit materiaal werken de FEM-simulaties nog niet voldoende goed. Deels heeft dit te maken met het feit dat de wervelstromen in een gelaagd ud-laminaat anders lopen dan in een weefsel, deels met de andere matrix, deels met het onvoldoende nauwkeurig kunnen meten van de benodigde materiaaleigenschappen.

**Projectdoelstelling**

Het ontwikkelen van FEM-simulaties van het inductie-lasproces voor toepassing op koolstof-UD-PEKK lamimaten.

**Input**

- Bestaande FEM-modellen van koolstof-weefsel-PPS laminaten.
- Conceptuele opzet meetopstelling.

**Activiteiten**

- Ontwikkelen meetmethode voor benodige (elektische) input voor FEM-modellen.
- Aanpassen FEM-modellen naar nieuwe materialen.
- Uitvoeren van diverse simulaties om specifieke las-opstellingen te optimaliseren.
- Praktische validatie van simulaties.
- Rapporteren.

**Output**

- Gevalideerde FEM-modellen
- Eindrapport

**Contactgegevens**

Maarten Labordus
Senior R&D Engineer

KOK & VAN ENGELEN
COMPOSITE STRUCTURES BV

Kok & Van Engelen Composite Structures BV
Laan van Ypenburg 56
2497 GB The Hague, The Netherlands
Tel +31 (0)70 - 307 47 10
Fax +31 (0)70 - 307 47 11
Email Labordus@kve.nl
Website www.kve.nl

# B

# PROTH CUTTING AND GRINDING INSTRUCTIONS

The following appendix describes the tasks performed in order to get the samples used to measure the electric resistance of the Carbon Fibre (CF)-Poly(Ether-Ketone-Ketone) (PEKK) material. It is a work description set-up directly after instructions were received from Fred Bosch.

## B.1. PREPARING PROTH MACHINE

- Turn on the water filter in the other room. Clean the roster afterwards.
- Take the square bottom plate and two nuts to assemble in the Proth machine.
- Clean the bottom plate and the base of the Proth machine. Everything should be as level as possible.
- Position the bottom plate at the centre of the Proth machine and make sure the holes for the nuts are aligned.
- Tighten the nuts while making sure that the bottom plate stays centred.

In order to not damage the bottom plate, a separate PVC plate is used on which the laminate will be attached.

## B.2. PLACING THE PVC PLATE

- Grab the double sided tape, Stanley knife, some paper and ethanol.
- clean the PVC plate with ethanol and the piece of paper. This is to clean the surface before applying the tape.
- Apply the double sided tape, perpendicular to the direction the cutting blade will go.
- Make sure the double sided tape is not double at any location. The plate should be flat.
- Clean the other side of the PVC plate as well, the composite will be attached to this side.
- Measure the thickness of the composite. This will be as an input to the Proth cutting machine.
- Clean the laminate with ethanol and apply the double sided tape to your laminate. Tape should be at the locations where the blade will cut the laminate.
- Remove the paper from the double sided tape and attach the laminate to the PVC plate.

## B.3. PROTH PROGRAM

The settings used for cutting the samples is given in Figure B.1.

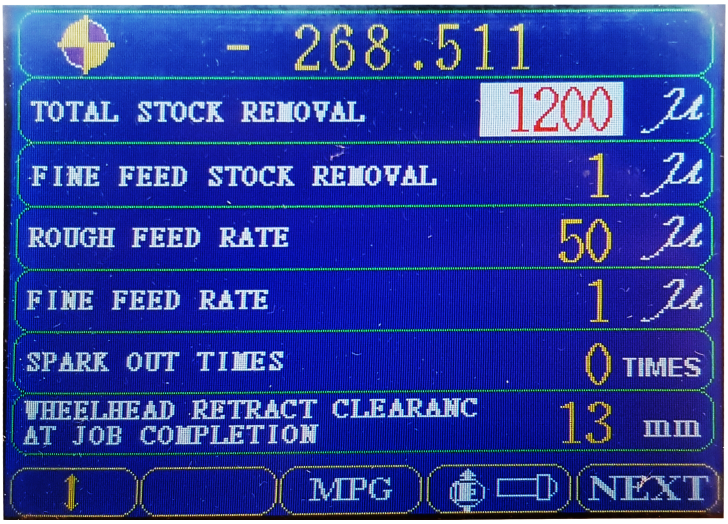


Figure B.1: Proth cutting machine settings

The total stock removal is the movement of the diamond blade saw in thickness direction. This equals the thickness of the laminate with a margin of 0.1 [mm]. The rough feed rate is set to 50 [$\mu$m]. This indicates the step size taken in thickness direction by the diamond blade saw.

# C
# MICROSCOPY TASK DESCRIPTION

The following appendix describes the tasks performed in order to get the microscopic images from this research. It is a work description set-up directly after instructions were received from Frans Oostrum.

## C.1. CREATING THE SAMPLES

- Use paint marker to draw the samples on the laminate one wants to visualise with the microscope. The samples shall not be longer than 1.5 [cm] and not wider than 2 [cm].
- Grab the tool box and the diamond blade saw from Frans' office and go to the cutting room.
- Put on safety goggles.
- Open the lid and grab the appropriate tools to install the blade.
- Install the blade and ensure that the blade is correctly installed (no visible wobble).
- Close the lid of the secotom-10.
- Turn on the machine. The button is located at the back of the machine.
- Set the machine to 3000 [rpm], 0.005 [mm/s] feed speed and 61 [mm] cut length. These settings dictate the movement of the platform inside the Secotom, which is not used. With a minimal feed speed and maximum cut length, the machine will stay on for a maximum duration.
- Cut the samples to size.
- Clean the machine.
- Open the lid and remove the blade.
- Clean the inside of the machine and leave the lid open to air the Secotom.
- Clean the samples with the ultrasonic ethanol bath. Place the samples in the basket, turn the button to infinite and clean for 10 [s]. Dry the samples with the help of compressed air.

## C.2. MAKING THE PLASTIC HOLDERS

- Take the box containing all materials to manufacture the plastic holder. The box is located in the cabinet in front of Frans' office.
- Go to the cutting room.
- Take the double sided tape and remove the paper covers
- Attach all the samples to each other (upside down), having the stickers as high as possible and the bottom sides of the samples aligned.
- Place the samples in the plastic holders.
- Create the thermoset plastic by mixing 1 scoop of liquid with 2 scoops of powder inside of a plastic container with a wooden stirrer. All the powder should dissolve. The plastic will gell within 5 minutes.
- After mixing the constituents, tab the plastic container on the table to remove any air bubbles from the polymer.

- Poor the polymer liquid into the plastic holders containing the samples, guided with the help of a wooden stirrer.
- Pour the liquid into one side of the sample holder until it comes out of the other side. This limits the amount of air bubbles inside the polymer.
- The plastic that is left over can be tested to see if it is hardened.
- Take the hardened plastic containing the samples from the plastic holder.

## C.3. SANDING AND POLISHING

- Take the specimen and sand with the Struers Pedemin Dap-7.
- Begin with a coarse sanding paper p180, this is to remove any plastic covering the sample's edges.
- Remove the spatter and holder rings. Place the sanding paper and put the rings back.
- Turn on the water to cool and lubricate the sanding process.
- Set the machine to 125 [rpm].
- Sand the samples by pressing them onto the sanding paper until the edges are free.
- When the edges are free, replace the sanding paper for a size p320. Turn on the water and sand for 1 minute in total.
- Replace the sanding paper for a size p1000. Turn on the water and sand for 1 minute.
- Replace the sanding paper for a size p2400. Turn on the water and sand for 1 minute.
- Remove the sanding paper block holder and the rings. Dry the spatter ring.
- Place the polishing block with grain size 6 [$\mu m$] (cabinet 1 above bottom drawer).
- Clean the samples in the ethanol bath and dry with compressed air.
- Place the samples in the holder (which is placed above the polishing block). Place the holder until the button on top clicks in.
- Wet the samples and polishing block with Ethanol. Never use water when polishing!
- Set the force of the holder to 15 [N], by turning the wheels above the samples towards the correct location. Each bar represents 5 [N].
- Turn on both machines and polish for 1 minute while keeping wet with ethanol.
- Clean the samples in the ethanol bath and dry with compressed air.
- Replace the polishing block for the 3 [$\mu m$] size (middle drawer) and repeat previous steps.
- Replace the polishing block for the 1 [$\mu m$] size (top drawer) and repeat previous steps.
- Remove the samples and clean with the ethanol bath and dry with compressed air.
- Make sure the liquid is cleared from the cracks.
- Remove the polishing block, never let is touch with water!
- Clean the polishing machine.
- Do not touch the outer sides of the samples, to prevent contamination.

## C.4. MICROSCOPE

- Log onto the computer.
- Turn on the microscope with the button on the left.
- Take the metal plate from the microscope, the hand press, a piece of cleaning gum and a piece of paper.
- Stick the the sample to the metal holder with the gum. Place the piece of paper on top of the samples and press the sample and metal holder together with the help of the hand press.
- Extract the filters of the microscope.
- Start the program Axiovision rel. 4.6.
- Press 'Workflow' and 'Live'.
- Use the coarse and fine adjustment knobs to sharpen the image.
- The two levers on the right back side of the microscope, can be used to limit the amount of light.
- To save images, press 'Snap'. The snap is located below the live window. Use F7 and F8 to zoom in and out. Attach the measuring bar and press save. Do not forget to set the scaling in the live image for correct scaling.

# D

# DIMENSIONS WOODEN PLATFORM

A wooden platform was manufactured on which the laminates reside during induction heating. The dimensions of the platform are included in Figure D.1. The units are in millimetres.

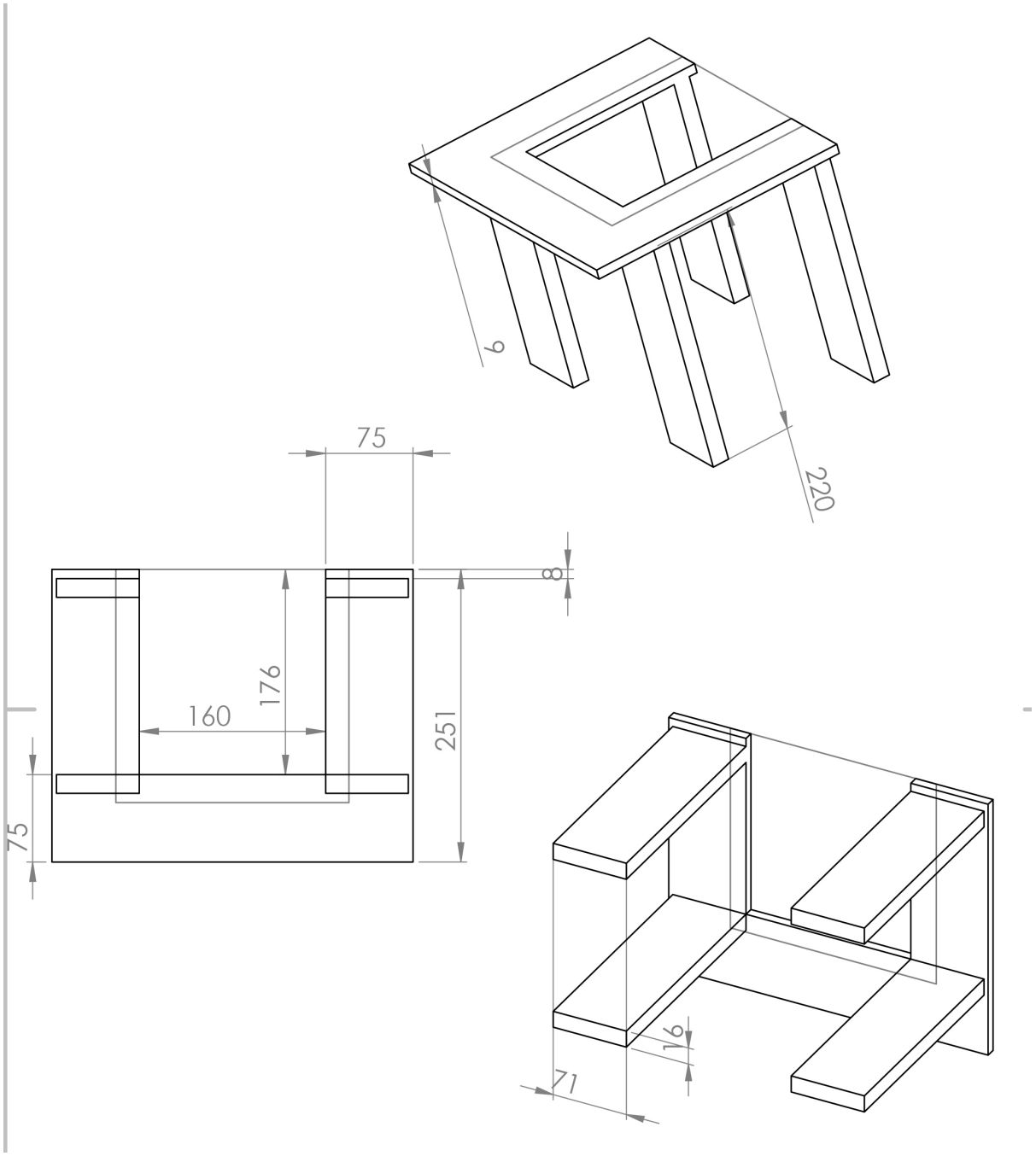


Figure D.1: Dimensions wooden platform

# E

# DIMENSIONS HELMHOLTZ AND HAIRPIN COILS

The current appendix gives the dimensions of the Helmholtz and Hairpin coils used to model the induction heating of the Carbon Fibre (CF)-Poly(Ether-Ketone-Ketone) (PEKK) laminates. Figures E.1, E.2 and E.3 give the top-, front- and side view of the Helmholtz coil. The copper tubing of the Helmholtz coil has a diameter of 4.8 [mm]. Figure E.4 shows the top view of the Hairpin coil. The tubing of the Hairpin coil has a diameter of 6.0 [mm].

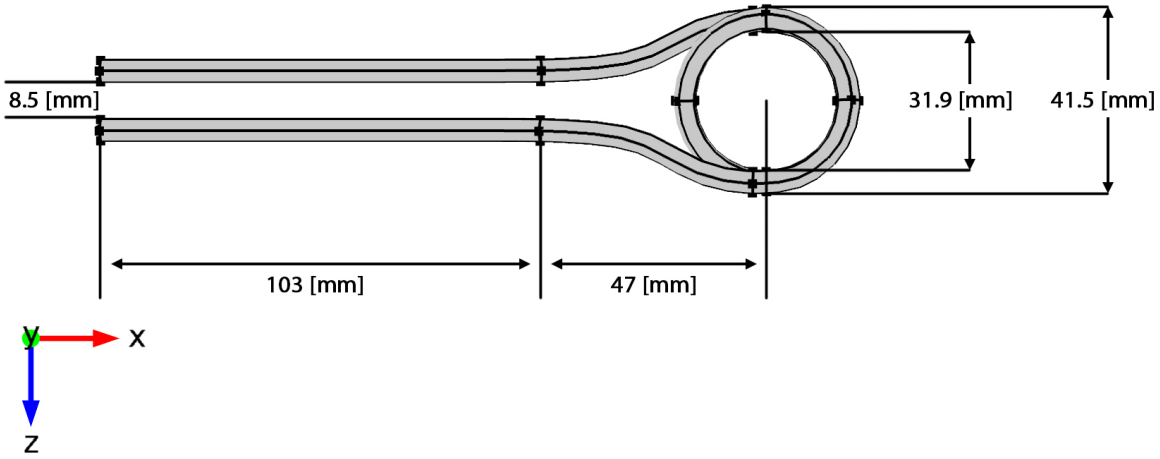


Figure E.1: Top view of the Helmholtz coil

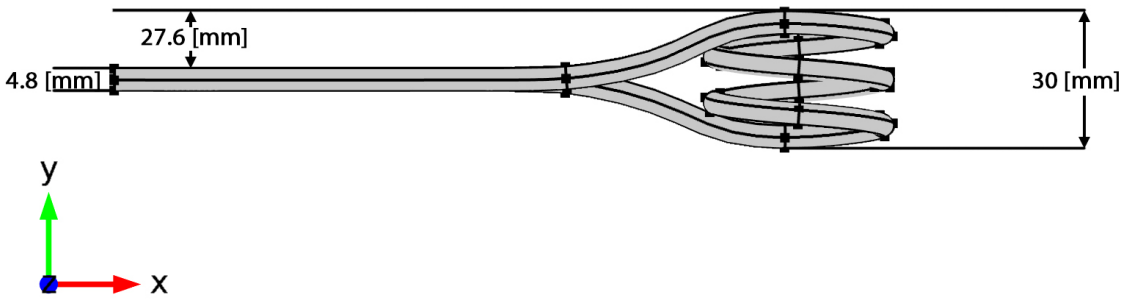


Figure E.2: Front view of the Helmholtz coil

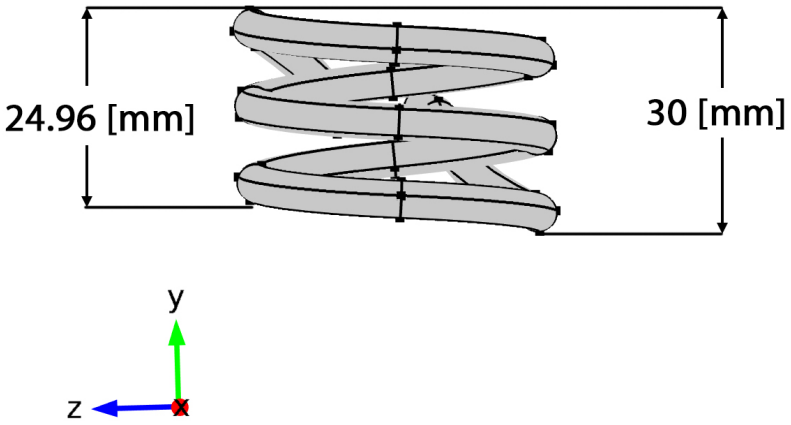


Figure E.3: Side view of the Helmholtz coil

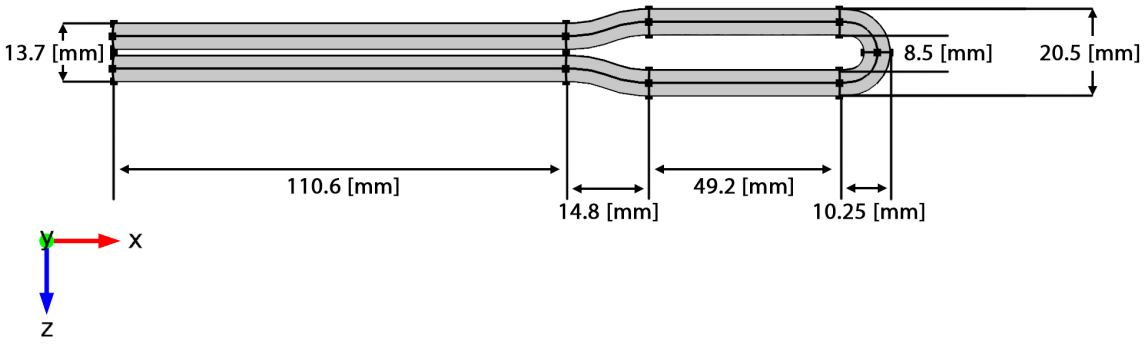


Figure E.4: Top view of the Hairpin coil

# F

# HAIRPIN HEATING PATTERN RESULTS

Figures F.1, F.2 and F.3 show the heating patterns predicted by the Comsol models for the Hairpin coil. All show an agreement with the experimental results confirming that Comsol is able to predict heating of the UD CF-PEKK laminates.

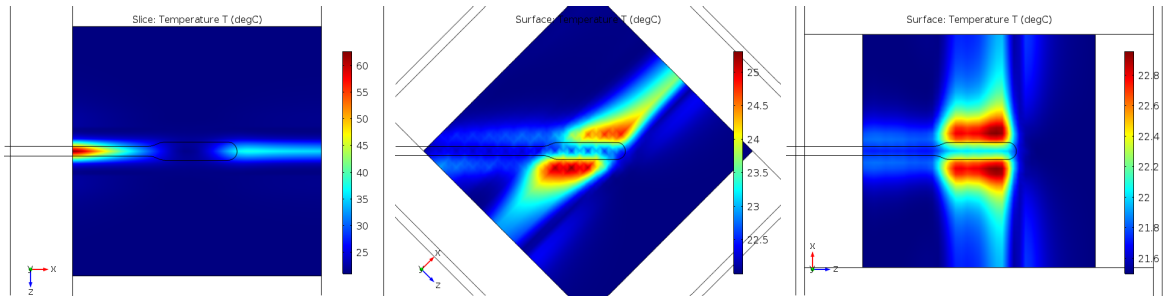


(a) $\alpha = 0[deg]$ (b) $\alpha = 45[deg]$ (c) $\alpha = 90[deg]$

Figure F.1: Heating pattern $[0]_{4S}$ laminate, Hairpin coil, 400 [A] at t = 15 [s]

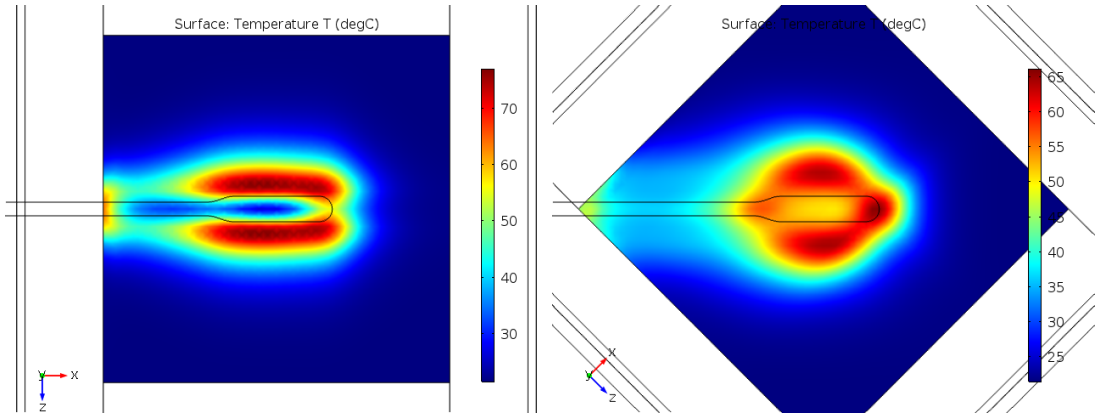


(a) $\alpha = 0[deg]$ (b) $\alpha = 45[deg]$

Figure F.2: Heating pattern $[0,90]_{4S}$ laminate, Hairpin coil, 150 [A] at t = 15 [s]

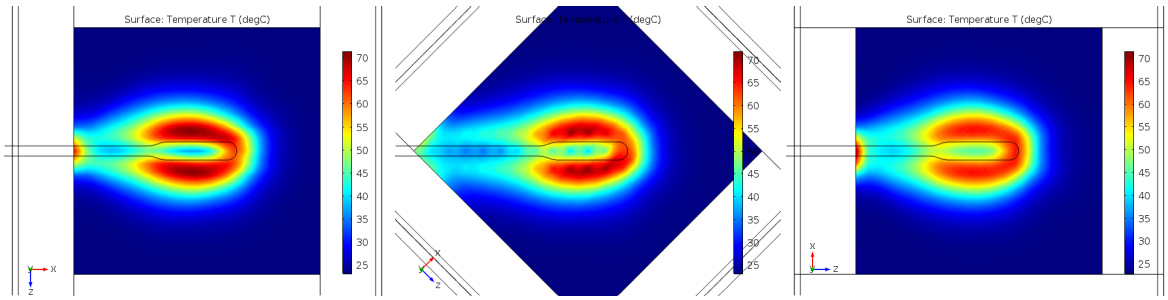


(a) $\alpha = 0[deg]$ (b) $\alpha = 45[deg]$ (c) $\alpha = 90[deg]$

Figure F.3: Heating pattern $[45,-45,0,90]_S$ laminate, Hairpin coil, 150 [A] at t = 15 [s]

# G
# RESISTANCE MEASUREMENTS

The raw data used for the final material resistance measurements are included in this appendix.

## G.1. ELECTRIC RESISTIVITY FIBRE DIRECTION $[0]_{4S}$ SAMPLES

With a rectangular shaped sample, there are a total of four possible ways to place the sample in between the copper terminals of the electric resistance measurement set-up. Figure G.1 shows the sample, and the rotations used to achieve the four different placement orientations. The origin of the coordinate system in this case is in the centre of the sample.

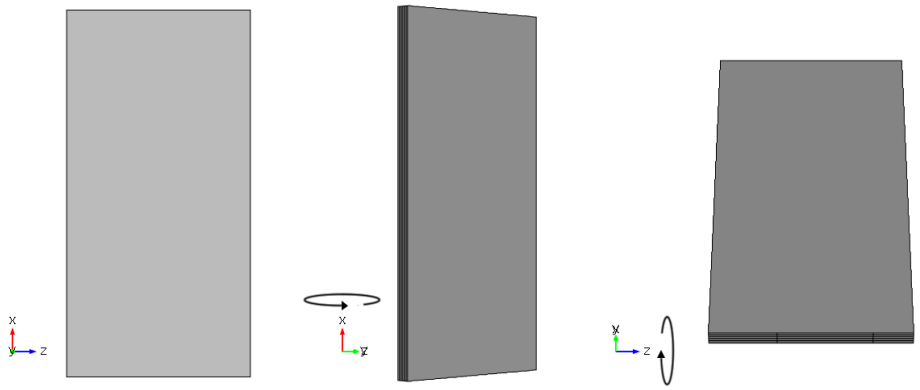

Figure G.1: Sample rotation axes

With position one being the starting position of the sample, the second position is achieved by rotating the sample $\pi$ [rad] along the x-axis (first rotation). The third position is achieved by starting from position two and rotating the sample $\pi$ [rad] along the z-axis of the sample. The final and fourth position is achieved by starting from position three and rotating the sample $\pi$ [rad] again along the x-axis of the sample. The positioning of the sample and its influence on the resistances measured is investigated for the resistance sample produced from the $[0]_{4S}$ laminate and measured in fibre direction. The results are given in Table G.1. The dimensions of the samples are included in Table G.4. The mass placed on top equalled 5 [kg], based on the findings of Table G.2.

Table G.1: Influence positioning sample on electric resistance $[0]_{4S}$ sample with 5 [kg] of mass placed on top

| | Positioning | | | |
|---|---|---|---|---|
| | 1 | 2 | 3 | 4 |
| Resistance sample 1 [Ω] | 0.12 | 0.22 | 0.26 | 0.16 |
| Resistance sample 2 [Ω] | 0.48 | 0.14 | 0.10 | 0.39 |
| Resistance sample 3 [Ω] | 0.09 | 0.18 | 0.17 | 0.09 |
| Resistance sample 4 [Ω] | 0.22 | 0.12 | 0.13 | 0.13 |
| Resistance sample 5 [Ω] | 0.14 | 0.26 | 0.26 | 0.15 |
| Resistance sample 6 [Ω] | 0.27 | 0.16 | 0.10 | 0.24 |

With the influence of the positioning of the sample known, the influence of the amount of mass placed on top of the electric resistance measurement set-up was also investigated. Table G.2 shows the results for the six different samples. The samples are positioned to have the best fit with the copper terminals.

Table G.2: Influence weight on resistance measurement

| | Mass placed on top [kg] | | | | | |
|---|---|---|---|---|---|---|
| | 0 | 1 | 2 | 3 | 4 | 5 |
| Resistance sample 1 [Ω] | 0.33 | 0.25 | 0.20 | 0.18 | 0.17 | 0.16 |
| Resistance sample 2 [Ω] | 0.24 | 0.20 | 0.17 | 0.16 | 0.15 | 0.15 |
| Resistance sample 3 [Ω] | 0.21 | 0.18 | 0.18 | 0.16 | 0.14 | 0.13 |
| Resistance sample 4 [Ω] | 0.23 | 0.18 | 0.17 | 0.15 | 0.15 | 0.15 |
| Resistance sample 5 [Ω] | 0.25 | 0.23 | 0.21 | 0.21 | 0.20 | 0.20 |
| Resistance sample 6 [Ω] | 0.56 | 0.38 | 0.29 | 0.23 | 0.21 | 0.19 |

The evaluation of the heating images obtained by using the thermal camera are included in Table G.3. The units are in inches and are measured using the ruler system of Photoshop. Because only the relative positions are of importance, the coordinate system used is not explained.

Table G.3: Evaluation heating images $[0]_{4S}$ samples in longitudinal resistivity measurements

| | | Photoshop evaluation | | | |
|---|---|---|---|---|---|
| Sample | Side | Left side sample [in] | Left side current [in] | Right side current [in] | Right side sample [in] |
| 1 | 1 | 3.415 | 3.831 | 5.039 | 6.142 |
| | 2 | 3.393 | 4.747 | 6.038 | 6.121 |
| 2 | 1 | 3.415 | 5.039 | 6.080 | 6.121 |
| | 2 | 3.539 | 4.227 | 5.788 | 6.142 |
| 3 | 1 | 3.456 | 4.060 | 6.142 | 6.538 |
| | 2 | 3.456 | 3.852 | 6.080 | 6.080 |
| 4 | 1 | 3.440 | 5.015 | 6.020 | 6.239 |
| | 2 | 4.122 | 5.122 | 6.892 | 6.892 |
| 5 | 1 | 3.748 | 5.461 | 6.385 | 6.385 |
| | 2 | 3.687 | 3.790 | 4.605 | 6.364 |
| 6 | 1 | 3.581 | 3.789 | 5.205 | 6.309 |
| | 2 | 3.706 | 5.288 | 6.371 | 6.454 |

The values of Table G.3 are used to compute the effective width of the current going through the sample. The dimensions, resistance measurements and conductivity computation is included in Table G.4.

Table G.4: Results $[0]_{4S}$ samples resistivity and conductivity computation longitudinal direction

| | | Dimensions sample | | | | | | |
|---|---|---|---|---|---|---|---|---|
| Sample | Side | Width [mm] | Length [mm] | Thickness [mm] | Width Current [mm] | Resistance [Ω] | Resistivity [$\Omega \cdot m$] | Conductivity [S/m] |
| 1 | 1 | 14.93 | 29.8 | 1.10 | 6.613656 | 0.25 | 6.10321E-05 | 16384.83 |
| | 2 | 14.93 | 29.8 | 1.10 | 7.06548 | 0.19 | 4.95532E-05 | 20180.33 |
| 2 | 1 | 14.96 | 29.8 | 1.09 | 5.755122 | 0.20 | 5.1995E-05 | 19232.61 |
| | 2 | 14.96 | 29.8 | 1.09 | 8.971402 | 0.18 | 5.90667E-05 | 16930 |
| 3 | 1 | 14.93 | 29.79 | 1.10 | 10.08574 | 0.21 | 7.63456E-05 | 13098.33 |
| | 2 | 14.93 | 29.79 | 1.10 | 12.67684 | 0.09 | 4.40009E-05 | 22726.83 |
| 4 | 1 | 14.97 | 29.78 | 1.10 | 5.37508 | 0.40 | 7.86227E-05 | 12718.97 |
| | 2 | 14.97 | 29.78 | 1.10 | 9.565668 | 0.18 | 6.35998E-05 | 15723.32 |
| 5 | 1 | 15.00 | 29.77 | 1.10 | 5.255973 | 0.25 | 4.77751E-05 | 20931.38 |
| | 2 | 15.00 | 29.77 | 1.10 | 4.566679 | 0.26 | 4.35345E-05 | 22970.26 |
| 6 | 1 | 14.95 | 29.86 | 1.12 | 7.759971 | 0.19 | 5.472E-05 | 18274.85 |
| | 2 | 14.95 | 29.86 | 1.12 | 5.891867 | 0.24 | 5.34806E-05 | 18698.36 |
| | | | | | | **Average** | **5.7E-05** | **18.2E03** |
| | | | | | | **Standard deviation** | **1.1E-05** | **3.3E3** |

## G.2. ELECTRIC RESISTIVITY TRANSVERSE TO FIBRE DIRECTION $[0]_{4S}$ SAMPLES

A total of ten samples were produced in order to measure the electric resistivity perpendicular to the fibre direction. The influence of positioning the samples on the electric resistance measured was also investigated for these samples. Table G.5 gives the results, measured with approximately 5 [kg] of mass placed on top of the measurement set-up. The different positions are achieved by applying the same rotations performed for the longitudinal samples, based on the rotations of Figure G.1.

Table G.5: Influence positioning sample on electric resistance $[90]_{4S}$ sample with 5 [kg] of mass placed on top

| | Positioning | | | |
|---|---|---|---|---|
| | 1 | 2 | 3 | 4 |
| Resistance sample 1 [Ω] | 150.6 | 150.5 | 150.4 | 150.5 |
| Resistance sample 2 [Ω] | 152.4 | 152.4 | 152.4 | 152.4 |
| Resistance sample 3 [Ω] | 146.7 | 146.7 | 146.7 | 146.7 |
| Resistance sample 4 [Ω] | 136.5 | 136.6 | 136.6 | 136.6 |
| Resistance sample 5 [Ω] | 142.9 | 142.9 | 142.9 | 142.9 |
| Resistance sample 6 [Ω] | 147.9 | 148.0 | 148.0 | 147.9 |
| Resistance sample 7 [Ω] | 150.9 | 150.3 | 150.3 | 150.8 |
| Resistance sample 8 [Ω] | 149.4 | 149.2 | 149.2 | 149.4 |
| Resistance sample 9 [Ω] | 149.2 | 149.0 | 149.0 | 149.2 |
| Resistance sample 10 [Ω] | 134.6 | 134.4 | 134.4 | 134.5 |

Table G.5 shows how the positioning of the samples has little to no influence on the resistance measured. The influence of the weight on the resistance measured for $[90]_{4S}$ samples is given in G.6.

Table G.6: Influence weight on resistance measurement

| | Mass placed on top [kg] | | | | | |
|---|---|---|---|---|---|---|
| | 0 | 1 | 2 | 3 | 4 | 5 |
| Resistance sample 1 [Ω] | 151.9 | 151.4 | 151.0 | 150.4 | 150.3 | 150.3 |
| Resistance sample 2 [Ω] | 153.7 | 153.5 | 153.3 | 153.2 | 153.1 | 153.0 |
| Resistance sample 3 [Ω] | 147.7 | 147.5 | 147.4 | 147.3 | 147.3 | 147.3 |
| Resistance sample 4 [Ω] | 137.5 | 137.4 | 137.3 | 137.2 | 137.1 | 137.1 |
| Resistance sample 5 [Ω] | 143.7 | 143.6 | 143.5 | 143.4 | 143.4 | 143.4 |
| Resistance sample 6 [Ω] | 149.3 | 149.0 | 148.7 | 148.6 | 148.5 | 148.5 |
| Resistance sample 7 [Ω] | 151.9 | 151.7 | 151.1 | 151.0 | 151.0 | 151.0 |
| Resistance sample 8 [Ω] | 150.2 | 150.0 | 149.9 | 149.9 | 149.9 | 149.9 |
| Resistance sample 9 [Ω] | 150.1 | 150.1 | 150.0 | 149.9 | 149.8 | 149.8 |
| Resistance sample 10 [Ω] | 136.0 | 135.6 | 135.4 | 135.2 | 135.1 | 135.1 |

Table G.6 shows how the weight has much less of an influence on the resistance results due to the increased resistances measured. The results for the computation of the conductivity of the Carbon Fibre (CF)-Poly(Ether-Ketone-Ketone) (PEKK) material transverse to the fibre direction is given in Table G.7 and equals approximately 12.6 [S/m] at room temperature.

Table G.7: Results $[90]_{4S}$ samples resistivity and conductivity computation

| | Dimensions sample | | | | | |
|---|---|---|---|---|---|---|
| Sample | Width [mm] | Length [mm] | Thickness [mm] | Resistance [Ω] | Resistivity [$\Omega \cdot m$] | Conductivity [S/m] |
| 1 | 14.90 | 29.82 | 1.10 | 150.4 | 0.08266 | 12.09709 |
| 2 | 14.89 | 29.83 | 1.09 | 152.4 | 0.08292 | 12.05999 |
| 3 | 14.92 | 29.83 | 1.09 | 146.7 | 0.07998 | 12.50339 |
| 4 | 14.90 | 29.78 | 1.07 | 136.5 | 0.07308 | 13.68428 |
| 5 | 14.92 | 29.84 | 1.08 | 142.9 | 0.07717 | 12.95908 |
| 6 | 14.92 | 29.84 | 1.11 | 147.9 | 0.08208 | 12.18257 |
| 7 | 14.86 | 29.79 | 1.07 | 150.3 | 0.08022 | 12.46548 |
| 8 | 14.91 | 29.89 | 1.12 | 149.2 | 0.08336 | 11.99669 |
| 9 | 14.90 | 29.86 | 1.11 | 149.0 | 0.08253 | 12.11698 |
| 10 | 14.92 | 29.88 | 1.08 | 134.4 | 0.07248 | 13.79713 |
| | | | | **Average** | **0.0797** | **12.6** |
| | | | | **Standard deviation** | **0.004** | **0.67** |

## G.3. ELECTRIC RESISTIVITY THROUGH-THICKNESS DIRECTION $[0]_{4S}$, $[0,90]_{2S}$, $[45,-45,0,90]_S$ AND $[45,-45,0,90]_{2S}$ SAMPLES

Through-thickness measurements were performed on all of the different lay-ups, in order to compute the different contact resistivities and the volume resistivity of the material. The influence of positioning the samples on the electric resistance measured was also investigated for these samples. Tables G.8 and G.9 show the influence of the position of the sample on the resistance measured. The minimum resistance is used to compute the through thickness conductivity of the lay-ups.

Table G.8: Influence positioning sample on electric through-thickness resistance $[0]_{4S}$ sample with 5 [kg] of mass placed on top

| | Positioning $[0]_{4S}$ samples | |
|---|---|---|
| | 1 | 2 |
| Resistance sample 1 [Ω] | 34.4 | 34.4 |
| Resistance sample 2 [Ω] | 33.4 | 33.3 |
| Resistance sample 3 [Ω] | 34.2 | 34.2 |
| Resistance sample 4 [Ω] | 28.8 | 28.9 |
| Resistance sample 5 [Ω] | 22.9 | 23.1 |
| Resistance sample 6 [Ω] | 30.9 | 31.0 |
| Resistance sample 7 [Ω] | 29.8 | 29.7 |
| Resistance sample 8 [Ω] | 26.8 | 26.8 |
| Resistance sample 9 [Ω] | 34.6 | 34.5 |
| Resistance sample 10 [Ω] | 32.8 | 32.8 |

Table G.9: Influence positioning sample on electric through-thickness resistance $[0,90]_{2S}$ sample with 5 [kg] of mass placed on top

| | Positioning $[0,90]_{2S}$ samples | |
|---|---|---|
| | 1 | 2 |
| Resistance sample 1 [Ω] | 36.7 | 36.7 |
| Resistance sample 2 [Ω] | 47.9 | 48.1 |
| Resistance sample 3 [Ω] | 39.9 | 40.0 |
| Resistance sample 4 [Ω] | 44.3 | 44.3 |
| Resistance sample 5 [Ω] | 64.6 | 64.6 |
| Resistance sample 6 [Ω] | 49.4 | 49.4 |
| Resistance sample 7 [Ω] | 37.1 | 37.2 |
| Resistance sample 8 [Ω] | 47.1 | 47.1 |
| Resistance sample 9 [Ω] | 44.0 | 43.9 |

Results show how the positioning of the samples has little to no influence on the resistances measured. The influence of the weight on the resistance measured for the $[0,90]_{2S}$ samples is given in G.10.

Table G.10: Influence weight on resistance measurement through-thickness $[0,90]_{2S}$ samples

| | Mass placed on top [kg] | | | | | |
|---|---|---|---|---|---|---|
| | 0 | 1 | 2 | 3 | 4 | 5 |
| Resistance sample 1 [Ω] | 37.5 | 37.4 | 37.4 | 37.4 | 37.4 | 37.4 |
| Resistance sample 2 [Ω] | 48.9 | 48.9 | 48.8 | 48.8 | 48.8 | 48.8 |
| Resistance sample 3 [Ω] | 40.8 | 40.7 | 40.7 | 40.7 | 40.7 | 40.7 |
| Resistance sample 4 [Ω] | 45.2 | 45.1 | 45.1 | 45.1 | 45.1 | 45.1 |
| Resistance sample 5 [Ω] | 66.0 | 66.0 | 66.0 | 66.0 | 65.9 | 65.9 |
| Resistance sample 6 [Ω] | 50.5 | 50.5 | 50.4 | 50.4 | 50.4 | 50.4 |
| Resistance sample 7 [Ω] | 37.9 | 37.9 | 37.9 | 37.9 | 37.8 | 37.8 |
| Resistance sample 8 [Ω] | 48.5 | 48.4 | 48.3 | 48.2 | 48.2 | 48.2 |
| Resistance sample 9 [Ω] | 44.9 | 44.8 | 44.8 | 44.7 | 44.7 | 44.7 |

Results show how the weight has almost no influence on the resistances measured. In order to find the different contact resistivities between plies, the through-thickness resistances of the $[45,\text{-}45,0,90]_S$ and $[45,\text{-}45,0,90]_{2S}$ samples have been measured. Tables G.11 and G.12 show both the influence of positioning and weight on the resistances measured.

Table G.11: Influence weight and position on resistance measurement through-thickness $[45,\text{-}45,0,90]_S$ samples

| | Mass placed on top [kg] | | | | | | |
|---|---|---|---|---|---|---|---|
| | Position 1 | | | | | | Position 2 |
| | 0 | 1 | 2 | 3 | 4 | 5 | 5 |
| Resistance sample 1 [Ω] | 80.9 | 80.7 | 80.7 | 80.6 | 80.6 | 80.6 | 80.2 |
| Resistance sample 2 [Ω] | 53.9 | 53.9 | 53.8 | 53.8 | 53.8 | 53.7 | 53.3 |
| Resistance sample 3 [Ω] | 47.1 | 47.1 | 47.1 | 47.0 | 47.0 | 47.0 | 47.4 |
| Resistance sample 4 [Ω] | 52.0 | 51.9 | 51.9 | 51.8 | 51.7 | 51.7 | 51.5 |
| Resistance sample 5 [Ω] | 56.5 | 56.5 | 56.4 | 56.4 | 56.3 | 56.3 | 56.5 |
| Resistance sample 6 [Ω] | 49.5 | 49.4 | 49.4 | 49.3 | 49.3 | 49.3 | 49.2 |
| Resistance sample 7 [Ω] | 47.8 | 47.8 | 47.7 | 47.6 | 47.6 | 47.6 | 47.5 |
| Resistance sample 8 [Ω] | 34.6 | 34.5 | 34.5 | 34.5 | 34.4 | 34.4 | 34.5 |
| Resistance sample 9 [Ω] | 51.6 | 51.5 | 51.5 | 51.4 | 51.4 | 51.3 | 51.1 |
| Resistance sample 10 [Ω] | 55.8 | 55.7 | 55.7 | 55.6 | 55.6 | 55.6 | 55.2 |

Table G.12: Influence weight and position on resistance measurement through-thickness $[45,\text{-}45,0,90]_{2S}$ samples

| | Mass placed on top [kg] | | | | | | |
|---|---|---|---|---|---|---|---|
| | Position 1 | | | | | | Position 2 |
| | 0 | 1 | 2 | 3 | 4 | 5 | 5 |
| Resistance sample 1 [Ω] | 116.3 | 116.3 | 116.2 | 116.2 | 116.1 | 116.1 | 116.2 |
| Resistance sample 2 [Ω] | 122.1 | 122.1 | 122.1 | 122.1 | 122.1 | 122.1 | 122.1 |
| Resistance sample 3 [Ω] | 93.7 | 93.7 | 93.7 | 93.6 | 93.6 | 93.6 | 93.7 |
| Resistance sample 4 [Ω] | 76.1 | 76.1 | 76.0 | 76.0 | 76.0 | 76.0 | 76.0 |
| Resistance sample 5 [Ω] | 122.1 | 122.1 | 122.1 | 122.0 | 122.0 | 122.0 | 122.0 |
| Resistance sample 6 [Ω] | 120.8 | 120.8 | 120.8 | 120.7 | 120.7 | 120.7 | 120.6 |
| Resistance sample 7 [Ω] | 84.8 | 84.7 | 84.7 | 84.6 | 84.6 | 84.6 | 84.6 |
| Resistance sample 8 [Ω] | 173.7 | 173.7 | 173.7 | 173.7 | 173.6 | 173.6 | 173.5 |
| Resistance sample 9 [Ω] | 119.9 | 119.9 | 119.8 | 119.8 | 119.8 | 119.8 | 119.8 |
| Resistance sample 10 [Ω] | 130.3 | 130.3 | 130.2 | 130.2 | 130.2 | 130.2 | 130.2 |

The dimensions of the different samples used, and the computation of the conductivity in through-thickness direction for all of the lay-ups are given in Tables G.13, G.14, G.15 and G.16.

Table G.13: Results $[0]_{4S}$ samples resistivity and conductivity computation through-thickness direction

| | Dimensions | | | | | |
|---|---|---|---|---|---|---|
| Sample | Width [mm] | Length [mm] | Thickness [mm] | Resistance [Ω] | Resistivity [$\Omega \cdot m$] | Conductivity [$S/m$] |
| 1 | 5.99 | 5.96 | 1.09 | 34.4 | 1.13 | 0.89 |
| 2 | 5.99 | 6.00 | 1.08 | 33.3 | 1.11 | 0.90 |
| 3 | 5.93 | 5.92 | 1.09 | 34.2 | 1.10 | 0.91 |
| 4 | 5.9 | 5.96 | 1.08 | 28.8 | 0.94 | 1.07 |
| 5 | 5.99 | 5.96 | 1.05 | 22.9 | 0.78 | 1.28 |
| 6 | 5.98 | 5.97 | 1.09 | 30.9 | 1.01 | 0.99 |
| 7 | 5.96 | 5.98 | 1.08 | 29.7 | 0.98 | 1.02 |
| 8 | 5.99 | 6.01 | 1.08 | 26.8 | 0.89 | 1.12 |
| 9 | 6.01 | 5.98 | 1.08 | 34.5 | 1.15 | 0.87 |
| 10 | 5.98 | 5.98 | 1.09 | 32.8 | 1.08 | 0.93 |
| | | | **Average** | **30.8** | **1.02** | **1.00** |
| | | | **Standard deviation** | **3.8** | **0.12** | **0.13** |

Table G.14: Results $[0,90]_{2S}$ samples resistivity and conductivity computation through-thickness direction

| | Dimensions | | | | | |
|---|---|---|---|---|---|---|
| Sample | Width [mm] | Length [mm] | Thickness [mm] | Resistance [Ω] | Resistivity $[\Omega \cdot m]$ | Conductivity $[S/m]$ |
| 1 | 5.75 | 5.72 | 1.08 | 36.7 | 1.12 | 0.89 |
| 2 | 5.75 | 5.88 | 1.08 | 47.9 | 1.50 | 0.67 |
| 3 | 5.83 | 5.73 | 1.07 | 39.9 | 1.25 | 0.80 |
| 4 | 5.67 | 5.82 | 1.09 | 44.3 | 1.34 | 0.75 |
| 5 | 5.80 | 5.72 | 1.11 | 64.6 | 1.93 | 0.52 |
| 6 | 5.76 | 5.83 | 1.10 | 49.4 | 1.51 | 0.66 |
| 7 | 5.72 | 5.86 | 1.09 | 37.1 | 1.14 | 0.88 |
| 8 | 5.73 | 5.88 | 1.08 | 47.1 | 1.47 | 0.68 |
| 9 | 5.75 | 5.81 | 1.08 | 43.9 | 1.36 | 0.74 |
| | | | **Average** | **45.7** | **1.40** | **0.73** |
| | | | **Standard deviation** | **8.5** | **0.25** | **0.12** |

Table G.15: Results $[45,-45,0,90]_S$ samples resistivity and conductivity computation through-thickness direction

| | Dimensions | | | | | |
|---|---|---|---|---|---|---|
| Sample | Width [mm] | Length [mm] | Thickness [mm] | Resistance [Ω] | Resistivity $[\Omega \cdot m]$ | Conductivity $[S/m]$ |
| 1 | 6.00 | 5.98 | 1.10 | 80.20 | 2.62 | 0.38 |
| 2 | 5.85 | 5.87 | 1.10 | 53.30 | 1.66 | 0.60 |
| 3 | 5.89 | 5.93 | 1.10 | 47.00 | 1.49 | 0.67 |
| 4 | 5.91 | 5.88 | 1.10 | 51.50 | 1.63 | 0.61 |
| 5 | 5.92 | 5.93 | 1.10 | 56.30 | 1.80 | 0.56 |
| 6 | 5.91 | 5.91 | 1.10 | 49.20 | 1.56 | 0.64 |
| 7 | 5.95 | 5.91 | 1.10 | 47.50 | 1.52 | 0.66 |
| 8 | 5.90 | 5.92 | 1.11 | 34.40 | 1.08 | 0.92 |
| 9 | 5.88 | 5.89 | 1.10 | 51.10 | 1.61 | 0.62 |
| 10 | 5.89 | 5.92 | 1.10 | 55.20 | 1.75 | 0.57 |
| | | | **Average** | **52.6** | **1.67** | **0.62** |
| | | | **Standard deviation** | **11.5** | **0.39** | **0.13** |

Table G.16: Results $[45,-45,0,90]_{2S}$ samples resistivity and conductivity computation through-thickness direction

| | Dimensions | | | | | |
|---|---|---|---|---|---|---|
| Sample | Width [mm] | Length [mm] | Thickness [mm] | Resistance [Ω] | Resistivity [$\Omega \cdot m$] | Conductivity [$S/m$] |
| 1 | 6.01 | 6.01 | 2.25 | 116.1 | 1.86 | 0.54 |
| 2 | 5.98 | 6.03 | 2.25 | 122.0 | 1.96 | 0.51 |
| 3 | 5.97 | 6.01 | 2.24 | 93.6 | 1.50 | 0.67 |
| 4 | 6.03 | 6.02 | 2.25 | 76.0 | 1.23 | 0.82 |
| 5 | 6.04 | 6.06 | 2.20 | 122.0 | 2.03 | 0.49 |
| 6 | 6.00 | 6.06 | 2.25 | 120.6 | 1.95 | 0.51 |
| 7 | 6.04 | 5.99 | 2.24 | 84.6 | 1.37 | 0.73 |
| 8 | 5.98 | 6.06 | 2.14 | 173.5 | 2.94 | 0.34 |
| 9 | 6.00 | 6.01 | 2.27 | 119.8 | 1.90 | 0.53 |
| 10 | 6.01 | 6.03 | 2.26 | 130.2 | 2.09 | 0.48 |
| | | | **Average** | **115.8** | **1.88** | **0.56** |
| | | | **Standard deviation** | **27.3** | **0.48** | **0.14** |

## G.4. CONTACT RESISTIVITY COMPUTATIONS $[45,-45]_{2S}$ SAMPLES IN LONGITUDINAL DIRECTION

Table G.17 gives the dimensions and resistances measured for the samples with an aspect ratio of 1. The amount of mass placed on top of the measurement set-up equals approximately 5 [kg].

Table G.17: Resistance measurements longitudinal $[45,-45]_{2S}$ AR=1 samples

| | Dimensions | | | |
|---|---|---|---|---|
| Sample | Width [mm] | Length [mm] | Thickness [mm] | Resistance measured [Ohm] |
| 1 | 14.84 | 15.96 | 1.12 | 0.54 |
| 2 | 14.80 | 15.86 | 1.12 | 0.66 |
| 3 | 14.85 | 15.88 | 1.09 | 0.43 |
| 4 | 14.84 | 15.83 | 1.09 | 0.43 |
| 5 | 14.80 | 15.87 | 1.11 | 0.41 |
| 6 | 14.85 | 15.88 | 1.13 | 0.39 |
| 7 | 14.95 | 15.85 | 1.13 | 0.51 |
| Ori1 | 16.23 | 14.81 | 1.11 | 0.52 |
| Ori2 | 16.38 | 14.82 | 1.12 | 0.42 |
| Ori3 | 16.27 | 14.85 | 1.12 | 0.43 |
| | | | **Average** | **0.47** |

With the Direct-Current (DC) heating experiments performed on the samples of Table G.17, Table G.18 analyses five of these samples on contact between sample and copper terminals. The parameters $l1$ and $l2$ indicate the lower contact points in between which current flows between copper terminal and sample. The parameters $u1$ and $u2$ indicate these positions for the upper contact points. These parameters are computed relative to the sample geometry and indicate the distance between contact point and left side of the sample in the heating image.

Table G.18: Evaluation heating images $[45,-45]_{2S}$ samples (AR=1) longitudinal resistivity measurements

| | | Photoshop evaluation | | | |
|---|---|---|---|---|---|
| Sample | Width [mm] | l1 [mm] | l2 [mm] | u1 [mm] | u2 [mm] |
| 1 | 14.84 | 3.78 | 11.92 | 4.40 | 14.84 |
| 3 | 14.85 | 2.01 | 12.80 | 0.00 | 14.85 |
| 4 | 14.84 | 0.00 | 12.77 | 2.01 | 14.84 |
| Ori1 | 14.81 | 0.00 | 10.27 | 1.32 | 10.61 |
| Ori2 | 14.82 | 0.00 | 11.66 | 0.00 | 14.82 |

The resistance of the $[45,-45]_{2S}$ samples, with an aspect ratio of 2, measured in longitudinal direction are given in Table G.19.

Table G.19: Resistance measurements longitudinal $[45,-45]_{2S}$ AR=2 samples

| | Dimensions | | | |
|---|---|---|---|---|
| Sample | Width [mm] | Length [mm] | Thickness [mm] | Resistance [Ω] |
| 1 | 14.88 | 31.9 | 1.11 | 0.89 |
| 2 | 14.89 | 31.79 | 1.10 | 0.93 |
| 3 | 14.83 | 31.82 | 1.11 | 1.19 |
| 4 | 14.85 | 31.76 | 1.11 | 1.22 |
| 5 | 14.88 | 31.86 | 1.10 | 1.05 |
| 6 | 14.85 | 31.60 | 1.06 | 1.07 |
| 7 | 14.85 | 31.87 | 1.11 | 0.96 |
| 8 | 14.87 | 31.82 | 1.09 | 0.88 |
| 9 | 14.82 | 31.89 | 1.11 | 0.96 |
| 10 | 14.81 | 31.82 | 1.12 | 0.88 |
| | | | **Average** | **1.00** |

Table G.20 gives the resistance measurement results in longitudinal direction for the $[45,-45]_{2S}$ samples with an aspect ratio of 3.

Table G.20: Resistance measurements longitudinal $[45,-45]_{2S}$ AR=3 samples

| | Dimensions | | | |
|---|---|---|---|---|
| Sample | Width [mm] | Length [mm] | Thickness [mm] | Resistance [Ω] |
| 1 | 14.9 | 47.81 | 1.10 | 1.58 |
| 2 | 14.79 | 47.74 | 1.09 | 1.60 |
| 3 | 14.86 | 47.76 | 1.10 | 1.70 |
| 4 | 14.9 | 47.78 | 1.10 | 1.54 |
| 5 | 14.83 | 47.83 | 1.10 | 1.70 |
| 6 | 14.8 | 47.69 | 1.11 | 1.54 |
| 7 | 14.95 | 47.77 | 1.10 | 1.53 |
| 8 | 14.82 | 47.57 | 1.12 | 1.47 |
| | | | Average | 1.58 |

## G.5. AC-RESISTANCE THROUGH-THE-THICKNESS MEASUREMENTS $[0,90]_{2S}$ SAMPLES

For the Alternating-Current (AC) measurements performed on the $[0,90]_{2S}$, five different samples were cut and gold sputtered. The dimensions of these samples are included in Table G.21.

Table G.21: AC Resistance measurement samples through-the-thickness $[0,90]_{2S}$ laminate

| | Dimensions | | |
|---|---|---|---|
| Sample | Width [mm] | Length [mm] | Thickness [mm] |
| 1 | 10.92 | 10.92 | 1.11 |
| 2 | 10.86 | 10.80 | 1.10 |
| 3 | 10.84 | 10.87 | 1.10 |
| 4 | 10.95 | 10.87 | 1.11 |
| 5 | 10.89 | 10.90 | 1.10 |

# H

# COMSOL MODEL RESISTANCE EXPERIMENTS

The Comsol model, used to model the resistance experiments, is explained in the current Appendix. The geometry definition, meshing strategy, material definition, model set-up and solver type used, will be explained.

## H.1. GEOMETRY

The geometry of the resistance samples is based on the dimensions measured, included in Appendix G. Figure H.1 shows the geometry used in the resistance model.

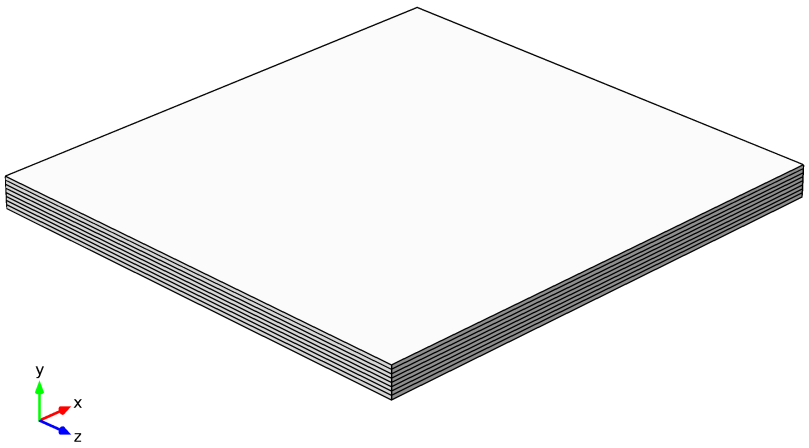


Figure H.1: Geometry used for $[0]_{4S}$, $[90]_{4S}$ and $[45,\text{-}45]_{2S}$ samples

Each ply is modelled separately in order to be able to apply the heterogeneous material properties. Bézier polygon partition lines are used in order to split the surfaces that are in contact with the copper terminals of the resistance measurement set-up. The partition is added in order to be able to model the improper contact between sample and copper terminal, witnessed with the Direct-Current (DC) heating experiments. The surfaces mentioned are shown in Figures H.2 and H.3.

## H.2. MATERIAL DEFINITION

The material properties given in Chapters 2 and 4 are used as material properties. The individual ply properties are included by rotating the global material properties over the individual angles at which the plies are oriented. This is done by locally rotating the coordinate system.

## H.3. CONSTRAINTS

The model consists of an Electric Currents physics module. Within this model the following constraints are applied:

- Current conservation, applied to the entire geometry domain.
- Electric insulation, applied to all the surfaces at which no other boundary conditions are applied.

- Initial value of 0 [V], applied on the entire geometry domain.
- Ground boundary condition (U=0[V]), applied to the surface in contact with the ground copper terminal.
- Terminal boundary conditions (I=1[A]), applied to the sample surface in contact with the other copper terminal.
- Contact impedance, applied to the interfaces between the individual plies. This boundary condition models the contact resistivity between plies and equals the values found in Chapter 4.

Figures H.2 and H.3 show the surfaces at which the ground and terminal boundary conditions are applied, indicated by their blue colours.

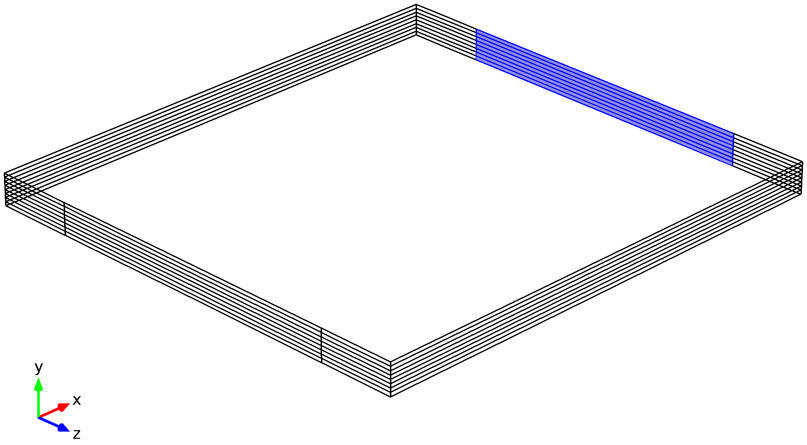


Figure H.2: Surfaces on which the ground boundary condition is applied

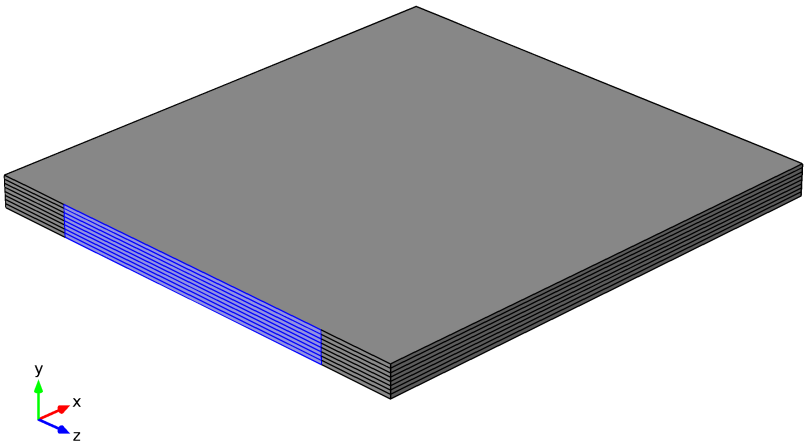


Figure H.3: Surfaces on which the terminal boundary condition is applied

## H.4. MESHING

The entire geometry is meshed with the help of structured triangular elements, swept through the thickness of the geometry. Structured triangular elements were used in order to have the elements aligned with all of the fibre orientations present within the laminate lay-up. The surface mesh is shown in Figure H.4.

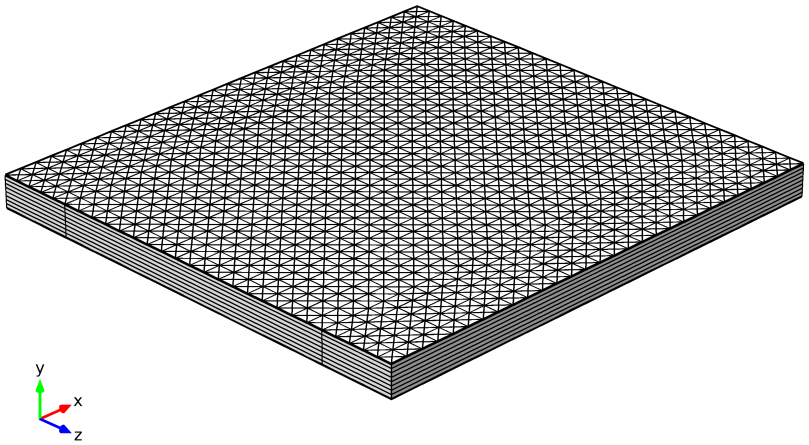


Figure H.4: Surface mesh used for the modelling of the resistance samples

This mesh is swept through the thickness. Each ply contains multiple elements in thickness direction, in order to be able to properly model the current distribution in thickness direction. Figure H.5 shows the mesh distribution through-the-thickness.

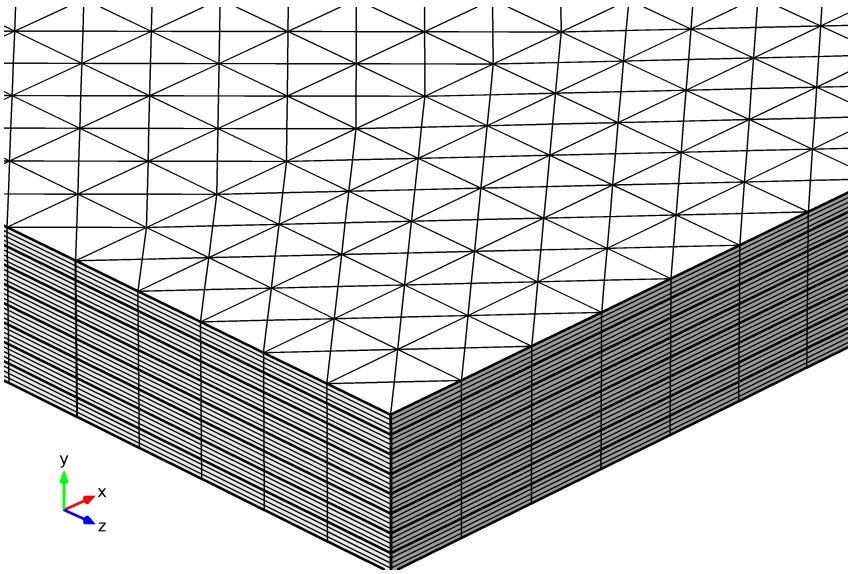


Figure H.5: Swept mesh through the thickness

## H.5. SOLVER TYPE

A stationary study step is used in order to find the steady-state resistance in the longitudinal direction of the samples.

## H.6. POST-PROCESSING

The Comsol model is used to find the resistance in the same direction as was measured experimentally. This can be achieved by doing a global evaluation of the resistance in 11-direction within Comsol. This correspond to the x-axis of the model.

# I

# THERMOCOUPLE LOCATIONS

This appendix shows all of the locations of all of the thermocouples used to measure the temperatures during heating experiments. The thermocouple locations for the heating tests performed with the horizontal Helmholtz coil are shown in Figure I.1. Figure I.2 shows the locations for the heating experiments performed with the Hairpin coil. Note that these coordinates are with respect to the global coordinate system, with the origin in the center of the coil's geometry.

Table I.1: Thermocouple locations heating experiments horizontal Helmholtz coil

| | | | Location | | |
|---|---|---|---|---|---|
| Laminate | Orientation a $\alpha$ [deg] | Thermocouple [-] | x [mm] | y [mm] | z [mm] |
| $[0]_{4S}$ | 0 | TC1 | 0 | -11.1 | 0 |
| | | TC2 | 16 | -11.1 | 0 |
| | | TC3 | 32 | -11.1 | 0 |
| | | TC4 | 0 | -10 | 0 |
| | 45 | TC1 | 0 | -11.1 | 0 |
| | | TC2 | 16 | -11.1 | 0 |
| | | TC3 | 32 | -11.1 | 0 |
| | | TC4 | 0 | -10 | 0 |
| | 90 | TC1 | 0 | -11.1 | 0 |
| | | TC2 | 14 | -11.1 | 0 |
| | | TC3 | 30 | -11.1 | 0 |
| | | TC4 | 0 | -10 | 0 |
| $[0,90]_{2S}$ | 0 | TC1 | 0 | -11.1 | 0 |
| | | TC2 | 16 | -11.1 | 0 |
| | | TC3 | 13 | -11.1 | -15 |
| | | TC4 | 0 | -10 | 0 |
| | 45 | TC1 | 0 | -11.1 | 0 |
| | | TC2 | 22 | -11.1 | 23 |
| | | TC3 | 21 | -11.1 | 0 |
| | | TC4 | 0 | -10 | 0 |
| $[45,-45,0,90]_S$ | 0 | TC1 | 0 | -11.1 | 0 |
| | | TC2 | 19 | -11.1 | -11 |
| | | TC3 | 0 | -11.1 | -21 |
| | | TC4 | 0 | -10 | 0 |
| | 45 | TC1 | 0 | -11.1 | 0 |
| | | TC2 | 20 | -11.1 | 0 |
| | | TC3 | 16 | -11.1 | -17 |
| | | TC4 | 0 | -10 | 0 |
| | 90 | TC1 | 0 | -11.1 | 0 |
| | | TC2 | 12 | -11.1 | 18 |
| | | TC3 | 21 | -11.1 | 0 |
| | | TC4 | 0 | -10 | 0 |

Table I.2: Thermocouple locations heating experiments Hairpin coil

| | | | Location | | |
|---|---|---|---|---|---|
| Laminate | Orientation a $\alpha$ [deg] | Thermocouple [-] | x [mm] | y [mm] | z [mm] |
| $[0]_{4S}$ | 0 | TC1 | 0 | -11.1 | 0 |
| | | TC2 | 30 | -11.1 | 0 |
| | | TC3 | 60 | -11.1 | 0 |
| | | TC4 | 0 | -10 | 0 |
| | 45 | TC1 | 0 | -11.1 | 0 |
| | | TC2 | 7.1 | -11.1 | -7.1 |
| | | TC3 | 14.1 | -11.1 | -14.1 |
| | | TC4 | 0 | -10 | 0 |
| | 90 | TC1 | 0 | -11.1 | 0 |
| | | TC2 | 10 | -11.1 | 0 |
| | | TC3 | 20 | -11.1 | 0 |
| | | TC4 | 0 | -10 | 0 |
| $[0,90]_{2S}$ | 0 | TC1 | 0 | -11.1 | 0 |
| | | TC2 | 35 | -11.1 | 0 |
| | | TC3 | 0 | -11.1 | -13 |
| | | TC4 | 0 | -10 | 0 |
| | 45 | TC1 | 0 | -11.1 | 0 |
| | | TC2 | 30 | -11.1 | 30 |
| | | TC3 | 23 | -11.1 | -13 |
| | | TC4 | 0 | -10 | 0 |
| $[45,-45,0,90]_S$ | 0 | TC1 | 0 | -11.1 | 0 |
| | | TC2 | 36 | -11.1 | 0 |
| | | TC3 | 0 | -11.1 | -15 |
| | | TC4 | 0 | -10 | 0 |
| | 45 | TC1 | 0 | -11.1 | 0 |
| | | TC2 | 25 | -11.1 | 25 |
| | | TC3 | 8 | -11.1 | -10 |
| | | TC4 | 0 | -10 | 0 |
| | 90 | TC1 | 0 | -11.1 | 0 |
| | | TC2 | 0 | -11.1 | 32 |
| | | TC3 | 12 | -11.1 | 0 |
| | | TC4 | 0 | -10 | 0 |

# J

# VALIDATION RESULTS

This appendix gives the raw data used to validate the Comsol induction heating model. The starting temperature, amperage, resonance frequency and duration settings are given in Table J.1 for all of the different laminates, coils and orientations.

Table J.1: Initial conditions induction heating experiments

| | | | Settings | | | |
|---|---|---|---|---|---|---|
| Coil | Laminate | Orientation [deg] | $T_{start}$ [$^oC$] | Amperage [A] | Frequency [kHz] | Duration [s] |
| Helmholtz | $[0]_{4S}$ | 0 | 22.4 | 399 | 346 | 15 |
| | | 45 | 21.0 | 399 | 347 | 15 |
| | | 90 | 22.5 | 399 | 347 | 15 |
| | $[0,90]_{2S}$ | 0 | 22.4 | 69.3 | 359 | 15 |
| | | 45 | 22.4 | 69.3 | 359 | 15 |
| | $[45,-45,0,90]_S$ | 0 | 23.5 | 69.3 | 369 | 15 |
| | | 45 | 23.0 | 69.3 | 369 | 15 |
| | | 90 | 23.3 | 69.3 | 369 | 15 |
| Hairpin | $[0]_{4S}$ | 0 | 21.2 | 399 | 361 | 15 |
| | | 45 | 22.1 | 399 | 359 | 15 |
| | | 90 | 21.9 | 399 | 360 | 15 |
| | $[0,90]_{2S}$ | 0 | 21.5 | 149.1 | 365 | 15 |
| | | 45 | 21.6 | 149.1 | 367 | 15 |
| | $[45,-45,0,90]_S$ | 0 | 23.2 | 149.1 | 367 | 15 |
| | | 45 | 23.2 | 149.1 | 366 | 15 |
| | | 90 | 22.9 | 149.1 | 366 | 15 |

All laminates have been heated for 15 [s]. The temperatures after 15 [s] of heating have been compared. The exact thermocouple locations are given in Appendix I. Thermocouples TC1 and TC4 are always located at the centre of the laminate on the bottom and top surface, relative to the coil. Thermocouple TC3 is always located at the position of maximum heating, depending on the laminate lay-up. The differences between experiments and comsol temperature predictions are given in Table J.2. The differences are indicated with their percentage difference relative to each other. A negative value indicates an underestimation of the temperature predicted by Comsol.

Table J.2: Percentage differences Comsol and experimental results thermocouple temperatures

| | | | Thermocouple difference [%] | | | |
|---|---|---|---|---|---|---|
| Coil | Laminate | Orientation [deg] | TC1 | TC2 | TC3 | TC4 |
| Helmholtz | $[0]_{4S}$ | 0 | -24.6 | -27.7 | -19.4 | -22.9 |
| | | 45 | -14.7 | -7.8 | -8.1 | -19.1 |
| | | 90 | -16.9 | -18.7 | -10.1 | -17.7 |
| | $[0,90]_{2S}$ | 0 | -31.8 | 0.4 | -17.2 | -28.9 |
| | | 45 | -24.2 | -24.4 | -13.0 | -23.2 |
| | $[45,-45,0,90]_S$ | 0 | -21.4 | 3.7 | 10.9 | -27.4 |
| | | 45 | -20.5 | 2.5 | 10.8 | -17.3 |
| | | 90 | -17.2 | 3.3 | -1.3 | -11.8 |
| Hairpin | $[0]_{4S}$ | 0 | -4.8 | 11.9 | 12.4 | -3.0 |
| | | 45 | 2.1 | 8.2 | 6.6 | 4.9 |
| | | 90 | -3.3 | -1.7 | -1.9 | -3.1 |
| | $[0,90]_{2S}$ | 0 | -32 | -7.3 | 21.9 | -32.6 |
| | | 45 | 18.8 | 0.8 | -0.5 | 23 |
| | $[45,-45,0,90]_S$ | 0 | -8.0 | 7.5 | 18.2 | -8.7 |
| | | 45 | -1.6 | 15.9 | 21.4 | -1.6 |
| | | 90 | 3.3 | 11.6 | 0.9 | 8.6 |

Table J.3 gives the actual temperatures for both the experimental (Exp) and Comsol model predictions (Com).

Table J.3: Temperatures thermocouples experiments and Comsol model

| | | | Temperature comparison | | | | | | | |
|---|---|---|---|---|---|---|---|---|---|---|
| | | | TC1 | | TC2 | | TC3 | | TC4 | |
| Coil | Laminate | Orientation [deg] | Exp [$^oC$] | Com [$^oC$] | Exp [$^oC$] | Com [$^oC$] | Exp [$^oC$] | Com [$^oC$] | Exp [$^oC$] | Com [$^oC$] |
| Helmholtz | $[0]_{4S}$ | 0 | 31.6 | 23.8 | 47.6 | 34.4 | 49.6 | 39.9 | 30.9 | 23.8 |
| | | 45 | 25.7 | 21.9 | 32.8 | 30.2 | 37.7 | 34.7 | 27.1 | 21.9 |
| | | 90 | 28.2 | 23.4 | 37.2 | 30.3 | 39.5 | 35.5 | 28.4 | 23.4 |
| | $[0,90]_{2S}$ | 0 | 42.3 | 29.0 | 58.1 | 59.2 | 95.9 | 79.0 | 40.6 | 29.0 |
| | | 45 | 39.6 | 30.0 | 85.9 | 63.0 | 75.7 | 67.0 | 38.9 | 29.9 |
| | $[45,-45,0,90]_S$ | 0 | 37.2 | 29.4 | 71.2 | 74.7 | 72.7 | 82.2 | 40.3 | 29.4 |
| | | 45 | 36.5 | 29.3 | 70.8 | 73.5 | 69.9 | 78.6 | 35.1 | 29.6 |
| | | 90 | 36.8 | 30.7 | 71.8 | 75.0 | 75.5 | 76.0 | 34.6 | 30.7 |
| Hairpin | $[0]_{4S}$ | 0 | 23.3 | 22.2 | 32.0 | 35.8 | 32.5 | 36.5 | 22.9 | 22.2 |
| | | 45 | 23.1 | 22.7 | 23.6 | 24.1 | 23.7 | 23.9 | 23.0 | 22.7 |
| | | 90 | 22.8 | 22.0 | 23.0 | 22.6 | 23.2 | 22.7 | 22.7 | 22.0 |
| | $[0,90]_{2S}$ | 0 | 38.9 | 26.4 | 57.8 | 54.3 | 62.0 | 75.8 | 39.2 | 26.4 |
| | | 45 | 42.5 | 47.5 | 51.7 | 50.7 | 60 | 59.4 | 40.9 | 47.1 |
| | $[45,-45,0,90]_S$ | 0 | 42.2 | 36.8 | 54.7 | 59.2 | 58.3 | 70.9 | 42.6 | 36.9 |
| | | 45 | 41.7 | 39.9 | 53.0 | 61.2 | 54.3 | 67.7 | 41.7 | 39.4 |
| | | 90 | 44.6 | 44.9 | 56.6 | 63.3 | 60.0 | 61.9 | 42.6 | 45 |

# K

# ANSYS MODEL

The first approach on modelling the induction heating phenomenon was based on using the Ansys software, due to its availability at KVE. However, after multiple setbacks and several different modelling approaches, the decision was made to switch to Comsol Multiphysics. The different modelling approaches and the erroneous results it produced will be discussed.

Different modelling methods have been applied in order to accurately predict the heating behaviour and occurring temperatures of the Uni-Directional (UD) Carbon Fibre (CF)-Poly(Ether-Ketone-Ketone) (PEKK) material. One of the first methods of modelling the induction heating phenomenon was based on modelling each ply separately and assigning all of the obtained material parameters to each individual ply. The coil, surroundings and boundary conditions could only have been modelled one specific way (based on the Ansys manual [95]).

## K.1. LAMINATE LAY-UP $[0]_{4S}$

The Helmholtz and Hairpin coil have both been modelled with the $[0]_{4S}$ laminate under the three different orientations $\alpha = 0, 45, 90[deg]$. Figure K.1 shows the heating pattern obtained by Ansys together with the actual heating pattern for the Helmholtz coil and the laminate under an orientation of $\alpha = 0[deg]$.

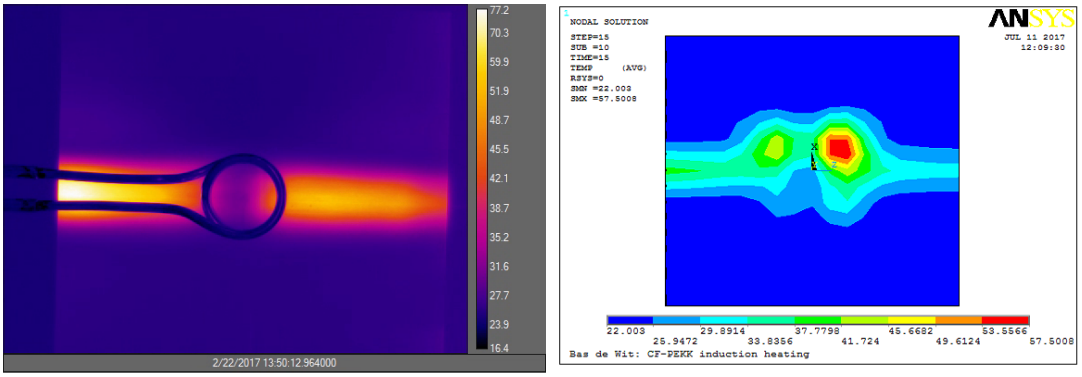


(a) After 15[s] heating experiment

(b) After 15[s] heating Ansys

Figure K.1: Heating pattern prediction $[0]_{4S}$, Helmholtz coil, $\alpha = 0[deg]$, 400 [A]

The coil is excluded in Figure K.1b, because it was not included in the thermal analysis in Ansys. Figure K.1b shows that Ansys actually predicts a heating pattern that stretches out over the entire width of the laminate. There are however key differences between the model and experimental results. Figure K.1b clearly shows how Ansys predicts a heating pattern which is more spread out around the coil, compared to the narrow heating pattern from Figure K.1a. In order to find out what is causing this difference, one should look into how the heat generation is computed by Ansys. The Joule heat generation per element is computed with the help of Equation K.1 [96].

$$Q^j = \mathrm{Re}\left(\frac{1}{2n}\sum_{i=1}^{n}[\rho]\{J_{ti}\}\cdot\{J_{ti}\}^*\right) \tag{K.1}$$

Where $n$, $\rho$, $J_{ti}$, the number of integration points, the resistivity matrix and the complex total current density in the element at integration point $i$ respectively [96]. Equation K.1 shows that the generation of heat is based on the eddy current density tensor and the resistivity properties of the material. By analysing the eddy current

density through the laminate, one should be able to find the cause of the difference between experimental and computational results. Figure K.2 shows the eddy current densities parallel, perpendicular and through-the-thickness directions with respect to the fibre orientation. Note that the values are unreadable, but will be assessed in the following text.

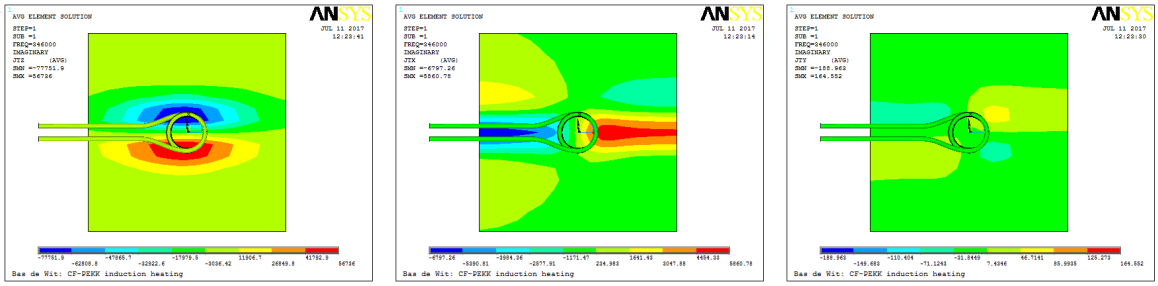

(a) Eddy current density parallel to fibre

(b) Eddy current density transverse to fibre

(c) Eddy current density through-the-thickness

Figure K.2: Ansys eddy current distribution $[0]_{4S}$, Helmholtz coil, $\alpha = 0[deg]$, 400 [A]

The figures represent contour plots, showing the locations of maximum and minimum eddy current densities. The maximum eddy current density parallel to the fibre is actually almost a factor 12 larger than the maximum eddy current density perpendicular to the fibre. The eddy current density in thickness direction is close to zero, indicating no currents are going through the thickness of the material for this specific heating example. However, because the heat generation function is depending on the material's resistivity and due to the fact that the resistivity in transverse direction is almost a factor 1400 bigger, causes the in-plane transverse current density to be dominant in the heating of the $[0]_{4S}$ laminate.

In order to further investigate how the currents are going through the material and its influence on the heating pattern, the resistivity of the material was set to infinity in particular directions. A total of three additional tests were performed with the transverse resistivity, the through-the-thickness resistivity and both the transverse and through-the-thickness resistivities set to infinity. By setting the material's resistivity in a particular direction to infinity, one prohibits any currents from flowing into this direction through the material. The heat generation pattern can then be analysed to see the effect of the current path.

Figure K.2c showed that the through-the-thickness current density was close to zero. Equation K.1 shows that the through-the-thickness current density will thus not have caused the spread in the heat generation pattern of Figure K.1b. In order to prove this, the through-the-thickness resistivity of the laminate was set to infinity, prohibiting any currents from flowing into this particular direction. Rerunning the model with the adjusted material properties showed no differences to occur for the heating pattern predicted by Ansys. This confirms the assumption that the spread in the heating pattern of Figure K.1b is not caused by any out-of-plane current densities.
The next step was to look into setting the in-plane transverse resistivity to infinity, limiting any eddy currents to go into that direction inside the laminate. It was assumed that by doing this, the currents would have to find an alternative route, completely changing the original heating pattern observed in Figure K.1b. The heat generation pattern prediction, based on these adjusted material properties, is given in Figure K.3.

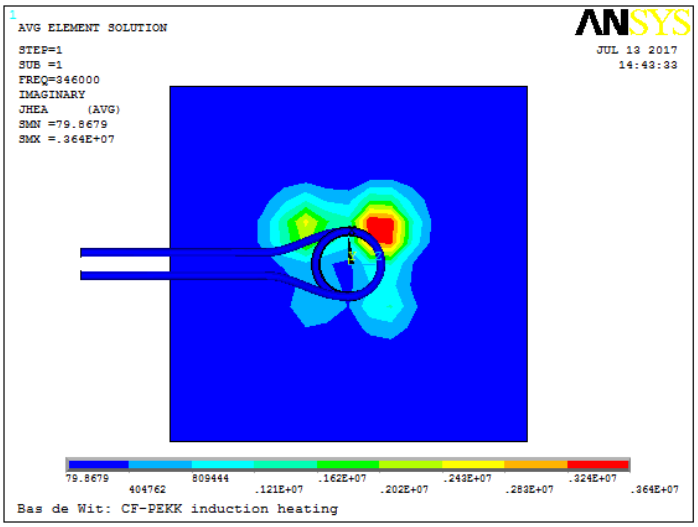


Figure K.3: Heat generation by Helmholtz, $[0]_{4S}$ laminate, 400 [A] with infinite transverse resistivity

The figure shows how the generation of heat is different from the original result due to the infinite resistivity perpendicular to the fibre direction. When looking into the current densities however, one notices no difference in current density patterns except for the transverse current density going to zero. This was expected to occur since the material is now non-conducting in transverse direction. The current density parallel to the fibre shows a reduction of almost 40% in amplitude. This is also as expected. The current is unable to flow in transverse direction and now has to follow a different path to complete the circuit inside of the laminate. The chances are that this path has a higher equivalent resistance than the original current path, reducing the current density in this direction. However, when looking at the through-the-thickness current density, one notices no changes at all. The current density has not increased and is still negligible. The question now arises, where does the heat generation of Figure K.3 come from? It is not based on the through-the-thickness nor the transverse current density. The current density contour of Figure K.2a also does not agree with Figure K.3. In order to see whether the generation of heat is actually being computed correctly, both the electric resistivities in thickness direction as in transverse direction are set to infinity.

When setting both the electric resistivities in thickness direction as in transverse direction to infinity, all current densities should reduce to zero. The current will no longer be able to close the circuit in the laminate. With the generation of heat based on the current densities, the heat generation pattern should also go to zero. After running the model with these material properties, the results showed that the eddy current densities in all directions returned to zero. This shows that the model actually does take into account that currents cannot be generated when there is no path for them to close the circuit. Figure K.4 shows the effects of setting the transverse and through-the-thickness resistivity to infinity for the $[0]_{4S}$ laminate heated by the Helmholtz coil. Figure K.4a shows how the net current density is approximately equal to zero (maximum value of $0.3E^{-05}[A/m^2]$. Even though the current densities go to zero, the heat that is being generated within the laminate is not going to zero. The heat generation for the top layer when there are no eddy currents going through the material is given in Figure K.4b.

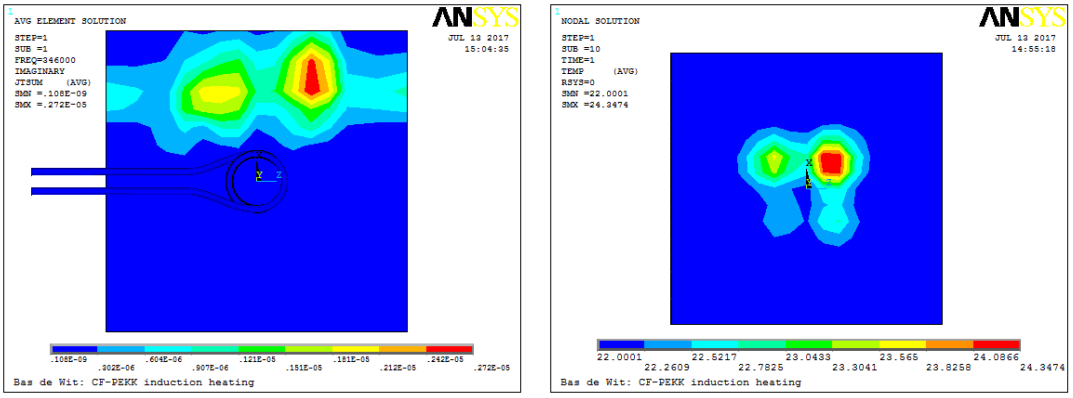


(a) Net current density top layer $[0]_{4S}$ laminate (b) Heat generation pattern top layer $[0]_{4S}$ laminate

Figure K.4: Influence transverse and through-thickness resistivity set to infinity, $[0]_{4S}$ laminate, Helmholtz coil

Figure K.4 shows how even though the summation of the eddy current density is zero, it is still giving a non-zero heat generation. Apparently, heat is being generated by something else than the eddy current density. The location where most of the heat is generated corresponds to the location where there was a spread in the heating pattern in Figure K.1b. The relative magnetic permeability of the material has been set to 1, also not being the reason for this unknown source in the heat generation. This unknown heat source is causing the difference between model predictions and experimental results. Why heat is being generated even though the current densities are equal to zero remains unknown.

In order to see whether this unknown source of heating is also present with different coil geometries, the Hairpin coil was also investigated. Figure K.5 shows the different heat generation patterns for the different orientations investigated.

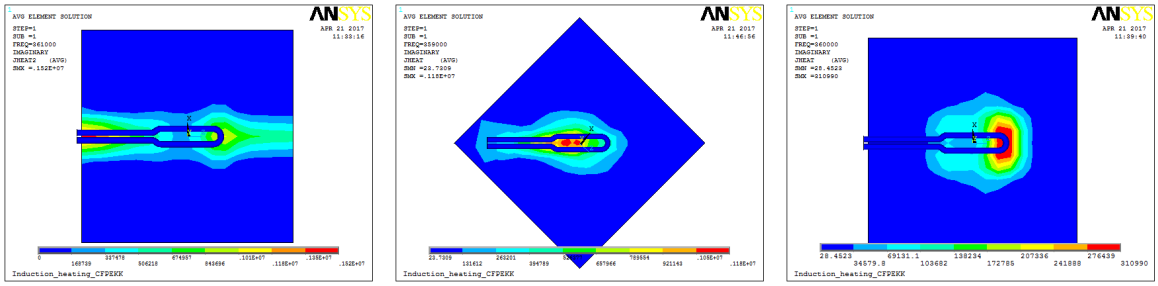

(a) $\alpha = 0[deg]$ (b) $\alpha = 45[deg]$ (c) $\alpha = 90[deg]$

Figure K.5: Heat generation pattern $[0]_{4S}$ laminate, Hairpin coil, 150 [A]

Figure K.5a shows a similarity with Figure K.1b, with the spread in the generation of heat located around the tip of the coil. Ansys is also unable to predict the generation of heat for the orientation of $\alpha = 45[deg]$ and the orientation of $\alpha = 90[deg]$ has the same spread in heat around the tip. Ansys is also unable to accurately predict the heating pattern that occurs for the Hairpin coil for the $[0]_{4S}$ laminate.

There seems to be an additional source of heat present, not based on the eddy currents going through the laminate. This causes deviations in heating patterns. Due to this unknown heat source, the thermocouple temperatures will not be compared because the data coming from the Ansys model will be based on erroneous results.

## K.2. LAMINATE LAY-UP $[0,90]_{2S}$

It is important that the Ansys model is able to predict the thermal behaviour in through-thickness direction. It is expected that the through-the-thickness heating behaviour dictates the overall heating of the cross-ply and

quasi-isotropic laminates. When the model is not able to predict the thermal pattern nor the temperatures occurring in the $[0,90]_{2S}$ laminate, it will not be able to predict any of the lay-ups correctly. Research has already shown a difference in heating patterns occurring for the $[0]_{4S}$ laminate. However, because these lay-ups are rarely used in practical applications, one will also investigate the ability of Ansys to predict other lay-ups. If the same problems are not encountered for angled-ply lay-ups, the model can still be useful. Figure K.6 shows the heat prediction of Ansys and the actual heating pattern occurring for the $[0,90]_{2S}$ laminate, heated with the Helmholtz coil and the laminate under $\alpha = 0[deg]$.

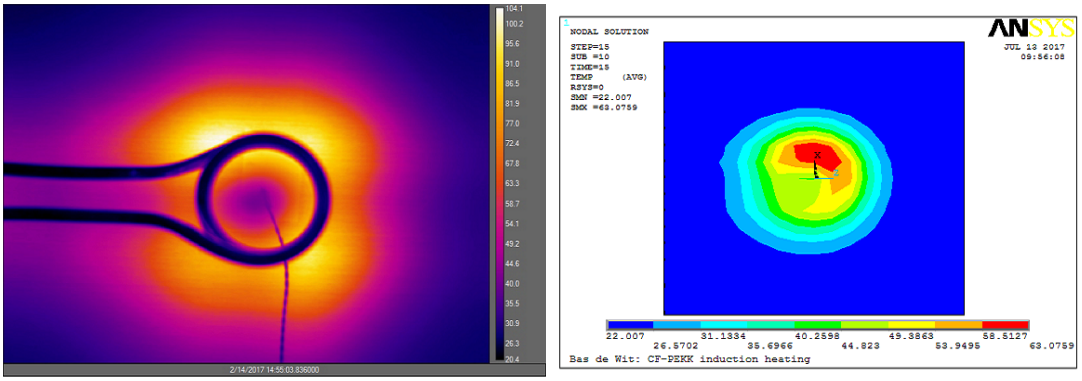


(a) After 15[s] heating experiment

(b) After 15[s] heating Ansys

Figure K.6: Heating pattern prediction $[0,90]_{2S}$, Helmholtz coil, $\alpha = 0[deg]$, 70 [A]

Although the heating patterns look somewhat similar, one major difference is the fact that the Ansys model is lacking the four distinct heating spots witnessed with the experimental results. By looking at the eddy current densities predicted by Ansys, one can find out what is causing this distinct heating pattern. Figure K.7 show the eddy current densities in three principle directions for this specific heating experiment.

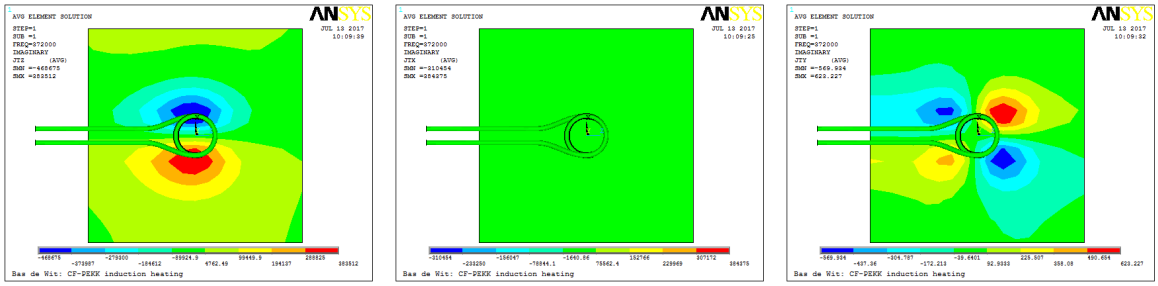


(a) Eddy current density parallel to fibre

(b) Eddy current density transverse to fibre

(c) Eddy current density through-the-thickness

Figure K.7: Ansys eddy current distribution $[0,90]_{2S}$ top ply, Helmholtz coil, $\alpha = 0[deg]$, 70 [A]

Figure K.7 only shows the eddy current distribution for the top ply. Because the eddy current density changes with the direction of the fibre, each ply will have a different distribution, rotated accordingly. The figures show how the eddy current density parallel to the fibre orientation is almost 500 times larger than in through-the-thickness direction. With the generation of heat being dependent on the eddy current density squared (Equation K.1), most of the heat will be generated in the direction of the fibre, even though the resistance is much smaller compared to the through-the-thickness resistance. Figure K.7c shows the locations where the current jumps through the thickness. The pattern is very similar to the locations of maximum heat generation in the experimental results.

In order to further understand the thermal behaviour of the laminate and to see whether there is again an unknown heat source present, particular material properties have been set to infinity in order to limit the current paths. The transverse resistivity, the through-the-thickness resistivity and both the transverse and through-the-thickness resistivities were set to infinity to see the effect on the heat generation pattern.

Because the current is expected to jump through the thickness to the adjacent ply, it is expected that by changing the transverse resistivity to infinity, no differences in the prediction of the heat generation pattern are expected. Running the model with these material properties confirmed this assumption. The eddy current densities do not change due to setting the in-plane transverse resistivity to infinity. The current is following the path alongside the fibre and jumps through the thickness to the adjacent ply at four distinct spots.

By setting the through-the-thickness resistivity of the ply to infinity, it is expected that each ply now thermally behaves as the results found in Section K.1. The current is now unable to jump through the thickness and will have to go in transverse direction to close the equivalent circuit that exists in each ply. The results however show that this is not the case in the evaluation of the problem by Ansys. The current density in through-the-thickness direction is reduced to zero and the maximum current density in fibre direction is reduced by approximately 40%. The heat generation patterns of the original material properties and the heat generation pattern for with infinite through-the-thickness resistivity are given in Figure K.8.

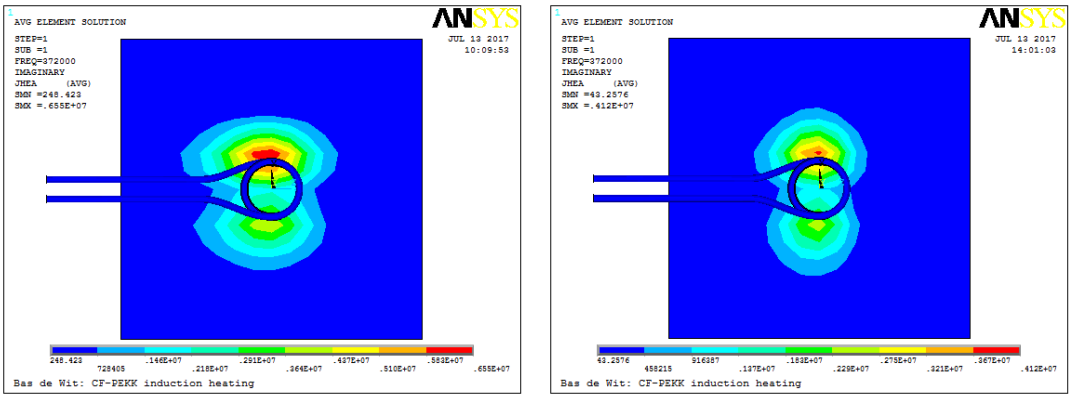


(a) Original heat generation

(b) Infinite through-the-thickness resistivity

Figure K.8: Heat generation patterns top layer $[0,90]_{2S}$ laminate, Helmholtz coil, $\alpha = 0[deg]$, 70 [A]

Figures K.8a and K.8b show limited differences when comparing the heat generation patterns. Apparently, the current density in fibre direction is still causing heat to be generated at the same location even though no currents can go through the thickness of the material. Looking at the in-plane transverse current density of the adjusted material model, one notices that this has not increased and is still equal to zero. Even though the transverse and through-the-thickness current densities are equal to zero, the longitudinal current density only decreased by a maximum of 40%. It is still causing the generation of heat through the laminate. Setting both the transverse and through-the-thickness resistivities to infinity does not change anything compared to Figure K.8b. It seems that the currents are able to jump from surface to surface because the ply solids are in electrical contact. Setting the through-the-thickness resistivity to infinity does not prohibit the currents to still go from ply to ply due to this. In order to find out if indeed electric contact is causing the generation of heat, a separate solid with infinite resistivity properties is modelled in between two fibre plies. The heat generation pattern of each of the plies now indeed resembles the heat generation pattern of Figure K.1b. In order to prevent currents from jumping from surface to surface, either a surface resistivity or a solid material should be included in between the fibre plies. However, Ansys only offers to include a surface resistivity in electric analyses and not in electromagnetic analyses. The only method of avoiding electric contact between individual plies is to physically model a separate layer in between. The thickness of such a solid and the electric and thermal properties such a solid should obtain are completely unknown. It cannot be related to any physical properties seen with the microscopy images. It was decided not to model such a matrix layer in between the fibre plies but to switch multi-physics software. Comsol Multiphysics was chosen due to its availability and the possibility of including surface resistivity properties in between fibre plies.

## K.3. Conclusion

The simulations of the $[0]_{4S}$ and $[0,90]_{2S}$ laminates showed that Ansys is not able to correctly predict the heating patterns witnessed in experiments. The analyses into the resistivity of the material showed an unknown heat source to occur in the $[0]_{4S}$ laminate, causing the differences in heating patterns between the computational and experimental results. Next to that, electric contact between fibre plies prohibits one to accurately

model the heating behaviour of angled-ply laminates. The inability of Ansys to include a surface resistivity within the electromagnetic solver module lead to the decision to switch multi-physics software to model the induction heating of UD CF-PEKK laminates. A solution to still be able to model the problem with Ansys is by inserting a solid layer in between fibre ply solids. This solid will prohibit currents from jumping from surface to surface. However, due to the vast number of unknowns related to modelling a separate solid layer in between fibre layers, it was decided to continue modelling with Comsol Multiphysics.